NASA CONTRACTOR REPORT

NASA CR-1625

SCALING OF VTOL RECIRCULATION EFFECTS

by Gordon R. Hall

Prepared by
NORTHROP CORPORATION
Hawthorne, Calif.
for Lewis Research Center

NATIONAL AERONAUTICS AND SPACE ADMINISTRATION • WASHINGTON, D. C. • AUGUST 1970

1. Report No. NASA CR-1625	2. Government Accession No.	3. Recipient's Catalog No.
4. Title and Subtitle SCALING OF VTOL RECIRCULATION EFFECTS		5. Report Date August 1970 6. Performing Organization Code
7. Author(s) Gordon R. Hall		8. Performing Organization Report No. None
9. Performing Organization Name and Address Northrop Corp~~oration~~ Hawthorne, California		10. Work Unit No. 11. Contract or Grant No. NAS 3-10498
12. Sponsoring Agency Name and Address National Aeronautics and Space Administration Washington, D.C. 20546		13. Type of Report and Period Covered Contractor Report 14. Sponsoring Agency Code

15. Supplementary Notes

16. Abstract

Reported herein are full-scale/small-scale comparisons of VTOL recirculation effects. The full-scale "reference" data were obtained from an investigation of a lift engine pod with two G. E. YJ-85 engines spaced approximately seven nozzle diameters apart. The small-scale data were obtained using a 1/5 scale geometrically similar model with simulated engine inlet and exhaust flows. Test conditions, instrumentation, and data reduction and analysis techniques were similar for the full-scale and small-scale investigations. The results indicate that the overall flow field and thermal environment including the free jets, ground jets, upwash, and hot gas ingestion are scalable, in terms of both dynamic and time-average characteristics, for the same exhaust pressure/temperature in full scale and small scale.

17. Key Words (*Suggested by Author(s)*)

1, VTOL
2, Jet ~~exhaust~~ Engines
Hot gas reingestion
3, Exhaust Gases

18. Distribution Statement

Unclassified - unlimited

19. Security Classif. (of this report)	20. Security Classif. (of this page)	21. No. of Pages	22. Price*
Unclassified	Unclassified	128	$3.00

*For sale by the Clearinghouse for Federal Scientific and Technical Information
Springfield, Virginia 22151

FOREWORD

This report documents the results of a detailed comparison of the recirculation and ingestion characteristics of a full-scale and geometrically similar small-scale engine pod. The work was performed by the Northrop Corporation under NASA contract NAS 3-10498. This contract provided for a series of exploratory experimental investigations, the primary objective being to determine the relative effectiveness and merits of various exhaust gas ingestion control concepts for potential application to VTOL aircraft. Secondary objectives of the contract were (1) to establish modeling criteria and test techniques required for proper simulation of full-scale recirculation and ingestion phenomena in small-scale investigations, and (2) to gain a better understanding of the recirculating flow fields. The NASA Project Manager was Nestor Clough, of the Lewis Research Center Special Projects Division.

The investigations were conducted with a small-scale engine pod model in which both dual turbojet and turbofan engines were simulated and with a geometrically similar full-scale engine pod containing dual turbojet engines. Potential ingestion control concepts (which were limited to investigation in the small-scale tests) included (1) concepts designed to alter the issuing exhaust jets such as exhaust vectoring and jet suppression nozzles which promote rapid mixing of the exhaust gases with the external ambient environment, (2) shielding devices integral with the engine pod which deflect the reflected upwash gases away from the inlet, and (3) ground surface configurations or devices which alter the impingement process of the exhaust jet on the ground so that the potential upwash is laterally removed from the engine proximity.

Prior to performing the small-scale investigation of various ingestion control concepts, it was essential that the validity of small-scale investigations of recirculation and ingestion phenomena be demonstrated more thoroughly than has been demonstrated heretofore. Thus, full-scale and small-scale tests with geometrically similar configurations (and with similar instrumentation) were conducted prior to the investigation of ingestion control concepts. Detailed comparisons of the data obtained for the full-scale and small-scale configurations are reported herein.

TABLE OF CONTENTS

SCALING OF VTOL RECIRCULATION EFFECTS

By

Gordon R. Hall
Northrop Corporation, Hawthorne, California

SUMMARY

Detailed comparisons of recirculation effects of a full-scale VTOL lift engine pod with YJ-85 engines and a geometrically similar small-scale pod with simulated engines have been made. The pods contained two engines spaced approximately seven diameters apart. Test conditions, instrumentation, and data reduction and analysis techniques were similar for the full-scale and small-scale pods. Comparisons were made of the free jets, ground jets, upwash, and hot gas ingestion into the engine inlets. The results indicate that the overall near flow field, external thermal environment, and hot gas ingestion are scalable, in terms of both dynamic and time-average characteristics, for the same exhaust pressure/temperature in full scale and small scale.

For both the full-scale and small-scale tests, significant ingestion of hot gases was found to occur in one engine or the other during two engine operation, but not in both simultaneously. For single engine operation, both full-scale and small-scale tests showed low level ingestion.

For two engine operation, ingestion characteristics of both full-scale and small-scale tests were found to be highly sporadic, exhibiting closely spaced temperature spikes which typically persist for a small fraction of a second. Due to the sporadic nature of the inlet thermal environment, various statistical representations were required in order to quantitatively characterize the dynamic and time-average properties of the data.

Frequency analyses showed that the full-scale/small-scale inlet temperature fluctuations are dynamically similar when compared on a time-scaled basis. Specifically, power density spectra of the full-scale and small-scale temperature fluctuations were found to be in excellent agreement when compared in terms of the non-dimensional frequency (i.e., Strouhal number), fD/U_o. That is, for the same nozzle exit velocity, the small-scale time scale is compressed such that the frequency of the temperature

fluctuations (and other events associated with unsteady turbulent phenomena within the flow field) occurs at a higher rate than the corresponding full-scale fluctuations, the time scale factor being equal to the size scale factor between the model and the full-scale test vehicles.

Comparisons were made of various full-scale/small-scale hot gas ingestion indices yielding information on the inlet temperature levels, temperature distortion, and temperature gradients. These comparisons showed good full-scale/small-scale agreement in the instantaneous characteristics of the various indices, in the amplitude distribution (i.e., probability density) of the indices, and in the effect of pod height above the ground plane on the time-average values of the indices.

Comparisons of the full-scale/small-scale external environment were also made. Specifically, comparisons were made of the lateral spreading and axial decay characteristics of the free jets, of the pressure and temperature profiles within the ground jet, and of the upwash strength and thermal environment. These comparisons indicate that the overall near flow field and thermal environment are scalable.

INTRODUCTION

Recirculation of exhaust gases in large-scale jet lift VTOL models has been the subject of several recent investigations (References 1-6). These investigations have generally shown that recirculation effects (viz. exhaust gas ingestion and induced aerodynamic forces) are highly dependent upon the vehicle configurations and can, indeed, be a serious problem -- especially for split engine configurations in which an upwash, or fountain, of hot gases is developed as a result of the interaction of opposing ground jet flows.

While full-scale investigations of recirculation effects of specific configurations provide guideline information useful in synthesizing future VTOL aircraft configurations, they cannot provide generalized design data which would allow confident prediction of the ingestion characteristics and induced aerodynamic forces for an arbitrary VTOL aircraft. That is, extrapolation of data to configurations other than the actual configuration tested is not reliable due to the fact that major changes in exhaust gas ingestion and induced aerodynamic forces have been found to occur from what would seem to be minor changes in aircraft configurations. As a result, new VTOL configurations evolved from design studies need to be tested for ingestion and induced aerodynamic characteristics. With such evaluations required, small-scale simulations yielding results applicable to geometrically similar full-scale vehicles are highly desirable in order to avoid costly full-scale testing during the preliminary design stages of VTOL aircraft.

Although a detailed examination of the fundamental transport equations in a viscous fluid and a detailed review of experimental results of turbulence phenomena associated with jet mixing and entrainment indicate that VTOL recirculation effects are scalable, comprehensive quantitative comparisons of full-scale and small-scale experimental data which convincingly demonstrate the scalability of recirculation phenomena have not been made heretofore (e.g., Reference 7). On the contrary some past attempts to compare full-scale and small-scale experimental data have produced negative results (e.g., Reference 1), although for reasons which can be explained in terms of model simulation techniques, test techniques, and instrumentation rather than being fundamental to the physics of the problem (e.g., Reference 8).

Reported here are direct comparisons of full-scale and small-scale recirculation effects which demonstrate that VTOL recirculation phenomena are scalable, in terms of both dynamic and time-average characteristics. The full-scale "reference" data used for the comparisons were provided from the investigation of the lift engine pod reported in Reference 5. The small-scale data were obtained using a 1/5 scale geometrically similar model. Test conditions, instrumentation location, sensing elements, recording instruments, data reduction techniques, and data analysis techniques were similar for the full-scale and small-scale investigations.

SYMBOLS

D	nozzle diameter
f	frequency
h	height from ground plane
H	height of pod undersurface from ground plane
ΔP	pod pressure minus ambient pressure
q	jet stagnation pressure minus ambient pressure
q_n	nozzle stagnation pressure minus ambient pressure
T	temperature indicated by an individual thermocouple
ΔT	temperature increment above ambient temperature, $T - T_\infty$
U_o	jet exit velocity
X	lateral displacement from pod longitudinal centerline
Z	vertical distance from nozzle exit
σ	RMS fluctuation

Ingestion Indices

$\bar{T}$	instantaneous spatial average inlet temperature, $\bar{T} = \frac{1}{n}\sum_{n=1}^{n} T_i$, where n equals number of inlet thermocouples
$\Delta\bar{T}$	instantaneous spatial average inlet temperature increment above ambient, $\bar{T} - T_\infty$
ϵ_{max}	instantaneous temperature distortion within inlet, $T_{max} - T_{min}$
$\dot{\bar{T}}$	instantaneous rate of rise of spatial average inlet temperature

Superscript

$\wedge$	time-average (applied to $\Delta\bar{T}$, ϵ_{max}, and $\dot{\bar{T}}$)

TEST FACILITY AND MODEL

Full-Scale

Test Facility

The full-scale tests were performed at the NASA-Ames Research Center VTOL Ground Effects Test Facility (Figures 1 and 2). This facility is an outdoor complex designed to support powered VTOL models in static tests. The complex consists of a fixed 78'x 80' ground plane and a model support structure. The support structure is mechanized to provide variation of model height above the ground plane and angle of attack.

Model

The full-scale test vehicle was the lift engine pod model shown in Figures 1 and 3. The pod was designed to accommodate four General Electric YJ-85 engines, although for the tests reported here only two engines were utilized. The spacing between the two engines, S, in terms of the 12.5 inch YJ-85 engine nozzle diameter, D, was $S/D = 7.3$. The nominal exhaust pressure ratio was $P_n/P_\infty = 1.8$ and nominal exhaust temperature $T_n = 1100^\circ F$.

The pod was mounted to the test facility support struts by a horizontal support beam normal to the longitudinal axis of the pod and by a toggle mechanism located at the vehicle nose. The main support beam was located ahead of the forward engine so as not to interfere with the upwash flow between the engines.

Alignment of the engine axes normal to the longitudinal axis of the pod was accomplished by rotation of the engines about the engine mounts. This longitudinal alignment, which was considered to be critical based on the results of the small-scale investigation of Reference 9, was subsequently checked by measurements of the exhaust flows issuing from the nozzles.

Small-Scale

Test Facility

The small-scale tests were performed at Northrop Corporation, Aircraft Division, VTOL Ground Effects Test Facility. A brief description of this facility is given below, with Reference 10 providing details of the design features and performance capabilities.

Figures 4 and 5 show the facility and model support system. Test models are centrally located with respect to a 40'x40' smooth and level ground plane located 30" above earth level. Directly below the model is a 14"x30" trap door through which the exhaust jets flow during temperature stabilization of the model and ducting system. Beneath the trap door is a deflector which diverts the exhaust flow outward beneath the ground plane.

Test models are mounted on a cantilever structure supported by a tripod base. Simulated engine exhaust flow is supplied from bottles of compressed air (Figure 4) and is heated to the desired exhaust temperature in passing through a pebble bed heater enroute to the model. Simulated engine inlet flow is induced by a vacuum system. The model exhaust and inlet flows are routed along and through, respectively, the support structure. Vertical position (or continuous motion) of the model is accommodated by telescoping assemblies in the exhaust nozzle supply lines and by flexible hose in the inlet suction lines.

The test area is large enough, and sufficiently vented, to avoid heating of the local "external" environment during periods of sustained testing. Additionally, all vertical obstructions are far enough removed from the exhaust jet source to avoid "jet reflection" effects. Wind protection in the test area is afforded by surrounding buildings and by installation of canvas wind screens (15' high) at the north and west ends of the test area as indicated in Figure 4. With the wind screens installed, local wind conditions within the test site are suppressed to levels typically less than 3 MPH during the morning and early afternoon.

Airflow to simulate wind effects is supplied from a 9'x12' duct which terminates near the edge of the ground plane. The drive system of the wind generator is an ejector concept which provides secondary to primary airflow in the ratio of about 80 to 1, the secondary air being drawn from the atmosphere and the primary air being provided by the same bank of compressed air which supplies the model exhaust flow.

Model

The small-scale model is shown in Figures 6 and 7. The model scale was approximately 1/5 in terms of relevant geometric parameters such as inlet diameter, nozzle exhaust diameter, "engine" spacing, pod height, and pod width.

The inlets and exhaust nozzles of the model contained centerbodies in order to provide close simulation of the full-scale inlet and nozzle flows. The inlet flow rate, with the inlets operating at the nominal inlet Mach number of 0.5, was approximately equal to the exhaust nozzle flow rate, when operating at the nominal exhaust pressure ratio of $P_n/P_\infty = 1.8$ and exhaust temperature of $T_n = 1100^\circ F$ (i.e., same exhaust conditions as full-scale tests).

Internally, the upper portion of the model served as a duct in routing the inlet flow out of the model. Internally, the lower portion of the model served as the exhaust flow supply duct. A perforated plate (.05" holes) was used to separate the exhaust flow supply duct from the nozzle chamber. The plate served to drop the pressure between the supply duct ($\approx$ 80 psia) and the nozzle chamber ($\approx$ 26 psia), thereby allowing a smaller supply duct cross section than would otherwise be required. The plate also eliminated problems of exhaust flow alignment which would have been severe without the plate.

Inlet suction and exhaust flow were supplied at each end of the model with an internal partition separating the forward "engine" flow from the aft "engine" flow. Air suction systems at each end of the model were essential in order to attain the desired inlet flow without geometric distortion of the model, distortion being necessary to accommodate the duct size required for a "single end" suction system.

Heat absorption by the model (and therefore model heating and cooling time) was minimized by insulating the model structure from the hot exhaust flow. The insulation resulted in maximum model structure temperatures (with exception of the nozzle) of about 400°F.

INSTRUMENTATION

Identical instrumentation (and instrumentation location) was selected for the majority of the full-scale and small-scale measurements. Instrumentation common to both the full-scale and small-scale tests is described below.

1. Inlet Temperatures - The inlets of the pods were instrumented with twelve high response bare bead thermocouples. The locations of the thermocouples were selected to represent equal flow areas within the inlet. The output of these thermocouples were recorded on FM magnetic tape.

The locations and details of construction of the inlet thermocouples are shown in Figure 8. The sensing element of the thermocouples was fabricated from .003" chromel/alumel wire. Based on Reference 11, the time constant for the thermocouple/flow environment combination was approximately 18 m.s. (or in terms of response to a sinusoidal input signal, flat response within 10 percent up to a frequency of about 5 cps), assuming an ideal butt weld junction through which the local thermal mass is not increased above that of the parent wire. Details of the design considerations relating to the construction concept, junction wire size, junction material, and operational reliability are given in Reference 5.

2. Inlet Proximity Temperatures - Twelve high response bare bead thermocouples (identical to those in the engine inlets) were cantilevered from the sides of the engine pods near the plane of the inlets (Figure 9). These thermocouples, which were recorded on oscillograph, were located to measure the temperature (and longitudinal concentration) of the upwash flow between the engines.

3. Ground Jet Pressures and Temperatures - A vertical rake was positioned as shown in Figure 10 to measure the ground jet pressure and temperature profiles in the interaction plane of the jets. The rakes consisted of an array of total pressure probes, static pressure probes, and temperature probes extending from the ground plane to about three nozzle diameters above the ground plane.

4. Engine Pod Pressures - Six pressure taps were located on the lower surface of the pods along the longitudinal centerline (Figure 11). These pressure measurements provided information on the strength and location of the upwash flow between the engines.

5. Exhaust Measurements - Exhaust nozzle pressure and temperature for the

full-scale and small-scale pods were measured with high response sensing elements (four per nozzle in full scale, three per nozzle in small scale) and recorded on oscillograph.

6. External Wind - External wind speed, azimuth, and elevation were monitored prior to testing and recorded continuously on oscillograph during the tests.

PROCEDURE

Test Procedure

Table 1 presents a list of the full-scale and small-scale tests used for the various comparisons presented herein. Prior to conducting each of the tests, external wind conditions were monitored until satisfactory conditions were attained. For the nominally "no wind" tests, wind conditions were less than 4 MPH within the test area. For the full-scale "wind" tests, natural winds of about 16 MPH were experienced, blowing nominally from the north (i.e., aligned with the pod, Figure 2). For the small-scale "wind" tests, wind speed and direction were controlled using the wind generator described previously. For these tests, a head wind (with respect to the model) was set at 16 MPH.

TABLE 1. TEST CONDITIONS

Engines Operating	Pod Height H/D	Wind Velocity
2 ↓	2 3 4 6 8	<4 MPH ↓
2	4	16 MPH (aligned with pod)
1	4	<4 MPH
1	4	16 MPH (aligned with pod)

Full-Scale

Once the desired wind condition was attained, the aft engine was started and brought to the nominal idle condition (viz. 50 percent RPM). For "two engine" tests, after stabilizing engine #4 at the idle condition, engine #1 was started and brought to idle condition, after which time data acquisition was initiated. The two engines were then simultaneously accelerated to "full power" (viz. 98 percent RPM), the acceleration requiring approximately 5 seconds with engine #4 typically requiring about one second more than engine #1. At the steady state full power condition, the exhaust pressure ratios were about 1.8 and exhaust temperatures about 1100°F. A typical exhaust pressure and temperature history is shown in Figure 12.

For single engine tests, after stabilizing engine #4 at the idle condition, data acquisition was initiated, followed by acceleration of the engine to full power.

Small-Scale

For the small-scale tests, the inlet suction system was set to give an inlet Mach number of 0.5, after which time the model and test facility ducting was preheated to provide an exhaust temperature of 1100°F at a model pressure ratio of 1.8 (i.e., exhaust pressure and temperature same as for full scale). Upon establishing the desired exhaust conditions, the wind generator was set to give a 16 MPH head wind (for wind tests only), after which time data acquisition was initiated and the ground plane trap door was closed. The trap door closure time was about 150 m.s. Data acquisition subsequent to trap door closure was typically 40 seconds.

Ambient Temperatures

For the full-scale tests, the ambient temperature level was typically about 40°F. These tests were conducted in the early morning hours of December at Ames Research Center.

For the small-scale tests, the ambient temperature level ranged from about 60°F to about 90°F. These tests were conducted during the summer at Northrop Corporation, Aircraft Division.

Although much of the temperature data presented in the sections which follow are referenced to the ambient level, some of the data are presented at absolute levels. In reviewing these data, the ambient temperature difference between the full-scale and small-scale tests should be kept in mind.

Data Reduction

Identical data reduction techniques were applied to the inlet temperature data of the full-scale and small-scale tests. In general, the techniques employed were oriented toward a statistical analysis of the inlet thermal environment due to the random, or sporadic, nature of the inlet temperature data. For data of this type, a statistical oriented approach to data analysis is essential for objective characterization of the data.

As noted previously, the inlet temperatures were sensed with high response thermocouples and recorded on magnetic tape. For each of the full-scale and small-scale tests, the raw inlet temperature data were played back on analog tapes. In addition, the following temperature indices, yielding quantitative information on the inlet temperature levels, spatial distortion, and temperature gradients, were computed from the raw data using a Comcor 175 Analog Computer.

(1) The instantaneous spatial average of the n individual temperatures within the inlet:

$$\overline{T}(t) = \frac{1}{n}\sum_{i=1}^{n} T_i(t)$$

(2) The cumulative time-average of (1).

(3) The instantaneous maximum temperature distortion within the inlet:

$$\epsilon_{max}(t) = T_{max}(t) - T_{min}(t)$$

(4) The cumulative time-average of (3).

(5) The instantaneous rate of rise of (1):

$$\dot{\overline{T}}(t) = \frac{d\overline{T}}{dt}$$

(6) The cumulative time-average of the absolute value of (5).

The above defined full-scale/small-scale ingestion indices are presented in the Appendix for each of the tests of Table 1. In addition, time histories of the raw inlet temperature data are provided for selected tests.

Data reduction providing quantitative characterization of the inlet temperature fluctuations, in the form of power spectral density plots and probability density plots, was also performed using the analog computer and random data analysis equipment.

DISCUSSION

Scope of Analysis

The primary purpose of this report is to compare full-scale and small-scale recirculation data of similar lift engine pod configurations, identically instrumented, and operating in ground proximity. The intent is to demonstrate that small-scale tests, if properly conducted, can give test results representative of full-scale configurations.

Considering the above objective, it is not the intent to analyze and discuss trends of ground proximity phenomena as this is done extensively in Reference 5 which separately reports the full-scale tests, and will be done in a forthcoming report which separately reports the small-scale tests. Rather, the discussions presented concentrate on the direct comparison of test data at test conditions common to both the full-scale and small-scale programs. Accordingly, analyses of the physics of the ground proximity phenomena have generally been limited to discussions which are complementary to the full-scale/small-scale comparisons. Liberal reference to other work is provided at appropriate points for those interested in additional detail.

The material presented in the sections which follow, although concentrating on hot gas ingestion characteristics, also include exhaust jet calibrations, ground jet pressure and temperature profiles, and pod pressure distributions. Additional data, comparing full-scale and small-scale ingestion characteristics from each of the tests of Table 1, are presented in the Appendix.

Exhaust Jet Calibration

Prior to conducting the full-scale/small-scale tests, calibrations of the jet exhausts were made. These calibrations are relevant to subsequent comparisons of full-scale/small-scale recirculation effects. This was borne out in the findings of Reference 9 which demonstrated that recirculation effects are extremely sensitive to jet exit angles and moderately sensitive to jet dynamic pressure decay (i.e., turbulence) characteristics. Thus, in any attempt to simulate full-scale recirculation effects in small scale, it is essential that full-scale/small-scale jet alignment and dynamic decay characteristics be closely matched.

Dynamic pressure profiles (i.e., jet total less ambient pressure) of the full-scale/small-scale jets were measured at various distances, Z, from the nozzle exit using a cruciform pressure rake with probes aligned to measure the jet pressure profiles in the fore/aft plane and in the right/left plane. Measurements were made from the nozzle exit up to Z/D about 10, with the rake aligned such that the centerprobe of the cruciform was coincident with a plumb line suspended from the nozzle centerline. The measurements were taken at the nominal values of nozzle pressure ratio and nozzle temperature of $P_n/P_\infty = 1.8$ and $T_n = 1100°F$, respectively. The dynamic pressure profiles obtained were found to be similar for the full-scale and small-scale jets, both in lateral spreading characteristics and axial decay characteristics.

The dynamic pressure profiles, q, non-dimensionalized with respect to the dynamic pressure measured within the nozzle, q_n, are shown in Figures 13 (full scale) and 14 (small scale). The depression in the dynamic pressure in the central region of the jets at lower values of Z/D is indicative of flow separation from the nozzle centerbody, the small-scale data (Figure 14) indicating a somewhat greater centerbody effect than the full-scale data (Figure 13). At larger values of Z/D, the relatively localized effects of the centerbody are not apparent, with the full-scale and small-scale profiles resembling a distribution characteristic of the asymptotic profiles for a conventional open nozzle.

At the larger values of Z/D, a small offset of the dynamic pressure peak from vertical (i.e., $r/R = 0$) is generally observed in Figures 13 and 14. These offset values in the dynamic pressure profiles were used to determine the alignment of the jets relative to vertical, assuming the jet centerline to be defined by the locus of the dynamic pressure peaks. Based on this method, the maximum mis-alignment of the full-scale/small-scale jets relative to vertical was determined to be less than 1 degree.

Figure 15 shows the variation in jet centerline dynamic pressure with Z/D for the full-scale and small-scale jets. Excellent agreement for the rate of decay of the full-scale/small-scale jets is indicated at the higher values of Z/D. At the smaller values of Z/D, the more pronounced effect of the small-scale centerbodies is again evident.

Ingestion Characteristics

Two Engine Operation

Figures 16 and 17 show the inlet temperature environment from the full-scale and small-scale tests, respectively, for two engine operation at H/D = 4 and low wind conditions. The data were obtained by playback of the raw data from magnetic tape. From the point of view of comparing full-scale/small-scale characteristics, the data of Figures 16 and 17 are typical of other values of H/D.

Ingestion Asymmetry - For two engine operation, in which exhaust gas ingestion is dominated by the upwash, or fountain, resulting from mutual interaction of the jets and the ground plane, several general characteristics common to both the full-scale and small-scale data are immediately obvious. First of all, in reference to Figures 16a and 17b (i.e., engine #1 in full scale and aft inlet in small scale), it is observed that beyond approximately the first five seconds in Figure 16a (the time required to establish full power in the full-scale tests), and beyond t = 0 in Figure 17b (time of trap door closure in the small-scale tests), the inlet thermal environment is significantly above ambient temperature. In contrast, Figures 16b and 17a (i.e., engine #4 in full scale and forward inlet in small scale) show an essentially ambient inlet thermal environment except for occasional temperature spikes after establishment of full power in the full-scale tests and after trap door closure in the small-scale tests. Prior to establishment of full power in the full-scale tests, significant ingestion is observed in engine #4 due to the unequal acceleration of the two engines indicated in Figure 12.

Nonsymmetrical distribution of exhaust ingestion by the inlets was found to be typical of both full-scale and small-scale tests at other values of H/D as well as throughout a much broader range of operating variables on various full-scale and small-scale tests not specifically reported herein. Due to the geometric symmetry of the full-scale/small-scale engine pods in the region between the inlets, the ingestion prone engine or inlet (i.e., engine #1 or engine #4 full scale, forward inlet or aft inlet small scale) was found to vary from test to test.

In all the full-scale tests, the initial ingestion prone engine was found to remain the ingestion prone engine throughout the test. In a few small-scale tests, however, most of which do not have full-scale counterparts due to dissimilar model and/or test conditions, the ingestion was found to shift from one inlet to the other within the test. Thus, although there would seem to be some differences in the degree of stability of the nonsymmetrical ingestion phenomena, full-scale and small-scale tests are in agreement in generally exhibiting this phenomenon. Additional discussion of the physics of nonsymmetrical ingestion, including a discussion of the increased stability of the nonsymmetrical full-scale ingestion relative to small-scale ingestion, is given in Reference 5.

Gross Fluctuation Characteristics - Another obvious characteristic common to the full-scale/small-scale data of Figures 16a and 17b is the sporadic nature of the inlet temperature environment of the ingestion prone engine. Temperature spikes are observed in both the full-scale and small-scale data which typically persist for a small fraction of a second, and frequently reach levels in excess of 100°F above ambient. These temperature spikes, or pulses, are sometimes very local in nature as evidenced by simultaneous response of only few thermocouples, while at other times they are observed to encompass a large section of the inlet as evidenced by simultaneous response of the majority of the thermocouples. During time intervals between temperature spikes, the temperature level is typically ambient, with the full-scale data exhibiting dwell periods at the ambient level longer than the small-scale data. In no case was a prolonged temperature rise observed in either the full-scale or small-scale tests which could be considered a "steady" temperature, rather than a series of closely spaced temperature pulses. The "return to ambient" characteristic of the raw inlet temperature data, observed first in the full-scale tests, is discussed at length in Reference 5. Detailed analysis and comparison of the full-scale/small-scale inlet temperature fluctuations are presented later under "Temperature Fluctuation Analyses."

Single Engine Operation

In contrast to the data of Figures 16 and 17 (typical of operation with two engines) are full-scale/small-scale data of Figures A7-3 and A7-4, typical of operation with a single engine. For single engine operation at low wind conditions, the engine exhaust strikes the ground, spreads radially along the ground, and eventually rises as a result of buoyancy forces. The resulting ingestion level is essentially negligible, with peak temperatures generally less than 5°F above ambient for both the full-scale and small-scale tests, although for the full-scale data of Figure A7-3, somewhat higher temperatures are indicated during the period of engine acceleration prior to t = 3 seconds.

Effect of Wind

Full-scale and small-scale tests were also conducted at "high" wind conditions. Figures A6-3 and A6-4 show the inlet temperature data for two engine operation at H/D = 4 and a wind speed of nominally 16 MPH aligned with the pod. Both full-scale and small-scale data show a major reduction in ingestion levels from the low wind condition of Figures 16 and 17.

Further, for both full-scale and small-scale tests, the engines upstream with respect to the wind (i.e., engine #4 in full scale and forward inlet in small scale) show minor temperature pulses of about 10°-15°F distributed over the entire inlet, rather than localized as for the case of operation at low wind conditions. The distributed temperature pulse indicates a well mixed flow of exhaust gases which are swept up from the ground plane in the far field and blown back over the pod.

In contrast, the downstream engines (i.e., engine #1 in full scale and aft inlet in small scale) show occasional sharp localized spikes, typically 25°-100°F. The sharp spikes indicate an upwash which, although predominately suppressed and deflected by the wind, is occasionally entrained within the inlet flow.

Figures A8-3 and A8-4 compare full-scale and small-scale data for single engine operation at wind conditions similar to those of Figures A6-3 and A6-4 for two engine operation. The full-scale and small-scale data are similar in showing ingestion characteristics much like the upstream engine for two engine operation at wind conditions. Namely, temperature pulses of about 10°-15°F are frequently observed, the pulses being distributed over the entire inlet.

Ingestion Indices

Figures 18 through 23 present data on the full-scale/small-scale inlet temperature environment for two engine operation in terms of the various ingestion indices defined previously under "Data Reduction." Although the data of Figures 18 through 22 are presented at H/D = 4 (corresponding to the raw data of Figures 16a and 17b), the full-scale/small-scale comparisons which follow are generally representative of other values of H/D.

Instantaneous Indices

Figures 18 and 19 show full-scale and small-scale time histories of the spatial average inlet temperature ($\bar{T}$), the maximum temperature distortion within the inlet (ϵ_{max}), and the rate of rise of the spatial average temperature ($\dot{\bar{T}}$), for two engine operation at H/D = 4. These indices were computed from the ingestion prone engine raw data of Figures 16a and 17b (i.e., engine #1 full scale, aft inlet small scale) using an analog computer. Similar data are presented in the Appendix for each of the tests listed in Table 1.

From the graphs of $\bar{T}$, it is seen that the average inlet temperature is essentially ambient (with the exception of a few minor temperature pulses) prior to $t \approx 5$ seconds for the full-scale test (i.e., time to reach full power), and ambient up to $t = 0$ for the small-scale test (i.e., time of trap door closure). Beyond $t \approx 5$ seconds in the full-scale test and $t = 0$ in the small-scale test, the full-scale and small-scale data are generally in good agreement, both in the character of the data and in the temperature rise above ambient (note that the ambient temperature level in the full-scale test was about 40°F while that in the small-scale test was about 90°F). Significant oscillations in $\bar{T}$ are observed, reaching instantaneous levels approximately 50°F above ambient in both the full-scale and small-scale tests.

Since the temperature spikes observed in the raw data are generally localized, peak values of $\bar{T}$ are accordingly significantly less than the localized peak values of the individual temperatures observed in the raw data (Figures 16a and 17b). Thus $\bar{T}$, while still rather sporadic in nature, is considerably smoother than the individual temperature traces of the raw data.

Turning to the temperature distortion indices, ϵ_{max}, of Figures 18 and 19, it is seen that the instantaneous temperature distortion of both the full-scale and small-scale tests is highly sporadic, with the full-scale data indicating somewhat higher levels of distortion. Large values of distortion are frequently observed in both the full-scale and small-scale data without significant increase in $\bar{T}$, again illustrating the local nature of the hot gas ingestion. This is particularly evident during the 5 seconds of the full-scale test prior to reaching full power.

Amplitude Distribution

Figure 20 shows the amplitude distribution (i.e., probability density) of the time varying ingestion indices $\Delta\bar{T}$, ϵ_{max}, and $\dot{\bar{T}}$ of Figures 18 and 19, computation beginning once full thrust level of the engines was established in the case of the full-scale test and following trap door closure for the small-scale test.

Representation of fluctuating data of the type shown in Figures 18 and 19 in terms of the probability density function shows the relative time, or probability, that the data fall within a particular amplitude range. In the standard representation of probability density, the amplitude of the data (abscissa on the probability density plot) is normalized in terms of the RMS fluctuation of the data, σ , about the mean value of the data (corresponding to $\sigma = 0$). The ordinate of the probability density plot, $p(\sigma)$, is then a measure of the relative time, or probability, that the data fall within a particular amplitude range. The integral of the probability density function is unity since all of the data fall within the amplitude range of the probability density function. The most common probability density function of random data is the familiar Gaussian distribution, or bell-shaped curve, which is symmetrical about the mean value of the data (i.e., $\sigma = 0$) and with virtually all the data (i.e., 99.7 percent) falling within the amplitude range $\pm 3\sigma$ (i.e., peak fluctuation levels three times the amplitude of the RMS fluctuations). Deviation from Gaussian distribution in the way of skewed distributions indicates data of a "spikey" nature in which narrow high amplitude spikes are distributed predominately on one end of the amplitude range. For a detailed mathematical description of the probability density function, the reader is referred to Reference 12.

Figure 20a shows the full-scale/small-scale distributions of $\Delta\bar{T}$. The distributions are similar, both being skewed in the direction of the ambient temperature level with the most probable value of $\Delta\bar{T}$ being less than the mean value. That is, most of the time is spent at temperature levels below the mean value.

Figure 20b shows the full-scale/small-scale distributions of ϵ_{max}. The full-scale distribution is seen to be relatively symmetrical about the mean value while the small-scale distribution is skewed somewhat toward lower values.

Figure 20c shows the full-scale/small-scale distributions of $\dot{\bar{T}}$. The distributions are in good agreement, both being symmetrical about the mean value of $\dot{\bar{T}}$ (note that the mean value of $\dot{\bar{T}}$ is zero unless there is a net increase in $\Delta\bar{T}$ with time). Additionally, both distributions exhibit rather narrow spectra, the narrow spectra indicating that the majority of the time is spent at relatively low levels of $\dot{\bar{T}}$ relative to the maximum levels of $\dot{\bar{T}}$.

In summary, not only do the full-scale/small-scale qualitative fluctuations of $\Delta\bar{\bar{T}}$, ϵ_{max}, and $\dot{\bar{\bar{T}}}$ appear similar as indicated in Figures 18 and 19, but the actual quantitative distributions of the fluctuations about the mean level are essentially the same as indicated in Figure 20.

Cumulative Time-Averages

The instantaneous temperature indices for each of the tests were cumulatively time averaged in order to provide a single run-average index for each of the fluctuating quantities $\bar{\bar{T}}$, ϵ_{max}, and $\dot{\bar{\bar{T}}}$. These time-average quantities were obtained by continuous integration and division by time using an analog computer, the computing process beginning once full thrust level of the engines was established in the case of the full-scale tests and following trap door closure for the small-scale tests. For the case of $\dot{\bar{\bar{T}}}$, the integral taken was that of the absolute value rather than of the algebraic value (the integral of the algebraic value of $\dot{\bar{\bar{T}}}$ must be zero unless there is a net increase in $\bar{\bar{T}}$ with time).

Figures 21 and 22 show the cumulative time-averages $\hat{\bar{\bar{T}}}$, $\hat{\epsilon}_{max}$, and $|\hat{\dot{\bar{\bar{T}}}}|$ of the instantaneous data of Figures 18 and 19, the hat over the quantity indicating the cumulative time-average. As can be seen, the cumulative time-averages of both the full-scale and small-scale are essentially independent of time, except during the initial stages of the computation where the time interval which is divided into the integral is not sufficiently large (say, $t \lesssim 1$ second) to dampen the individual oscillations. That is, although the quantities $\bar{\bar{T}}$, ϵ_{max}, and $\dot{\bar{\bar{T}}}$ are of a sporadic nature on a short time basis, both full-scale and small-scale results showed no net change (i.e., no "long time" time-dependence) in the average value of these quantities over the duration of the tests.

Effect of H/D

Figure 23 shows the variation with H/D of the full-scale/small-scale time-average ingestion indices $\Delta\hat{\bar{\bar{T}}}$, $\hat{\epsilon}_{max}$, and $|\hat{\dot{\bar{\bar{T}}}}|$. These indices provide a single number representative of the inlet temperature level (referenced to ambient temperature), temperature distortion, and rate of temperature rise for a given test. As such, they provide a direct measure of the severity of the hot gas ingestion for a given test.

The period of the time-averaging computation for the indices was 30 seconds, although as indicated in Figures 21 and 22, the period of computation is not critical in that there is virtually no net change in the various indices with time.

The full-scale and small-scale results of Figure 23 are seen to be in good agreement, even to the extent of indicating a minor hump in the curves in the region between H/D = 3-5. Further, both full-scale and small-scale data agree in indicating major reduction in ingestion levels with a head wind of 16 MPH.

The full-scale/small-scale agreement is especially encouraging considering the sporadic nature of the raw data and the fact that repeatability of results under "identical" conditions from either full-scale or small-scale tests is no better than about ±10 percent. Thus, not only are the instantaneous ingestion indices similar as discussed above, but the time-average values of these indices are also in good agreement as demonstrated in Figure 23. It is of interest to note that the general shapes of the curves for the various indices are similar, thus indicating that any one of the indices would serve as a relative indicator of the severity of the hot gas ingestion.

Temperature Fluctuation Analyses

As discussed previously, the full-scale/small-scale inlet temperature raw data were found to be qualitatively similar in exhibiting fluctuation characteristics. However, quantitative analyses are essential to determine if a scaling relationship exists between the full-scale and small-scale temperature fluctuations. The importance of establishing a quantitative scaling relationship is that significant instantaneous reduction in engine stall margin can result from temperature fluctuations of the amplitudes and frequencies observed in the full-scale/small-scale data. Thus, an essential part of the data analysis from small-scale ingestion tests representing full-scale VTOL configurations is to relate the measured small-scale temperature fluctuations in terms of the full-scale vehicle being simulated. Accordingly, detailed quantitative analyses of the temperature fluctuations and general studies of scaling of turbulence phenomena were carried out to establish a scaling relationship between the full-scale/small-scale fluctuations. Although much of the detail of these analyses and studies is beyond the scope of this report, a brief account and some results are presented in the paragraphs which follow.

Thermocouple Time Constant

To begin with, in order to make meaningful quantitative comparisons of the full-scale/small-scale dynamic temperature fluctuations, it is essential to establish whether or not the recorded data are true representations of the actual instantaneous temperature environment. Following Reference 10, the actual temperature is related to the temperature measured by the thermocouple through the simple relation:

$$T_{act} = T_{meas} + \tau \dot{T}_{meas} \qquad (1)$$

where τ is the thermocouple time constant. As can readily be seen, the measured temperature will approach the actual temperature only if the thermocouple time constant is small and/or the gradient of the temperature is low. Thus, from thermal response considerations, one would like to make the thermocouple time constant arbitrarily small.

Other physical considerations, however, such as component fabricability, cost, and reliability, are limiting. The problem of thermocouple selection, then, is to minimize the sensing element wire diameter in order to enhance response characteristics (i.e., time constant $\tau \alpha d^{3/2}$) without serious compromise in the mechanical integrity of the element when installed in the relatively high acoustic, vibration, and velocity environment of an engine inlet. Based on simple endurance/reliability tests of various thermocouples, a wire size of .003" (τ nominally 18 m.s.) was selected for the full-scale/small-scale tests.

Although the nominal thermocouple time constant was 18 m.s. (based on the theoretical analysis of Reference 11), a more accurate method of assessing the actual time constant was devised. This method involved arbitrarily selecting an artificial value of time constant (designated τ_o), and then solving Equation (1) on an analog computer using the measured temperature history, the solution being an artificial time history of the "actual" temperature, $T_{act\ o}$. Then, working with the values of T_{meas} and $T_{act\ o}$, and their respective gradients, at specific points in the time history, it was possible to determine the actual value of τ. Excellent consistency for values of τ was obtained by this method. This consistency was demonstrated by comparing values of τ obtained: (1) at different points within a given temperature history; (2) for different initial arbitrary values of τ_0; and (3) from different thermocouple time histories of the same test.

The results indicated thermocouple time constants for the full-scale tests typically within a few milliseconds of the nominal 18 m.s. value. For the small-scale tests, however, the results indicated time constants typically about 30 m.s. Physical examination of the full-scale/small-scale thermocouples clearly indicated the reason for the difference in the full-scale/small-scale time constants: the full-scale thermocouples were in a relatively virgin condition throughout the full-scale tests while the small-scale thermocouples had accumulated a coating of foreign material as a result of being subjected to considerably more test time than the full-scale thermocouples.

Corrected Time Histories

Using the thermocouple time constant determined as described above (viz. 18 m.s. for the full-scale tests and 30 m.s. for the small-scale tests) and the measured time history, the corrected (actual) time history, T_{act}, was obtained from Equation (1) for several samples of raw temperature data from the full-scale/small-scale tests. The full-scale data were affected very little by the correction, while the correction to the small-scale data was found to be significant. Typical results are shown in Figure 24 for thermocouples at the same relative position within the ingestion prone inlets for two engine operation at H/D = 4. Considerably higher frequency content for the corrected (i.e., T(actual)) small-scale data than for the uncorrected (i.e., T(measured)) small-scale data is observed. The larger correction for the small-scale data relative to the full-scale data is the result of the higher time constant and higher temperature fluctuation frequencies of the small-scale data.

Additional substantiation to the small-scale corrected temperature histories was provided by recirculation tests in which a highly responsive hot wire anemometer (used in the temperature sensing mode) was placed in the inlet immediately adjacent to one of the thermocouples. These tests indicated good quantitative agreement (as demonstrated by comparison of power density spectra) between the temperature fluctuations measured by the hot wire and the corrected temperature fluctuation of the adjacent thermocouple.

Time-Scaled Data

Figure 25 shows a comparison of the corrected full-scale and small-scale temperature histories from Figure 24 with the time scale of the small-scale data expanded by a factor of 5 (i. e., approximate inverse of the model linear scale). This comparison is made in that true dynamic similarity between the full-scale/ small-scale temperature fluctuations implies stretching of the small-scale time scale by the inverse of the model scale, assuming identical jet exhaust conditions at the nozzle exits. Note that when compared on the time-scaled basis of Figure 25, the dynamic characteristics of the full-scale/small-scale data appear quite similar, with similar duration (time-scaled) temperature spikes and similar dwell periods (time-scaled) at ambient temperature level between temperature spikes.

Frequency Scaling

Although the data of Figure 25 show excellent qualitative agreement between the corrected full-scale and small-scale inlet temperature fluctuations when time-scaled by the model linear scale, power spectral density comparisons, which characterize the frequency content of the temperature fluctuations, are required for a quantitative evaluation of whether or not dynamic similarity exists (see Reference 12 for a rigorous mathematical definition of the power spectral density). For true dynamic similarity between the full-scale and small-scale temperature fluctuation characteristics, one would expect the power density spectra of the temperature histories to be the same when non-dimensionalized with respect to the Strouhal number, fD/U_o, as suggested in Reference 7. Figure 26 shows full-scale/small-scale power density spectra of the data of Figure 25 represented in terms of absolute frequency and in terms of non-dimensional frequency (i. e., Strouhal number).

The absolute spectra (Figure 26a) are qualitatively similar in exhibiting a relatively constant amplitude region, followed by a roll-off at nearly constant slope (on the log-log scale). The level of the constant amplitude region is, however, considerably lower for the small-scale spectrum (roughly by the model linear scale), and the roll-off frequency is considerably higher (roughly by the inverse of the model linear scale).

When non-dimensionalized by the Strouhal number (Figure 26b), however, the spectra are virtually identical, thus demonstrating dynamic similarity between the full-scale and small-scale temperature fluctuations in terms of the non-dimensional frequency, fD/U_o. That is, for the same nozzle exit velocity, the small-scale time scale is compressed such that the frequency of the temperature fluctuations (and other events associated with unsteady turbulent phenomena within the flow field) occurs at a higher rate than the corresponding full-scale fluctuations, the time compression factor being equal to the size scale factor between the model and the full-scale test vehicles. This result is what one would have anticipated if the relative size of the turbulent eddies of the upwash flow is preserved between full scale and small scale. Thus, the demonstrated dynamic similarity strongly suggests that the relative eddy size is preserved between full scale and small scale.

Further comparisons at the same nominal conditions of full-scale/small-scale power density spectra of various temperature histories are presented in Figure 27. Again, the small-scale absolute spectra show a lower constant amplitude region than the full scale, roughly by a factor equal to the model linear scale, and a higher roll-off frequency than the full scale, roughly by a factor equal to the inverse of the model linear scale. As before, when non-dimensionalized by the Strouhal number, however, the spectra are quite similar, thus further demonstrating dynamic similarity of the full-scale/small-scale temperature fluctuating as discussed above.

External Environment

Ground Jet Profiles

Two Engine Operation - Upon striking the ground, the individual exhaust jets are turned approximately parallel to the ground, spreading radially outward. The flow of the ground jet continues unimpeded in flowing away from the source except in the region between the impingement points of the two jets for two engine operation. In this region, the flow of the individual ground jets is toward one another, eventually interacting in the plane midway between the impingement points. Within the interaction process, the ground jet flows are turned outward and upward as indicated schematically in Figure 28.

Figure 29 shows full-scale/small-scale pressure profiles for various values of H/D for two engine operation. The peak values of the full-scale pressures are seen to be somewhat higher than the peak values of the small-scale pressures, especially at the higher values of H/D. Accordingly, from conservation of momentum considerations for the ground jet flow (which is essentially a boundary layer which merges into a free shear layer), the relative thickness of the small-scale ground jet is greater than that of the full-scale ground jet. The relatively thicker ground jet (and, hence, lower peak pressure) associated with the small-scale ground jet might be attributed to differences in ground plane relative roughness and other surface irregularities as well as to the non-linear growth of the boundary layer portion of the ground jet with Reynolds number, the latter effect leading to relatively thicker boundary layers in the small-scale ground jet.

It is of interest to note the rather curious trend of increasing dynamic pressure with increasing H/D indicated by both the full-scale and small-scale data of Figure 29.

Ground jet temperature profiles, presented in terms of ground jet temperature minus ambient temperature, are shown in Figure 30. The temperature profiles are seen to be relatively constant within the region measured (i.e., $h/D \lesssim 3$), with generally good agreement between the full-scale and small-scale data.

The thickness of the temperature profiles is seen to be considerably greater than the pressure profiles of Figure 29, being relatively constant over the region measured. The thicker thermal profile is attributed to the naturally rising gases from the edge of the velocity layer where buoyancy forces relative to inertial forces become important.

Single Engine Operation

Figure 31 shows the ground jet pressure and temperature profiles for single engine operation at H/D = 4. The agreement between the full-scale/small-scale profiles is quite good. The profiles for single jet operation are considerably thinner than the profiles for two jet operation, the thicker ground jet for two engine operation being the result of the flow in the interaction plane not being parallel to the ground.

Effect of Wind

Figure 32 shows ground jet pressure and temperature profiles for two engine operation at H/D = 4 and a wind speed of 16 MPH aligned with the pod. As for the low wind data of Figure 29, the full-scale pressure profile indicates higher peak pressure than the small-scale pressure profile, while good agreement is seen between the full-scale and small-scale temperature profiles. Both full-scale and small-scale data indicate little effect of the 16 MPH wind on the ground jet profiles relative to the low wind data of Figures 29 and 30.

Pod Pressure Distribution

Two Engine Operation - As indicated in Figure 28, the ground jets in the region between the engines flow toward one another, eventually interacting in the plane midway between the jet centerlines. Within the interaction process, the ground jet flows are turned outward and upward. The upward flow continues unimpeded until reaching the undersurface of the pod, where it impinges and is deflected around, and up, the sides of the pod.

It is noted that although ingestion was generally found to be significant in one engine or the other for two engine operation, but not in both, the upwash between the ground plane and the pod was found to be relatively symmetric, with upwash asymmetry occurring between the pod undersurface and the plane of the inlets.

The upwash of exhaust gases produces a pressure field on the vehicle undersurface which can, in general, result in significant force levels when considering the total surface area affected. Characteristic of the pressure distribution for two engine operation is a positive pressure field approximately midway between the engines, with a negative pressure field on either side, the level of the pressure field being strongly dependent on H/D. The positive pressure field results from impingement of the upwash flow, or fountain, on the engine pod at velocities as high as about 200 fps at the lower values of H/D. The negative pressure field on either side of the positive pressure field results from high mass flow entrainment by the jets (and, to a lesser extent, entrainment by the upwash flow), coupled with limited area from which to draw the free air necessary to satisfy the scavenging characteristics of the jets (Figure 28).

Pressure distributions on the undersurface of the full-scale/small-scale pods are shown in Figure 33 at various values of H/D. The strong effect of H/D on the impingement strength of the upwash is clearly indicated. Excellent agreement between the full-scale and small-scale test results is evident, both in peak pressure levels and in the details of the pressure distributions.

Single Engine Operation - For single engine operation, the induced pressures on the pod undersurface result solely from induced circulation set up by entrainment of free air by the jet, the resulting induced pressure distribution being considerably less than for two engine operation, and decreasing with distance from the operating engine. Figure 34 compares the full-scale and small-scale pressure distributions at H/D = 4. Excellent agreement between the full-scale and small-scale data is evident. More comprehensive comparisons, showing excellent agreement between full-scale and small-scale single jet induced pressure data, are reported in Reference 13.

Effect of Wind

Figure 35 compares full-scale and small-scale pressure distributions for two engine operation at H/D = 4 and a wind speed of 16 MPH aligned with the pod. The full-scale and small-scale data are in excellent agreement, both indicating significant reduction in the pod pressure levels from the low wind data of Figure 33.

Upwash Temperature

Temperatures of the upwash between the engines of the full-scale and small-scale pods were measured with thermocouples cantilevered from the sides of the pods near the plane of the inlets as indicated in Figure 9. Good agreement in the qualitative nature and quantitative levels of the full-scale and small-scale upwash was found to exist. Specifically, the upwash environment of both the full-scale and small-scale tests was found to exhibit temperature fluctuation characteristics much like that of the inlets. Typical local temperature fluctuations in the range of 50° - 100°F were observed with peak fluctuations up to 150°F.

Full-scale/small-scale similarity was also observed in the relative level of thermal activity in the proximity of the ingestion prone engine compared to that in the proximity of the non-ingestion prone engine, that near the ingestion prone engine being significantly greater. Analysis of both the full-scale and small-scale data suggests an upwash model composed predominately of large clumps of hot gas (as evidenced by the simultaneous response of several inlet proximity thermocouples). In approaching the inlet, acceleration of the flow results in stretching of the clumps, or bubbles, into elongated stream tubes which may occupy anywhere from a very small fraction of the inlet cross section to the major portion of the inlet cross section.

CONCLUSIONS

Results of detailed comparisons of recirculation effects of a full-scale and geometrically similar small-scale VTOL lift engine pod, operating at the same exhaust pressure/temperature conditions, have indicated that the overall near flow field, external thermal environment, and hot gas ingestion are scalable, in terms of both dynamic and time-average characteristics. Some specific similarities of the full-scale and small-scale test results are given below:

1. For both the full-scale and small-scale tests, significant ingestion of hot gases was found to occur in one engine or the other during two engine operation, but not in both simultaneously. For single engine operation, both full-scale and small-scale tests showed low level ingestion.

2. For two engine operation, ingestion characteristics of both full-scale and small-scale tests were found to be highly sporadic, exhibiting closely spaced temperature spikes which typically persist for a small fraction of a second.

3. Frequency analysis showed that the full-scale/small-scale inlet temperature fluctuations are dynamically similar when compared on a time-scaled basis. Specifically, power density spectra of the full-scale and small-scale temperature fluctuations were found to be in excellent agreement when compared in terms of the non-dimensional frequency, fD/U_o (i.e., Strouhal number).

4. Comparisons of full-scale/small-scale hot gas ingestion indices of inlet temperature levels, temperature distortion, and temperature gradients showed good full-scale/small-scale agreement in the instantaneous characteristics of the various indices, in the amplitude distribution (i.e., probability density) of the indices, and in the effect of H/D on the time-average values of the indices.

5. Comparisons of the lateral spreading and axial decay characteristics of the free jets, of the pressure and temperature profiles within the ground jet, and of the upwash strength and thermal environment showed that the overall near flow field and thermal environment are scalable.

REFERENCES

1. Lavi, R., "Parametric Investigations of VTOL Ground Proximity Effects." AIAA Paper Number 67-44, July 1967.

2. Hammond, A.D., McLemore, H.C., "Hot-Gas Ingestion and Jet Interference Effects for Jet V/STOL Aircraft." Presented at AGARD Flight Mechanics Panel Meeting, Gottingen, West Germany, September 1967.

3. McLemore, H.C., Smith, C.C., Jr., "Hot-Gas Ingestion Investigation of Large-Scale Jet VTOL Fighter-Type Models." NASA TND-4609, June 1968.

4. Lavi, R., Hall, G.R., Stark, W.W., "Full-Scale Ground Proximity Investigation of a VTOL Fighter Model Aircraft." NASA CR-1098, June 1968.

5. Hall, G.R., "Recirculation and Ingestion Characteristics of a Large-Scale VTOL Lift Engine Pod." NASA CR-72410, August 1968.

6. Kirk, J.A., Barrack, J.P., "Reingestion Characteristics and Inlet Flow Distortion of V/STOL Lift Engine Fighter Configurations." AIAA Journal of Aircraft, March-April 1969.

7. Ryan, P. F., Cosgrove, W. J., "Empirically Determined Wind and Scale Effects on Hot Gas Recirculation Characteristics of Jet V/STOL Aircraft." NASA CR-1445, Oct. 1969.

8. Adarkar, D.B., Hall, G.R., "The Fountain Effect and VTOL Exhaust Ingestion." AIAA Journal of Aircraft, March-April 1969.

9. Hall, G.R., Rogers, K.H., "Recirculation Effects Produced by a Pair of Heated Jets Impinging on a Ground Plane." NASA CR-1307, May 1969.

10. Watson, W.W., Weddell, A., Murakoshi, A., "Real Time, Real Temperature Jet V/STOL Test Facility." AIAA Paper No. 69-310, March 1969.

11. Hall, G.R., Bogdanovic, J.A., "Response of Bare Wire Thermocouples to Temperature Variations in a Jet Engine Intake." AIAA Journal of Aircraft, July-August 1967.

12. Bendat, J.S., Pierson, A.G., Measurement and Analysis of Random Data. New York; John Wiley & Sons, 1968.

13. Hall, G.R., "Scaling of VTOL Suckdown Forces." AIAA Journal of Aircraft, July-August 1967.

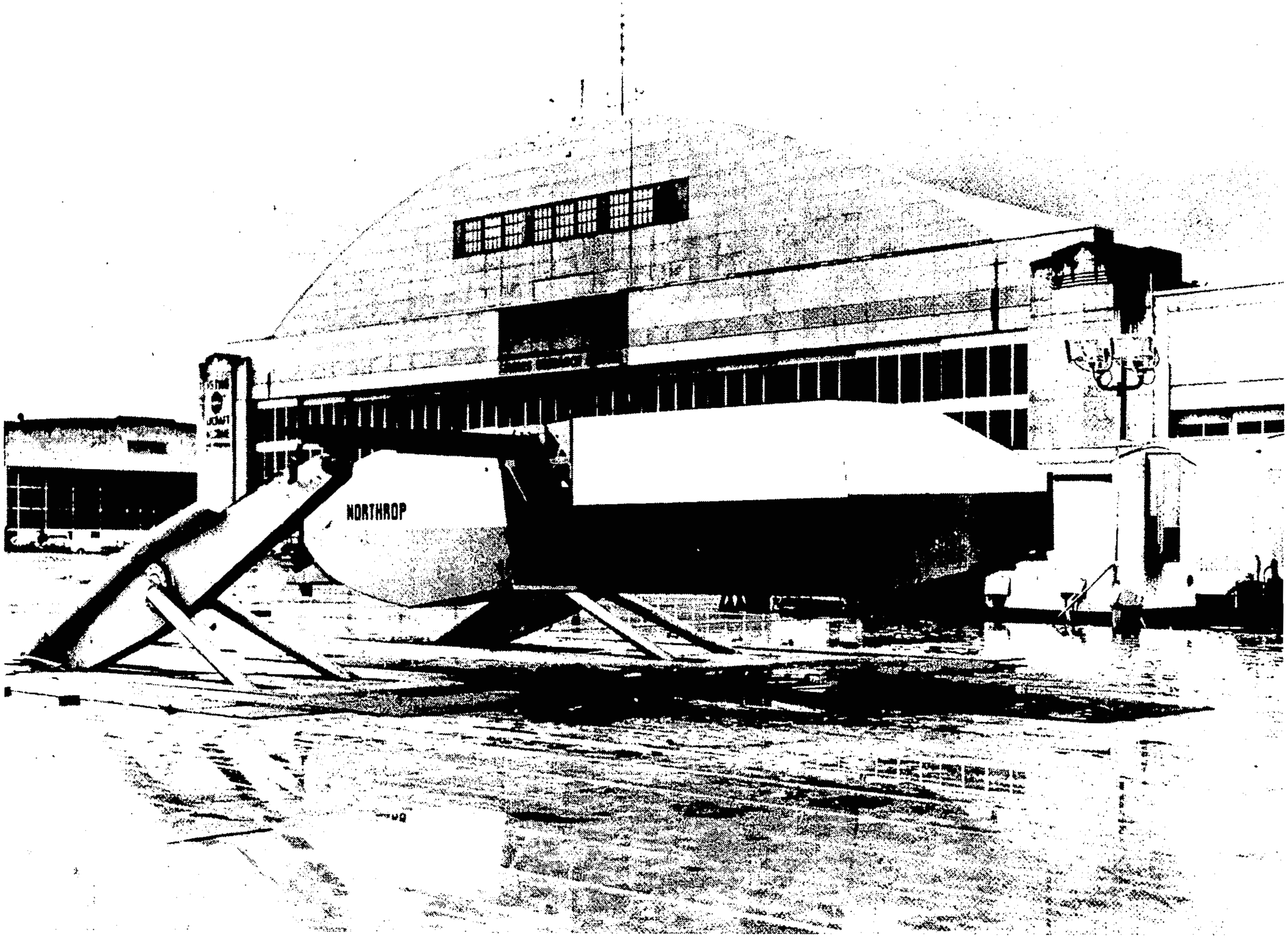

FIGURE 1. NASA-AMES VTOL GROUND EFFECTS TEST FACILITY

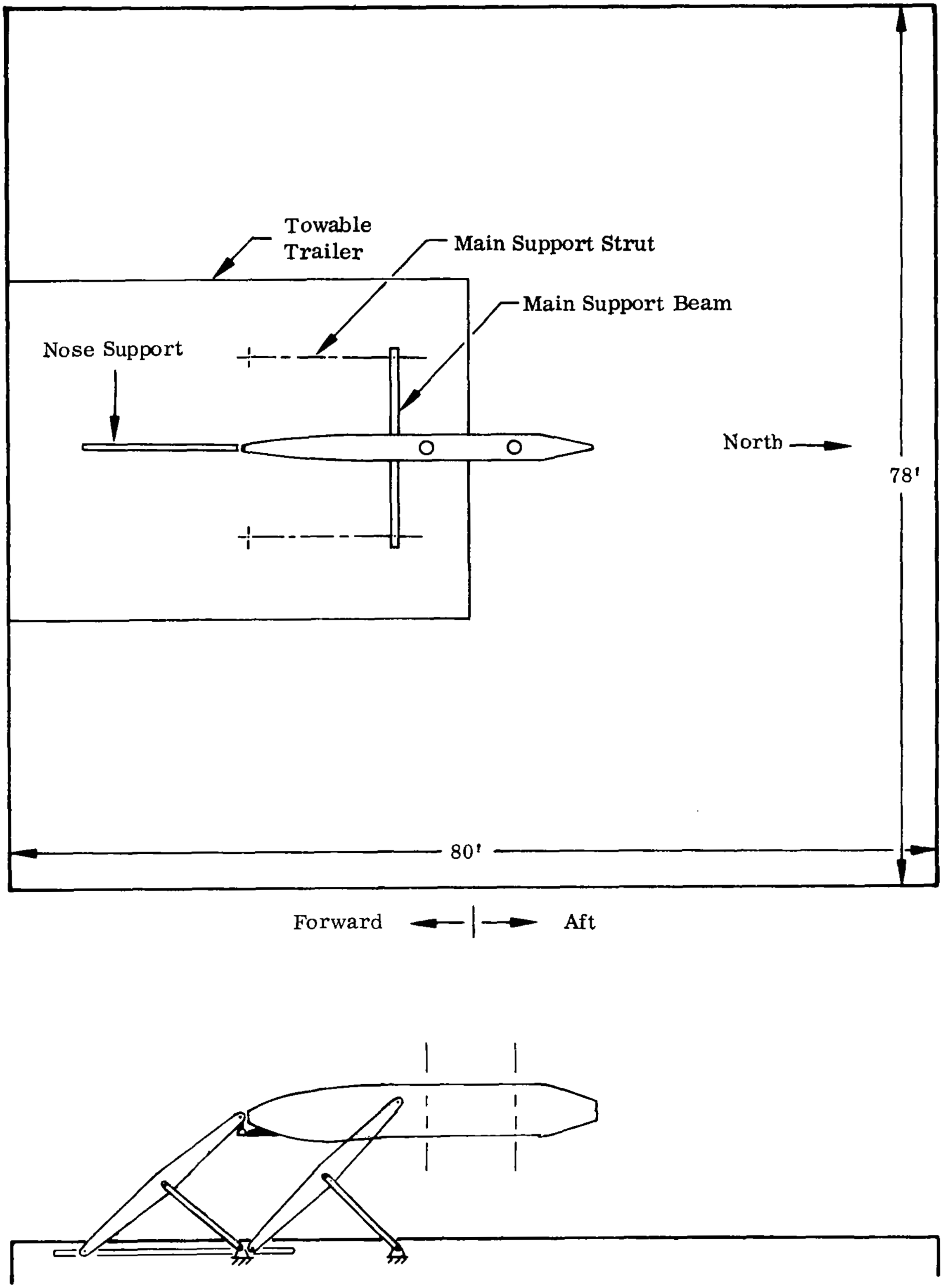

FIGURE 2. FULL-SCALE ENGINE POD SUPPORT AND GROUND PLANE

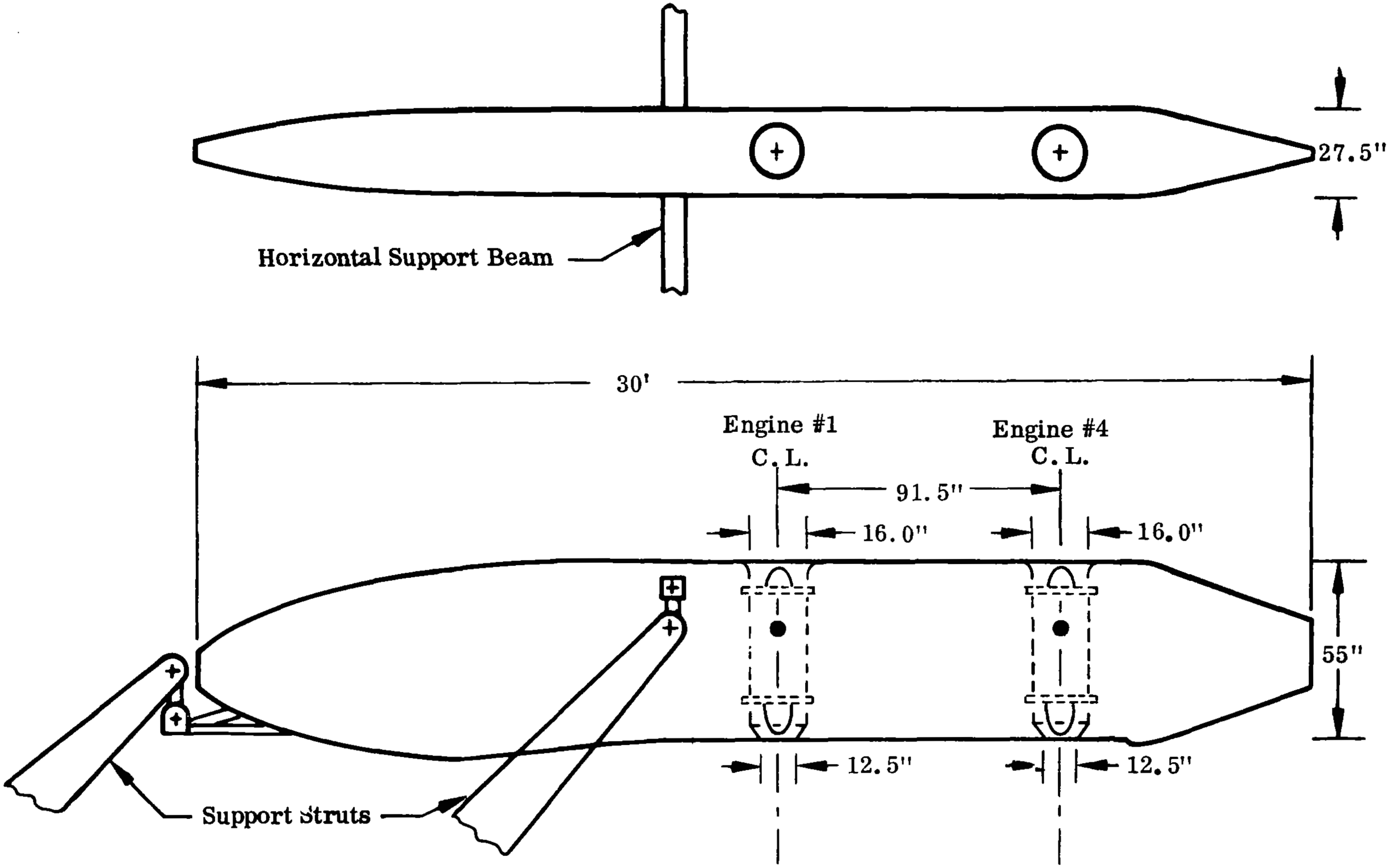

FIGURE 3. FULL-SCALE ENGINE POD

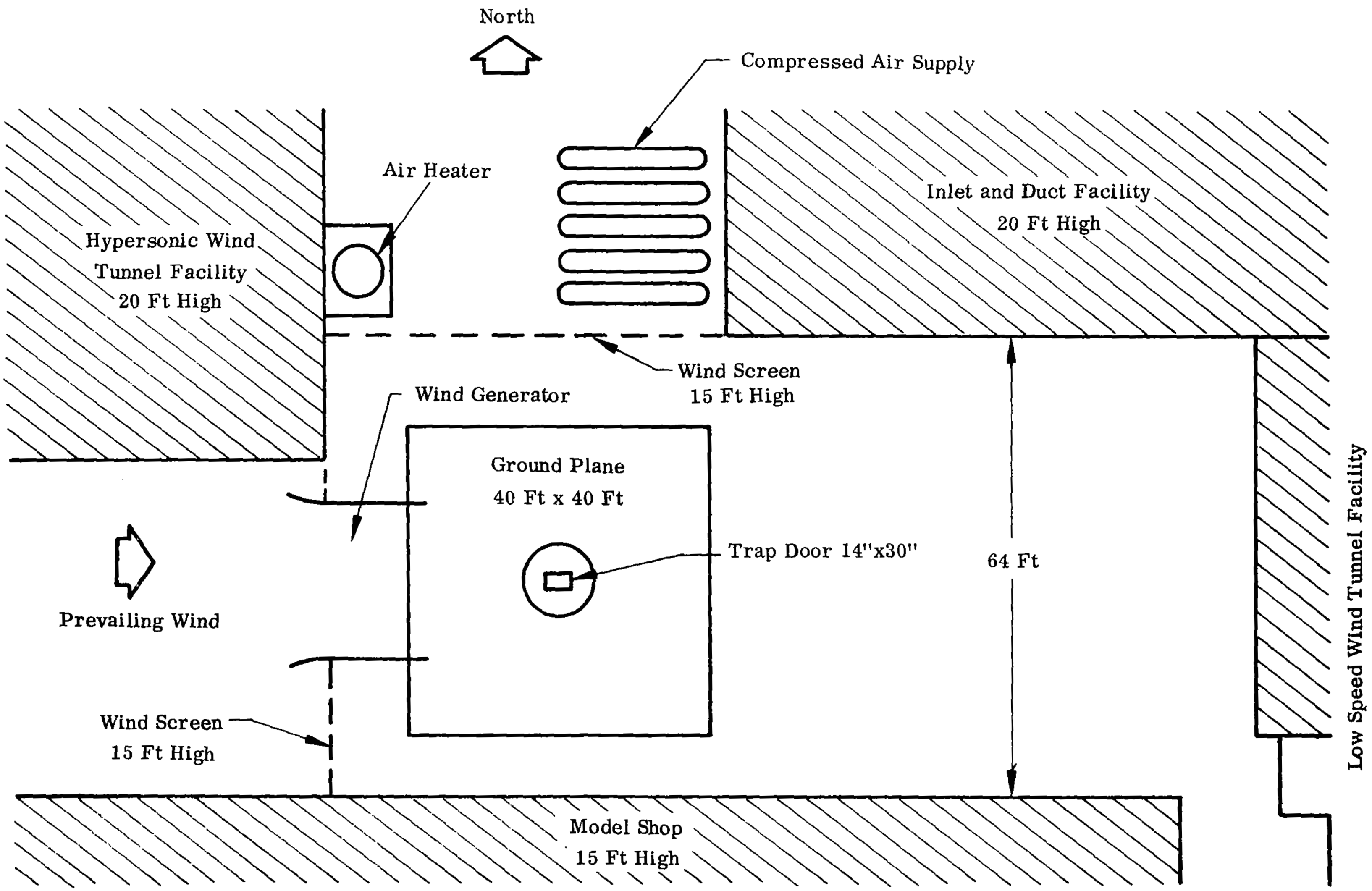

FIGURE 4. NORTHROP V/STOL GROUND EFFECTS TEST FACILITY GENERAL LAYOUT

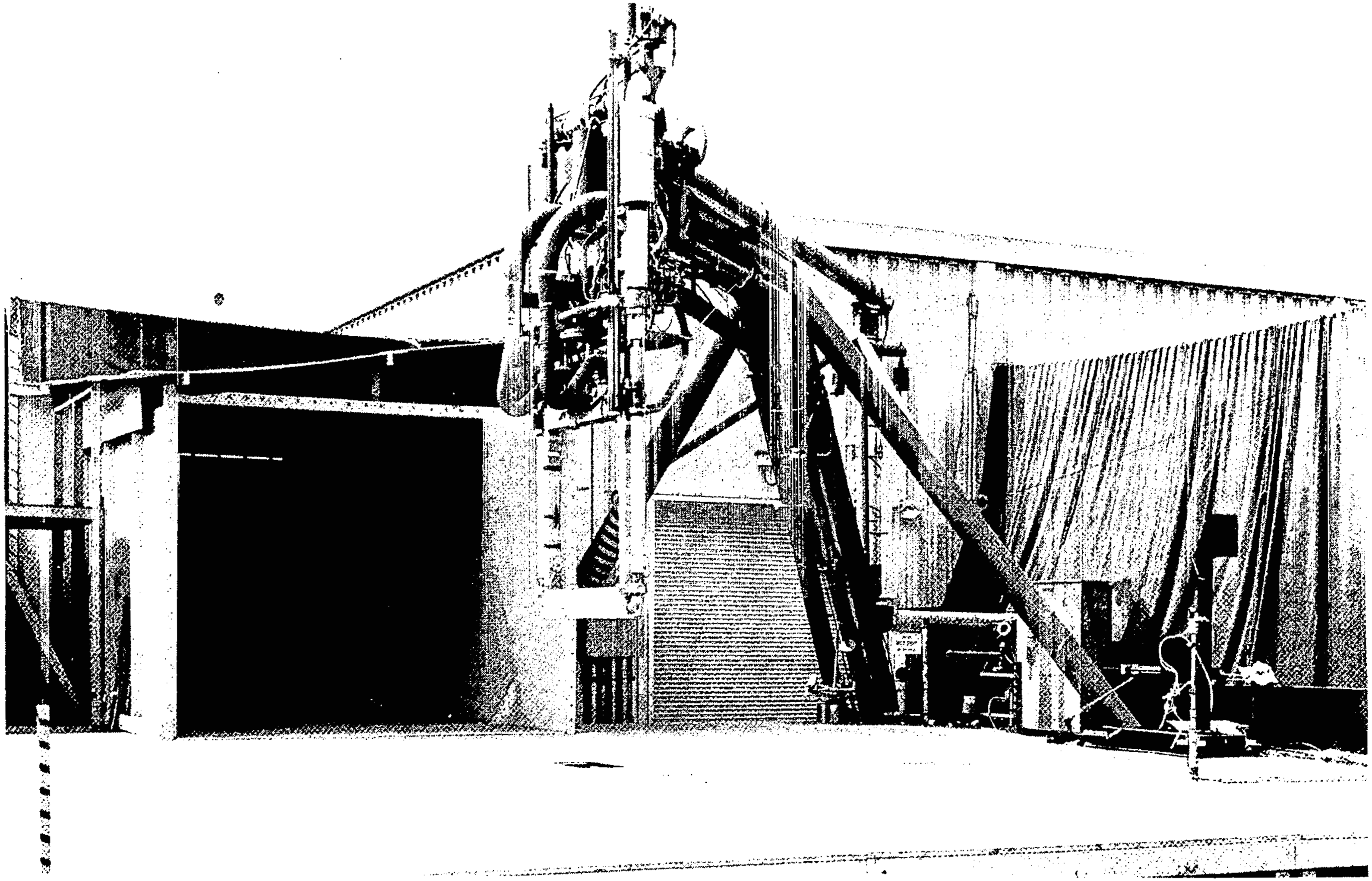

FIGURE 5. NORTHROP V/STOL GROUND EFFECTS TEST FACILITY

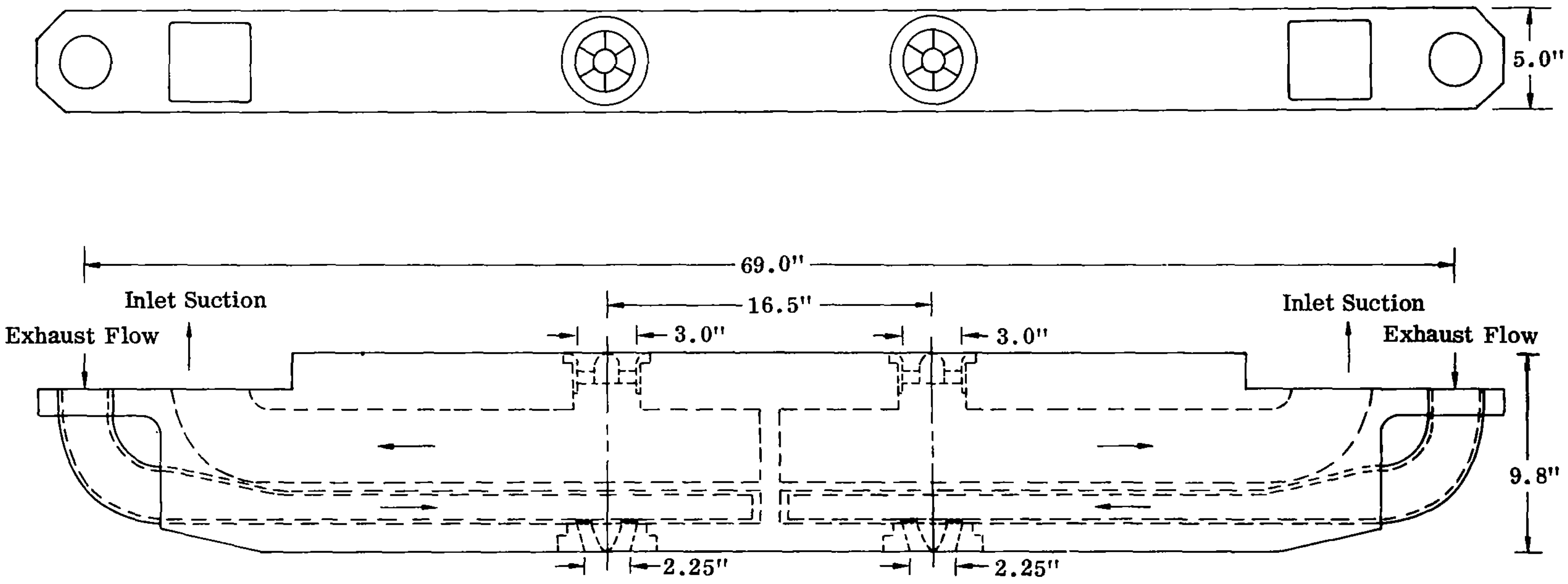

FIGURE 6. SMALL-SCALE ENGINE POD

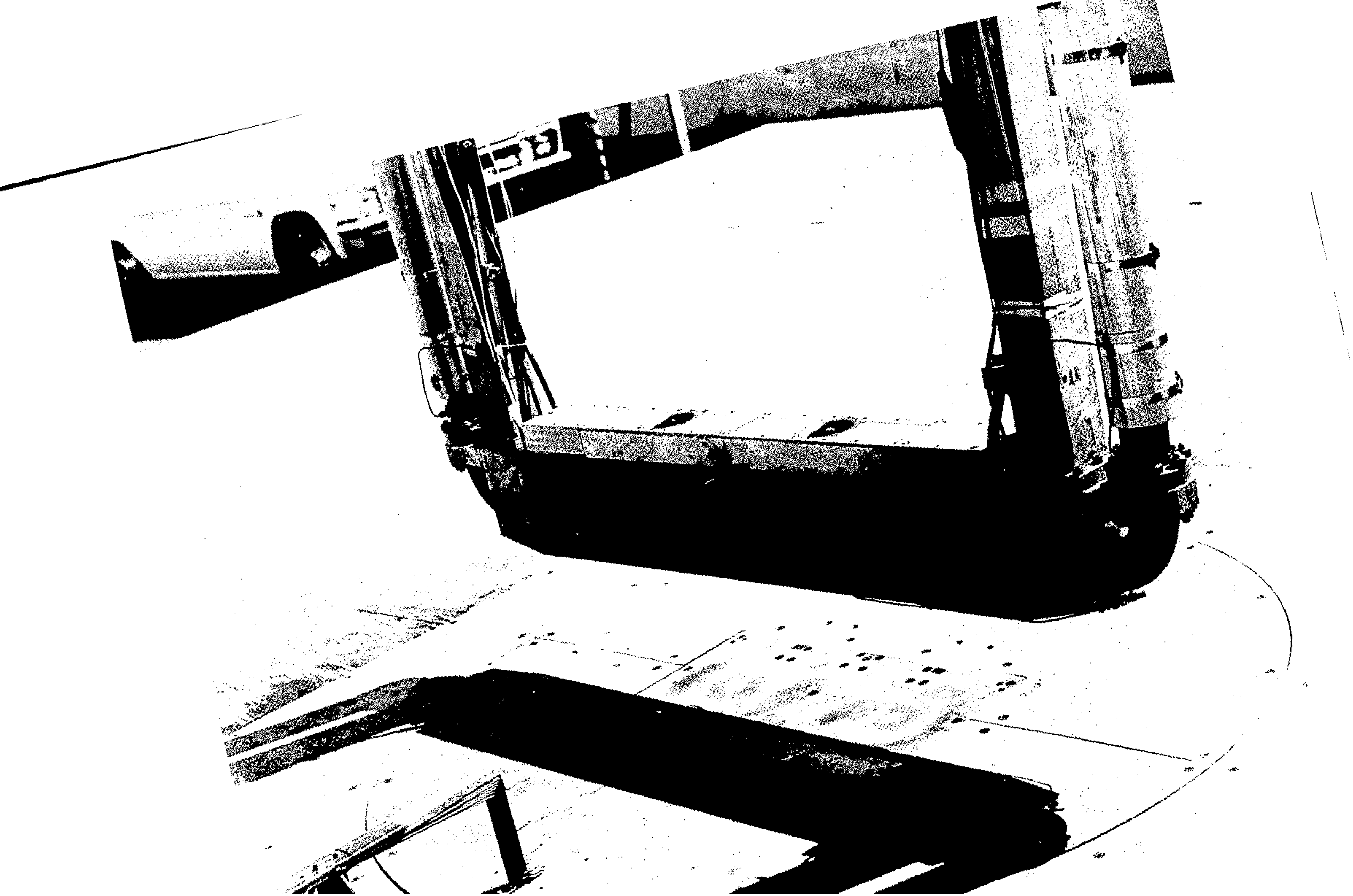

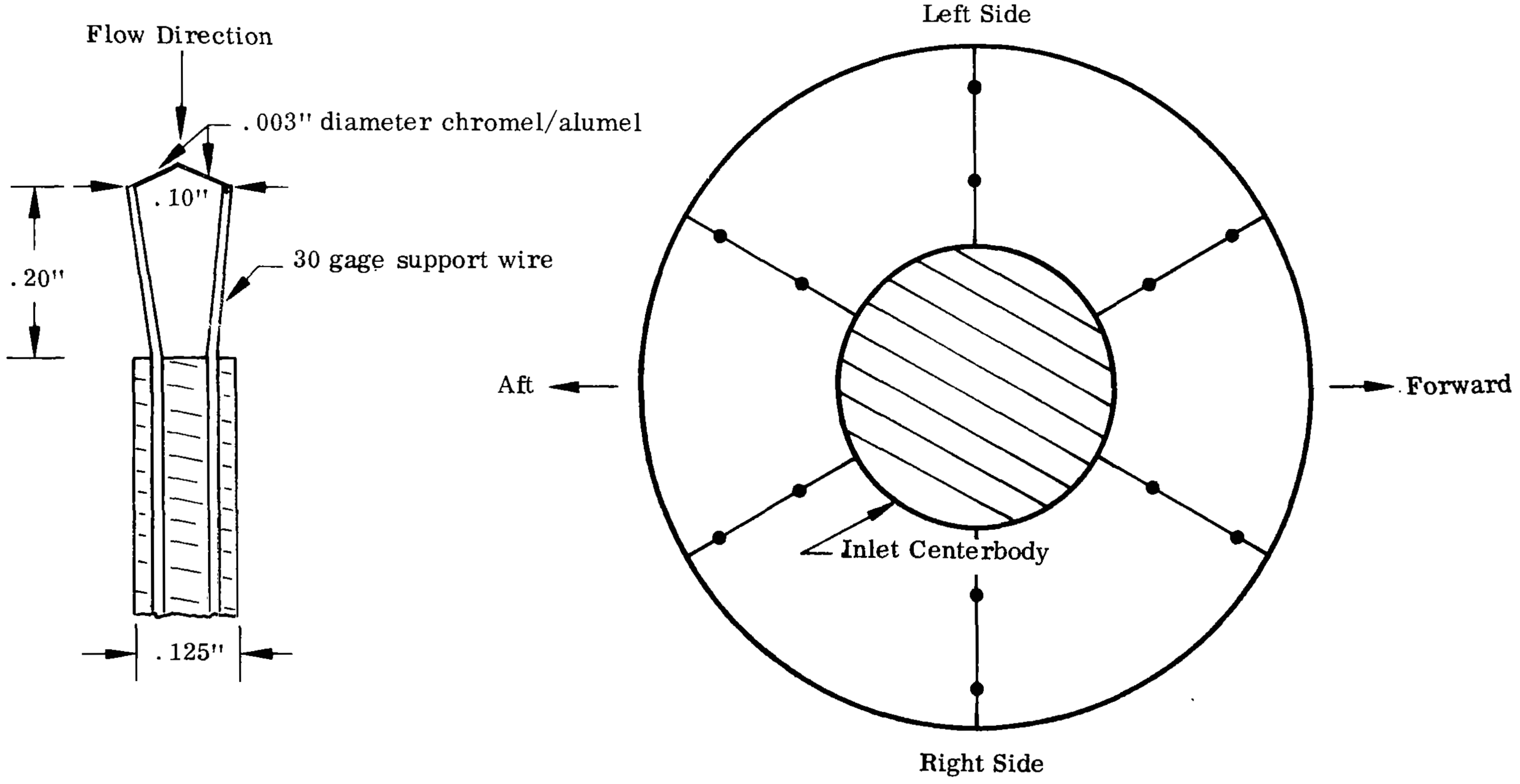

Note: T-C's located to represent equal flow areas.

FIGURE 8. INLET THERMOCOUPLE LOCATION AND CONSTRUCTION DETAIL

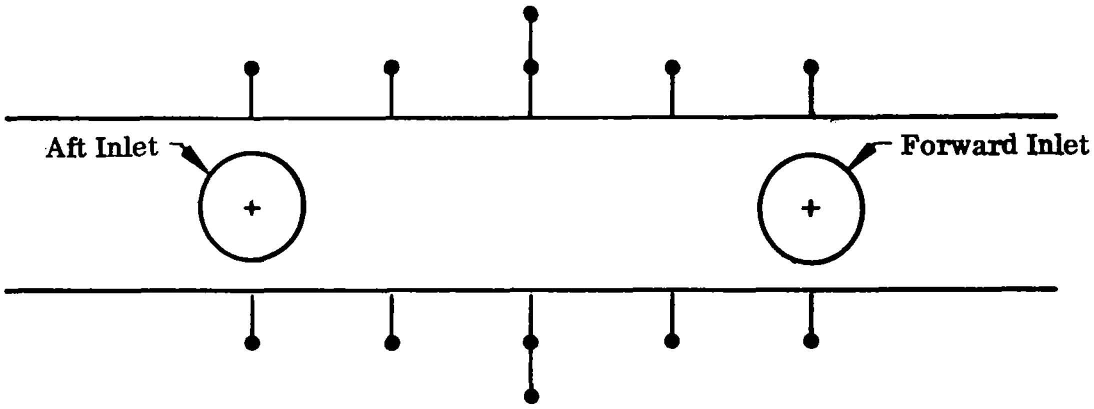

Note: T-C's located near plane of pod upper surface

FIGURE 9. INLET PROXIMITY THERMOCOUPLES

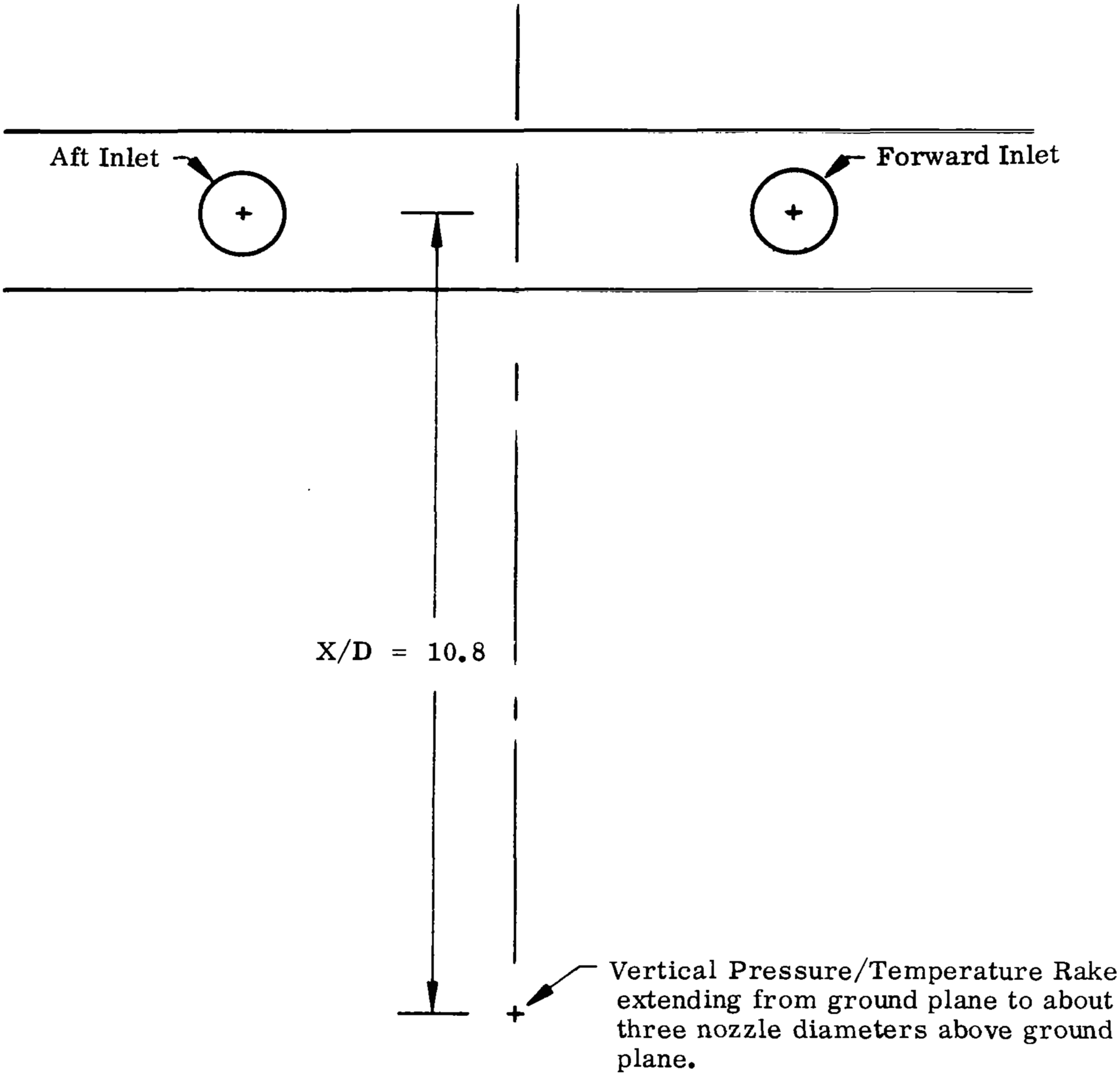

FIGURE 10. GROUND JET VERTICAL RAKE LOCATION

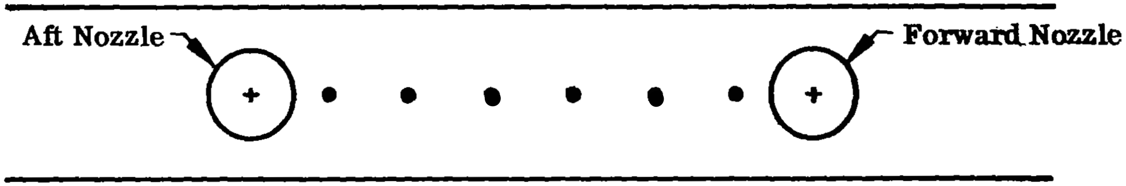

Note: Pressure taps located on engine pod lower surface

FIGURE 11. ENGINE POD PRESSURES

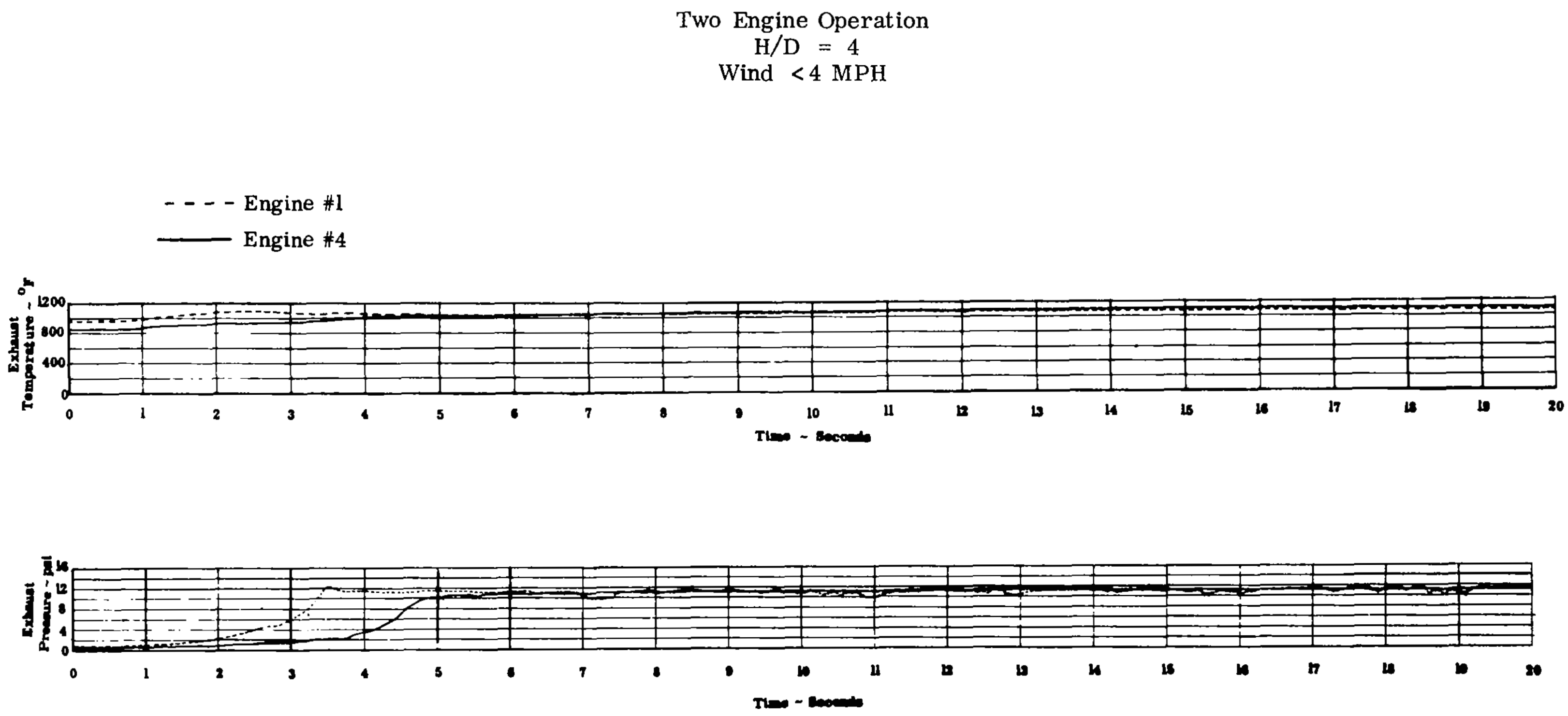

Two Engine Operation
H/D = 4
Wind <4 MPH

FIGURE 12. TYPICAL FULL-SCALE EXHAUST PRESSURE AND TEMPERATURE HISTORY

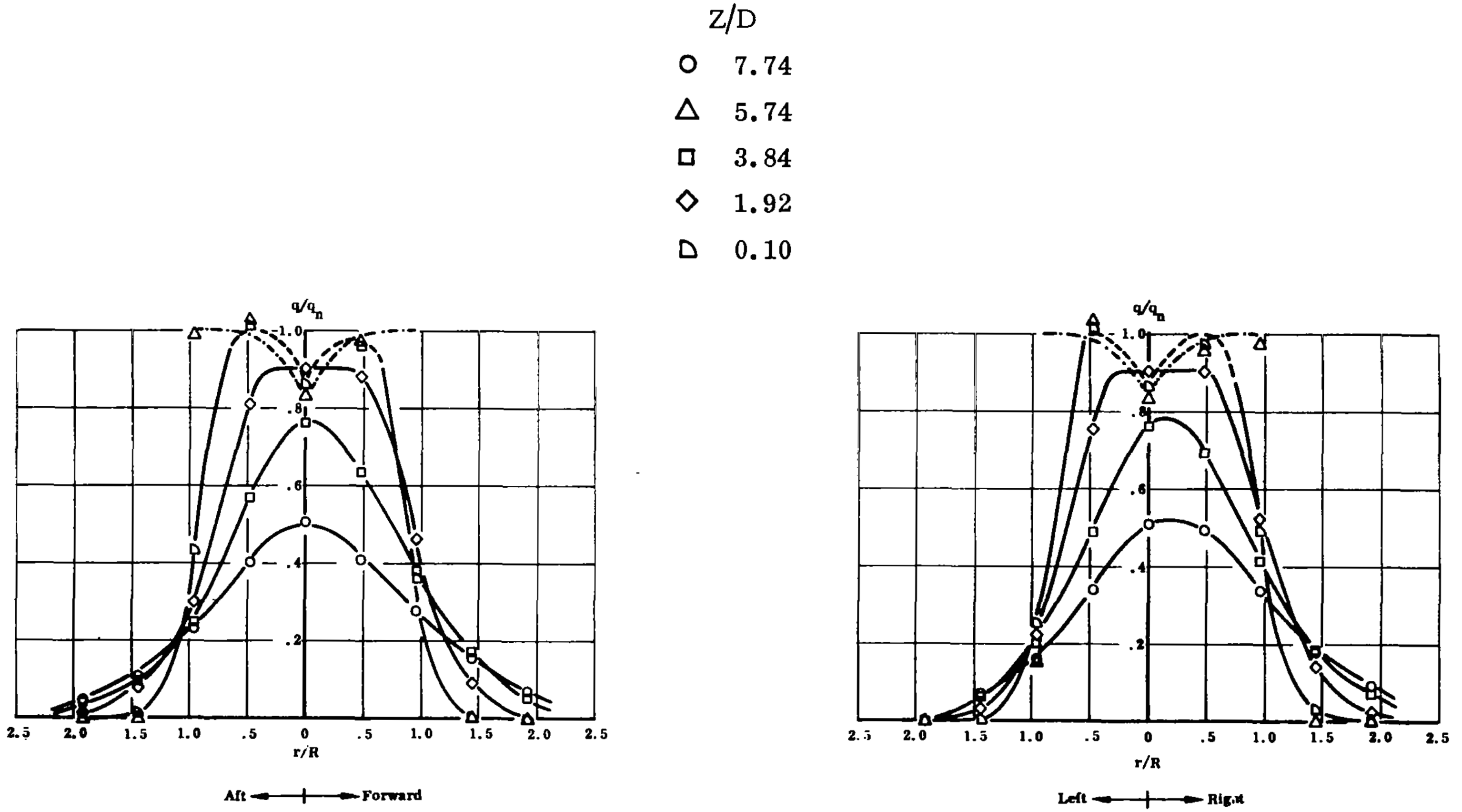

(a) ENGINE #1

FIGURE 13. FULL-SCALE EXHAUST JET CALIBRATION

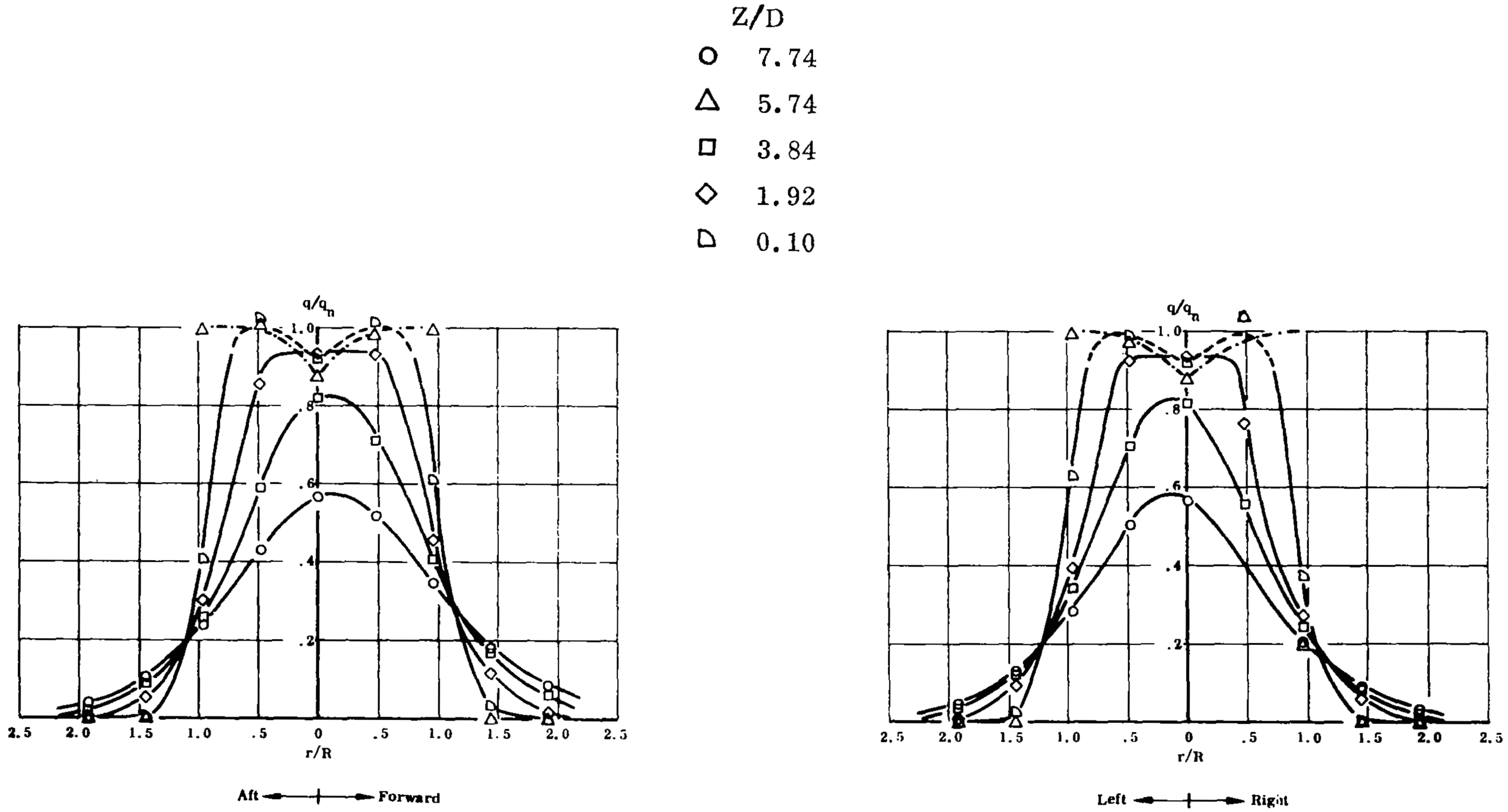

(b) ENGINE #4

FIGURE 13 (cont'd). FULL-SCALE EXHAUST JET CALIBRATION

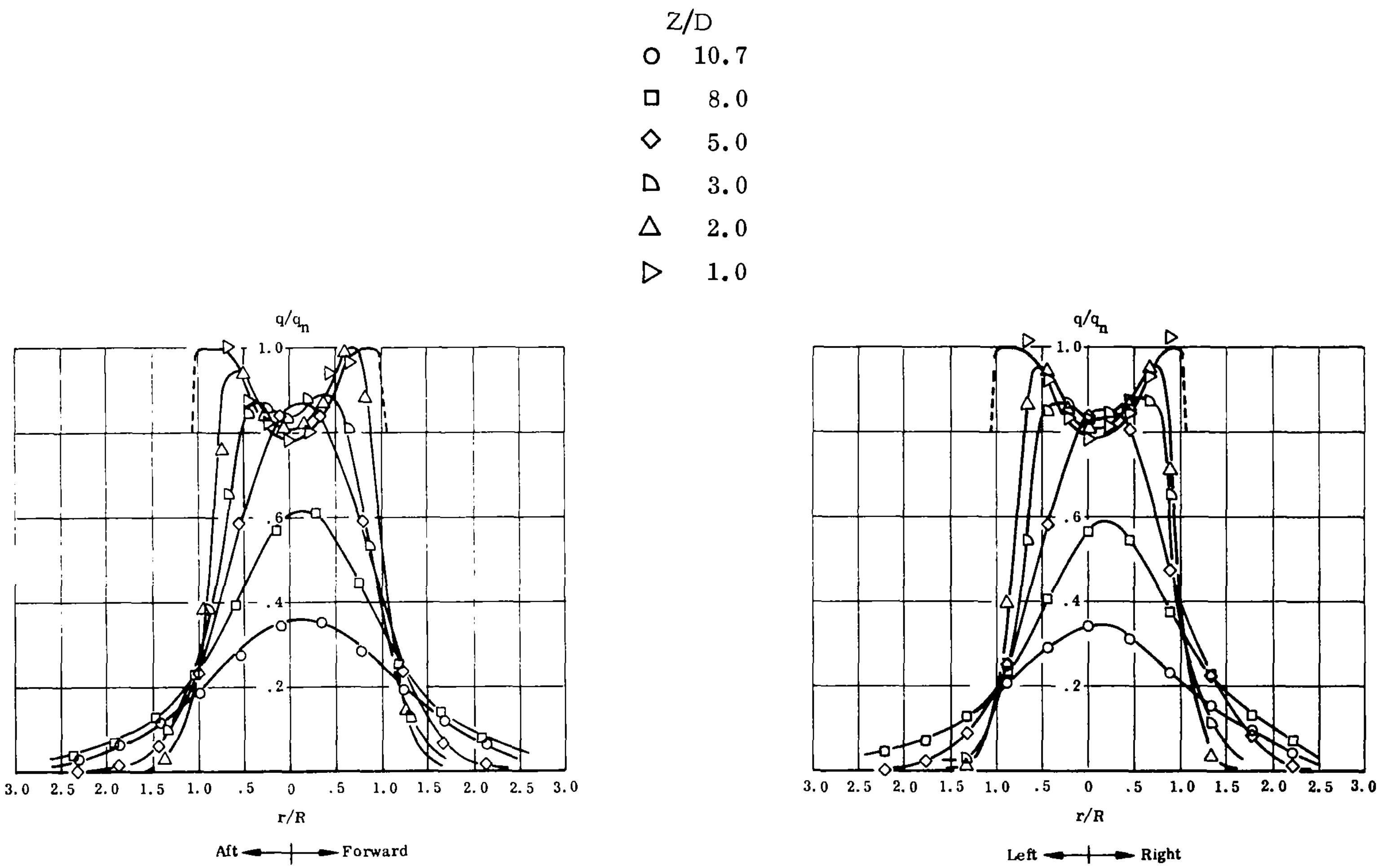

(a) FORWARD NOZZLE

FIGURE 14. SMALL-SCALE EXHAUST JET CALIBRATION

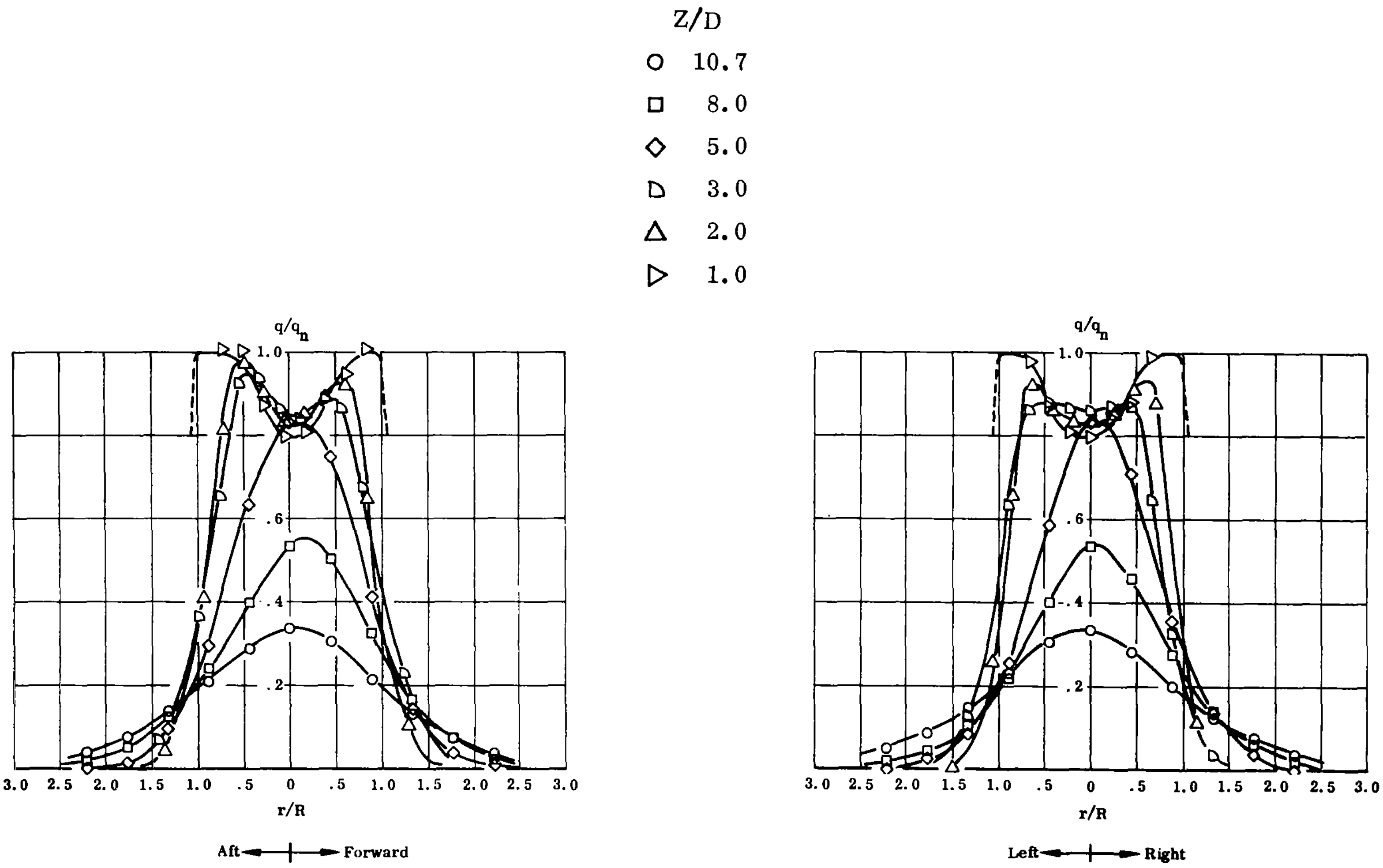

(b) AFT NOZZLE

FIGURE 14 (cont'd). SMALL-SCALE EXHAUST JET CALIBRATION

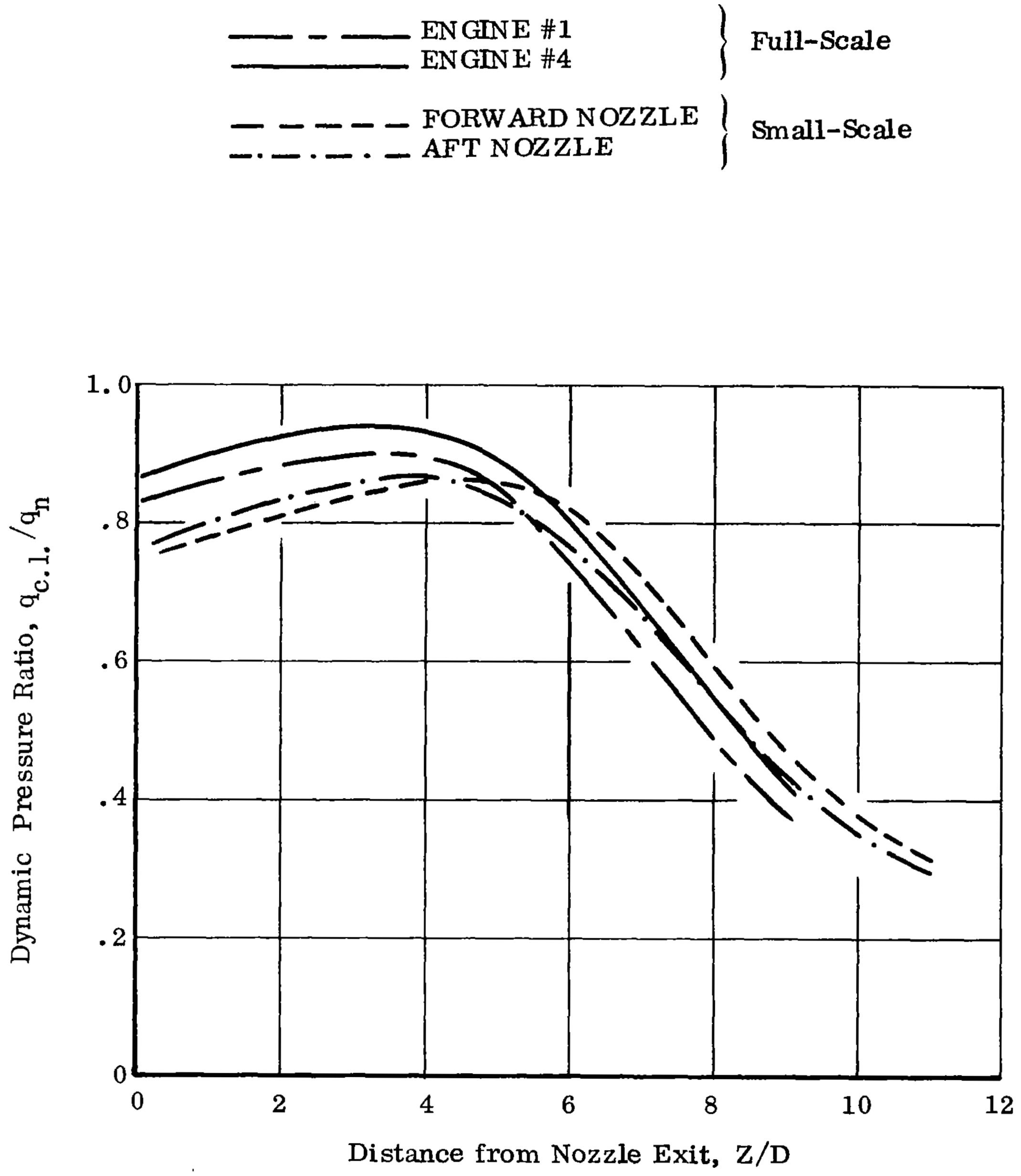

FIGURE 15. EXHAUST JET CENTERLINE DYNAMIC PRESSURE DECAY

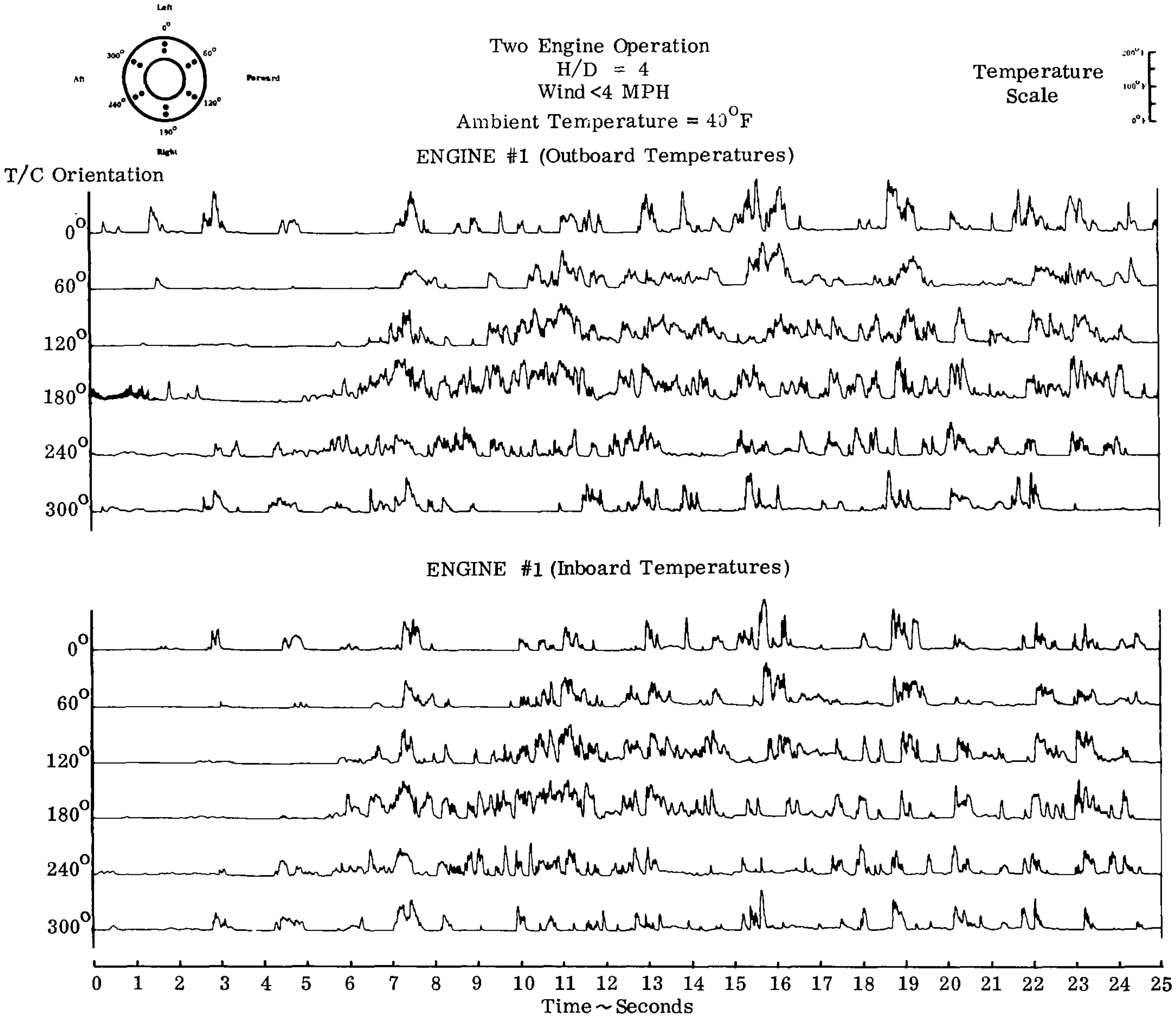

FIGURE 16a. FULL-SCALE INLET TEMPERATURE HISTORY - INGESTION PRONE ENGINE

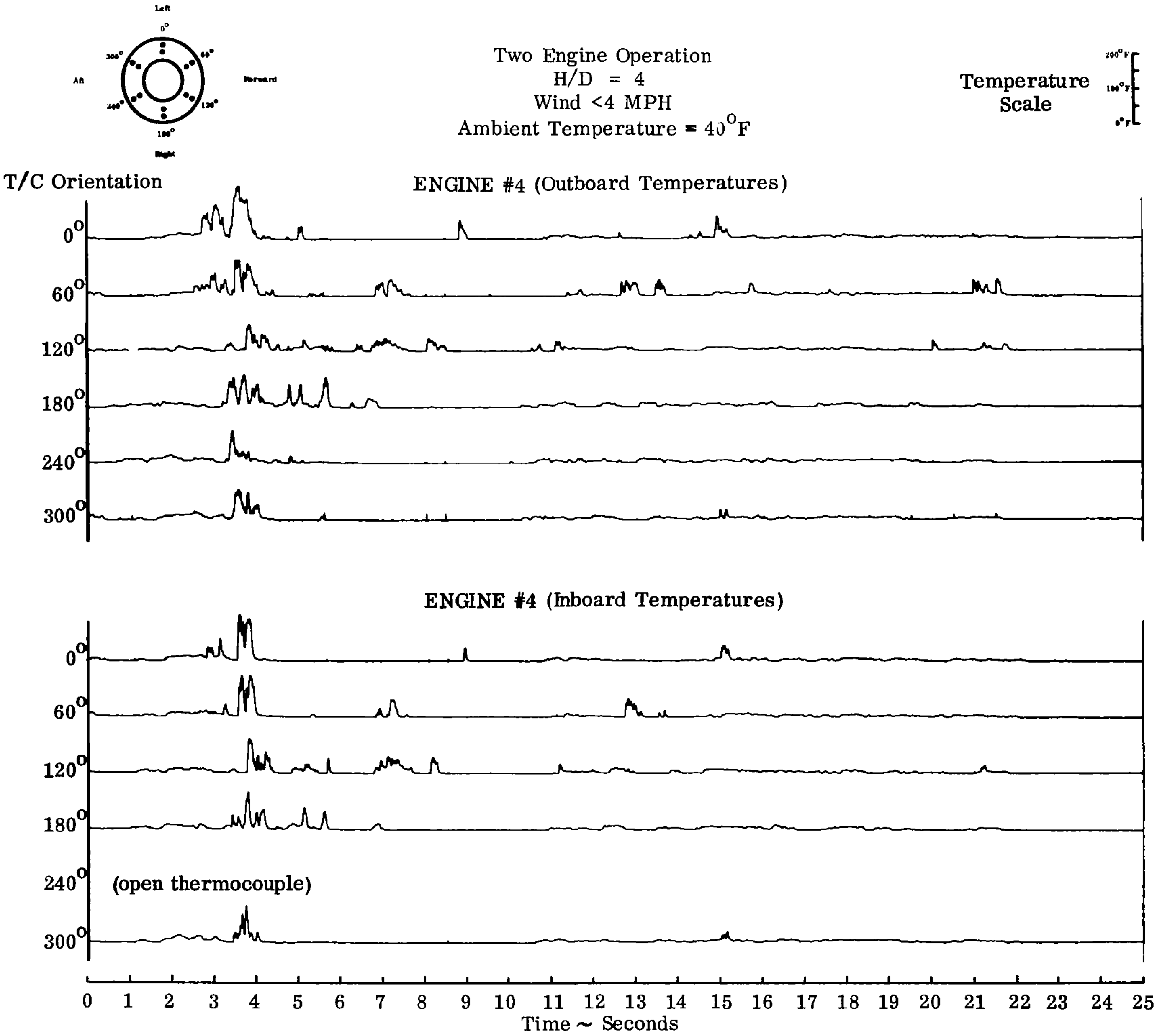
Two Engine Operation
H/D = 4
Wind <4 MPH
Ambient Temperature = 40°F

FIGURE 16b. FULL-SCALE INLET TEMPERATURE HISTORY - NON-INGESTION PRONE ENGINE

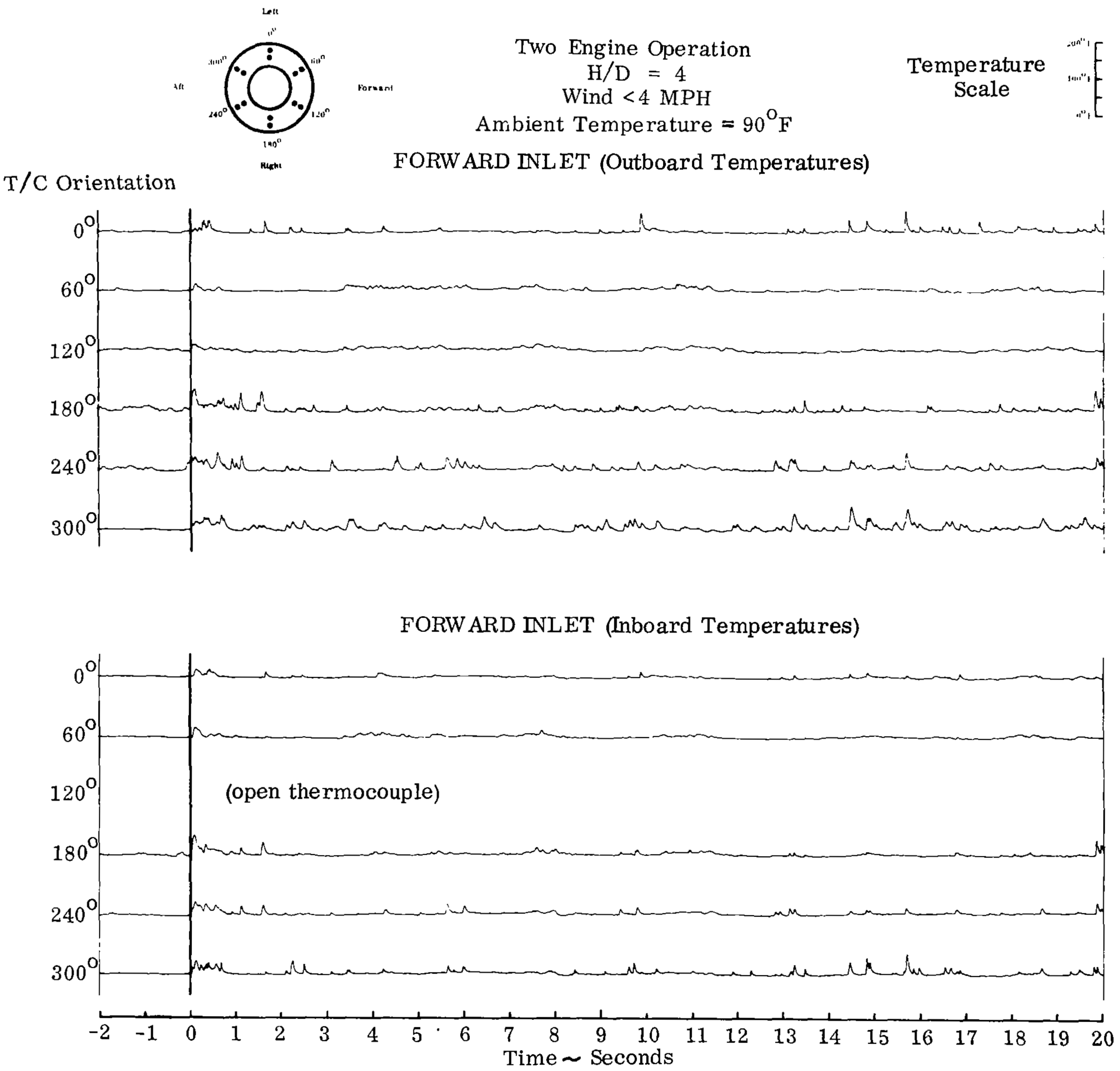

FIGURE 17a. SMALL-SCALE INLET TEMPERATURE HISTORY - NON-INGESTION PRONE ENGINE

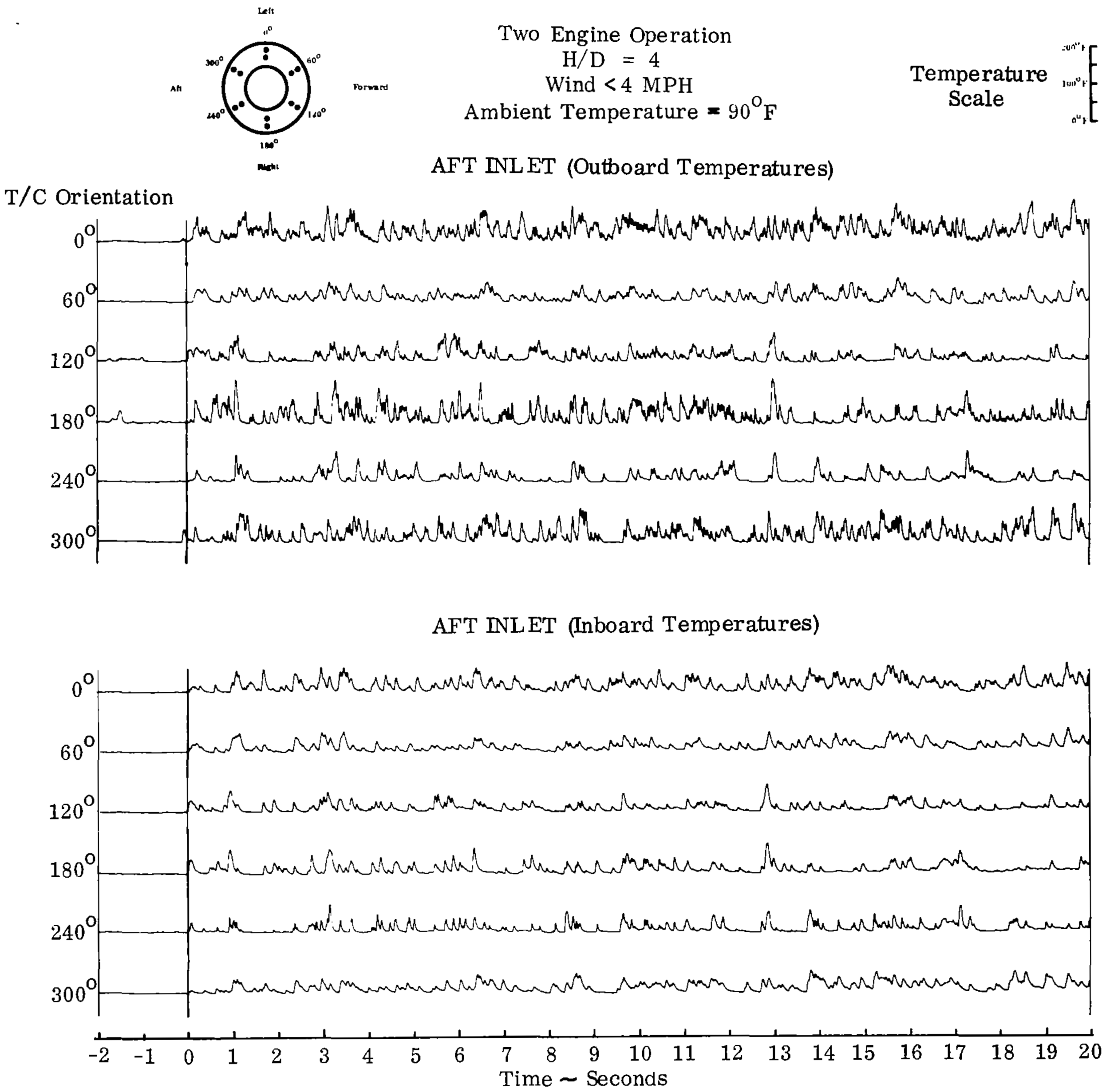

FIGURE 17b. SMALL-SCALE INLET TEMPERATURE HISTORY - INGESTION PRONE ENGINE

Two Engine Operation
H/D = 4
Wind <4 MPH

ENGINE #1

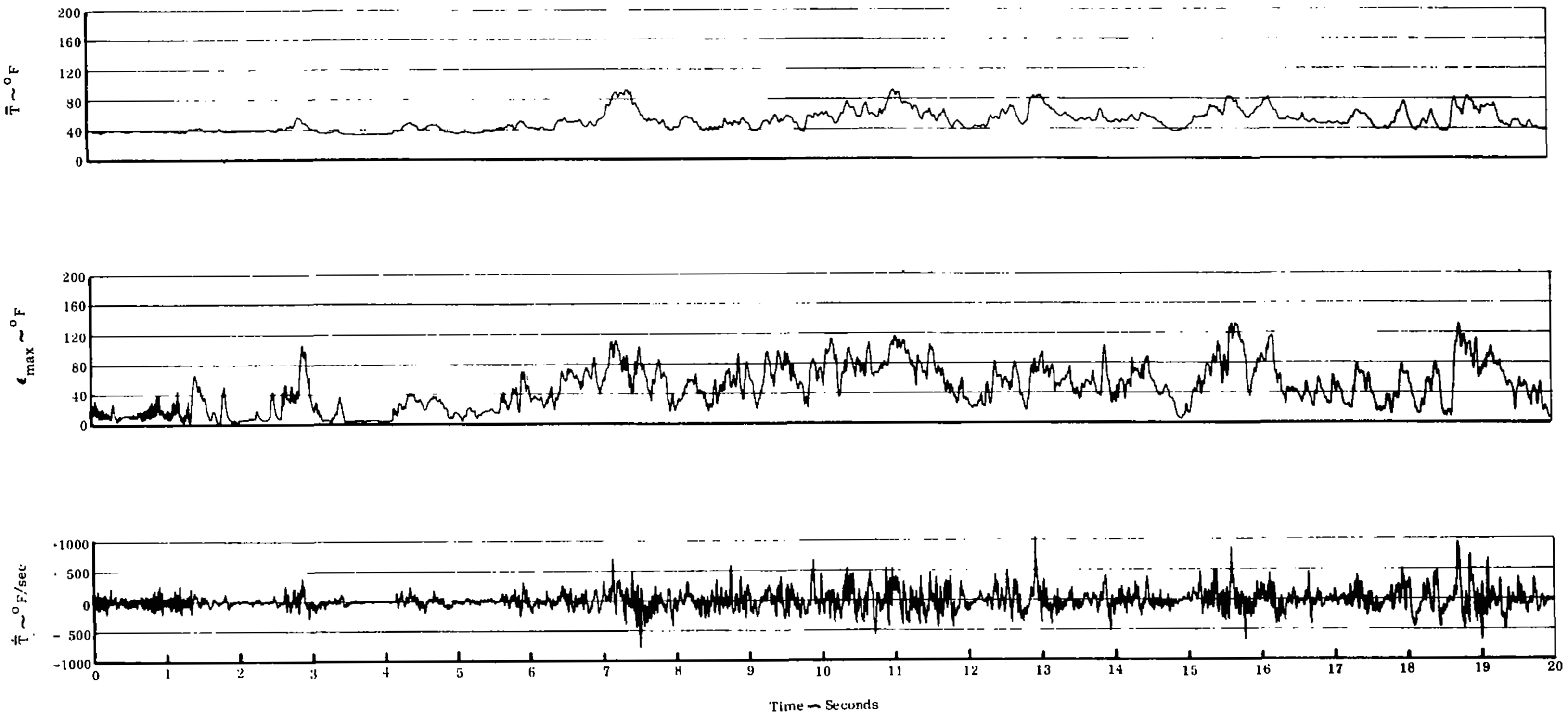

FIGURE 18. FULL-SCALE INGESTION CHARACTERISTICS HISTORY

Two Engine Operation
H/D = 4
Wind < 4 MPH

AFT INLET

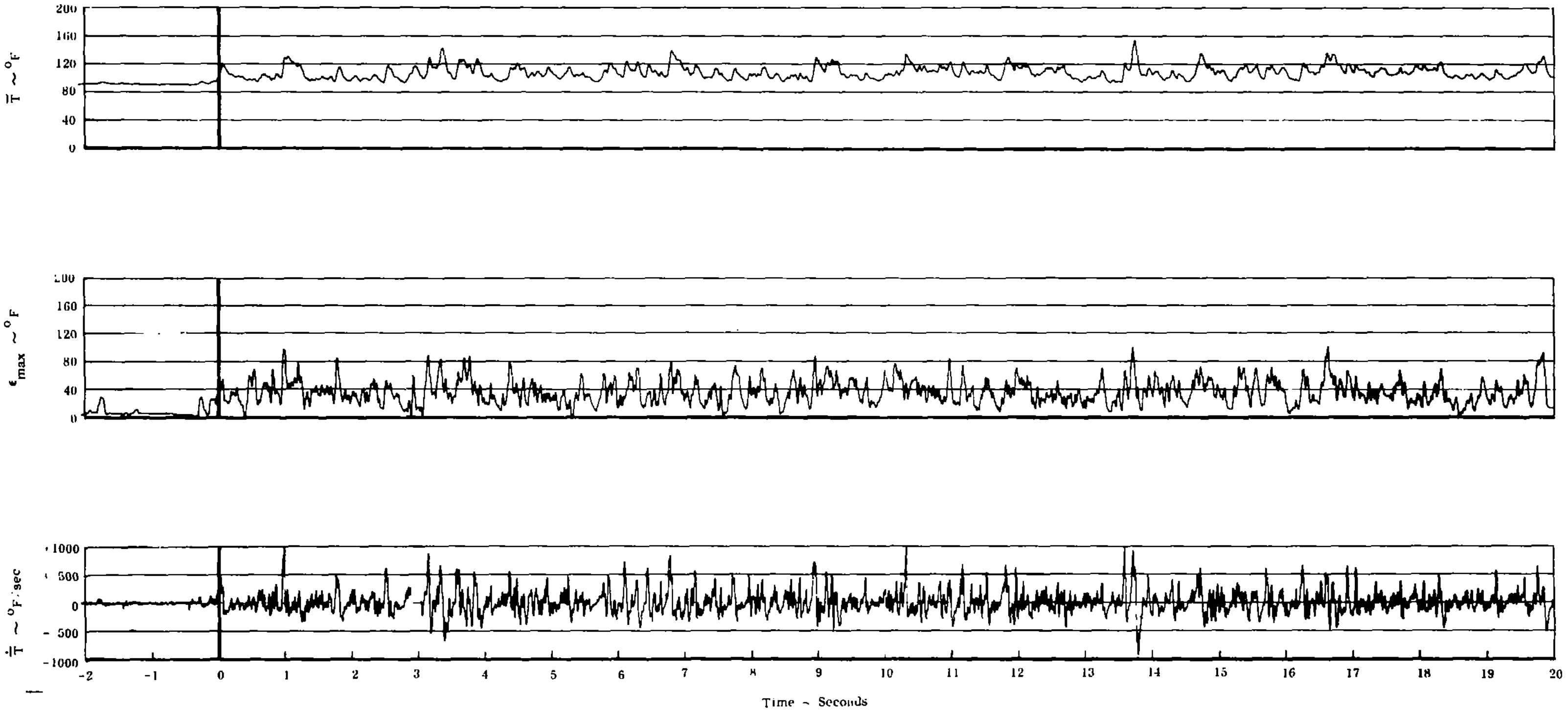

FIGURE 19. SMALL-SCALE INGESTION CHARACTERISTICS HISTORY

Two Engine Operation
H/D = 4
Wind <4 MPH

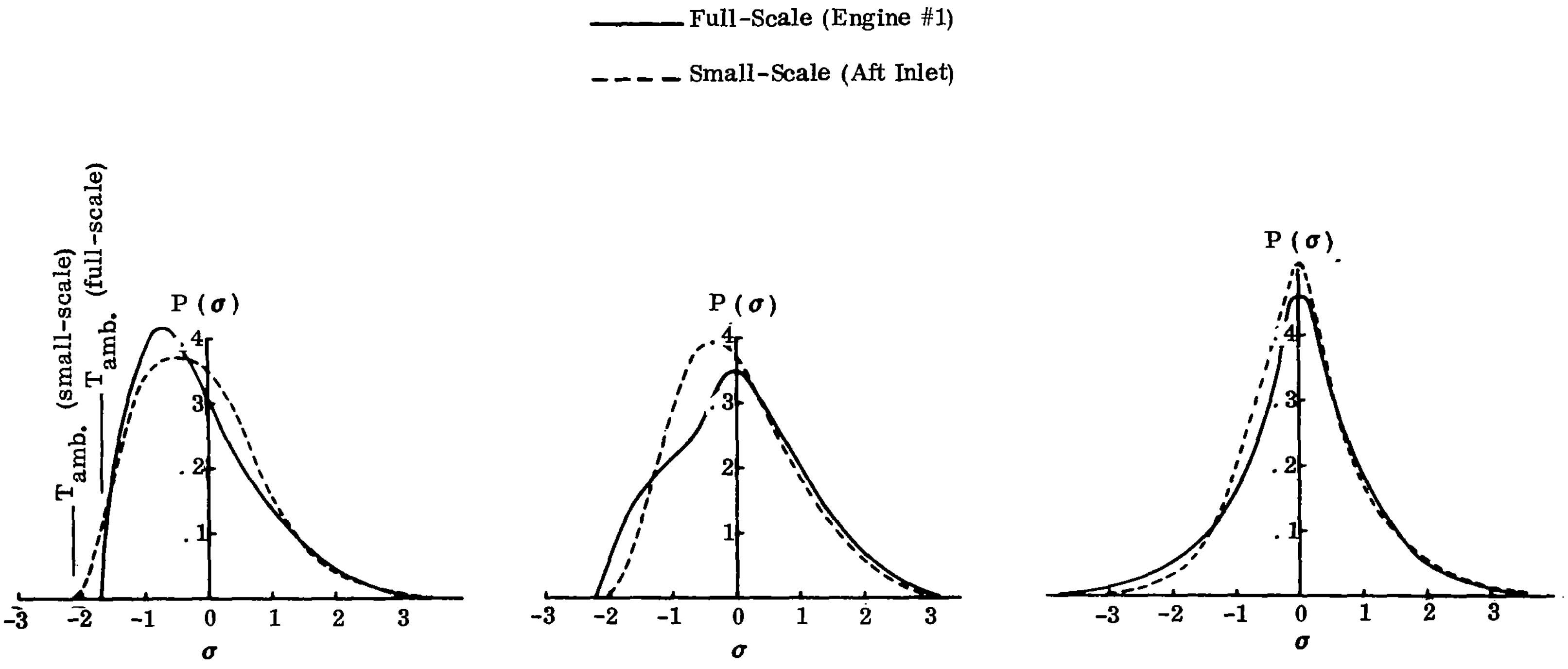

(a) $\Delta\overline{T}$

(b) ϵ_{max}

(c) $\dot{T}$

FIGURE 20. PROBABILITY DENSITY OF INGESTION CHARACTERISTICS

Two Engine Operation
H/D = 4
Wind <4 MPH

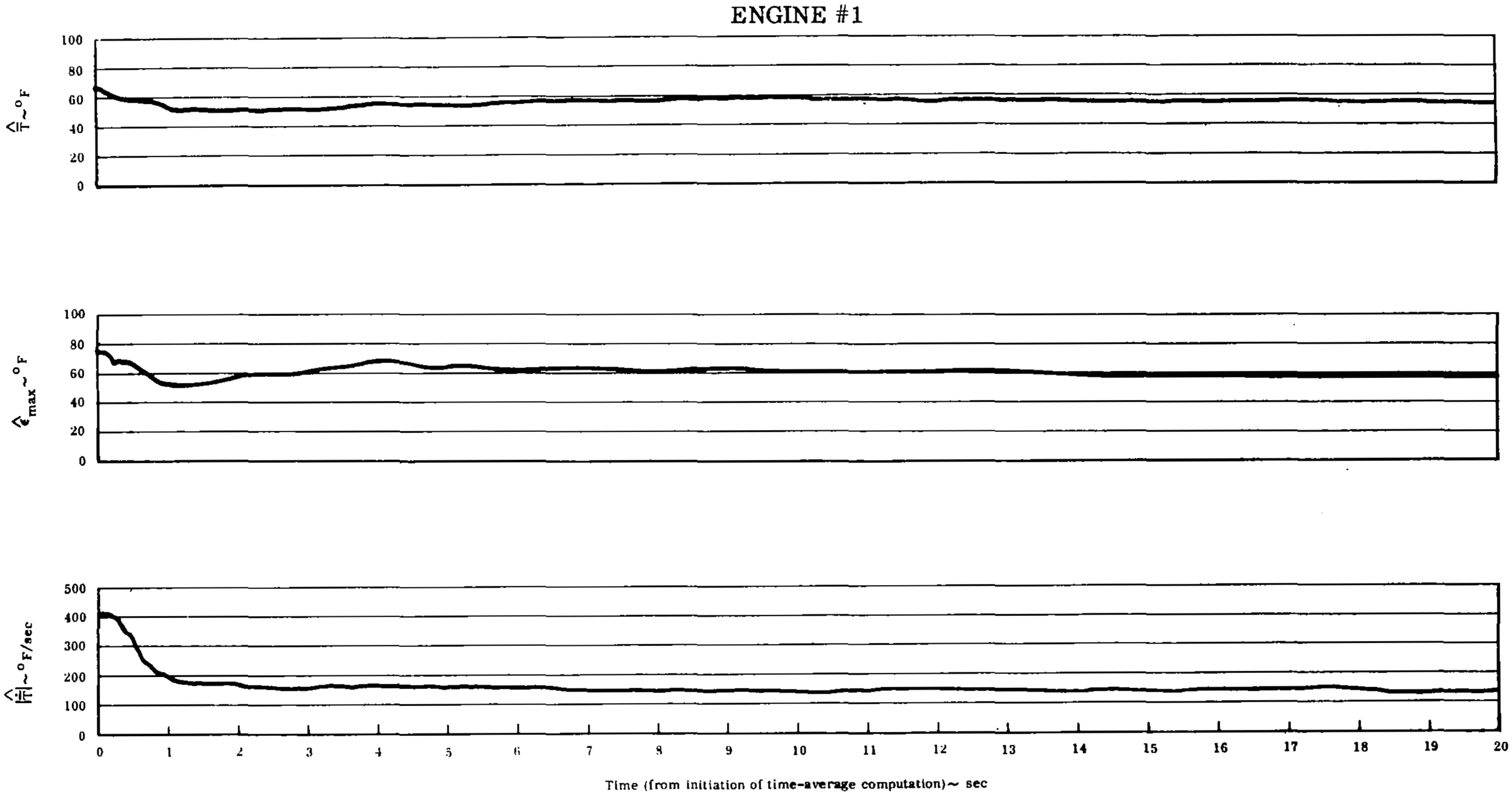

FIGURE 21. FULL-SCALE INGESTION CHARACTERISTICS CUMULATIVE TIME-AVERAGE

Two Engine Operation
H/D = 4
Wind <4 MPH

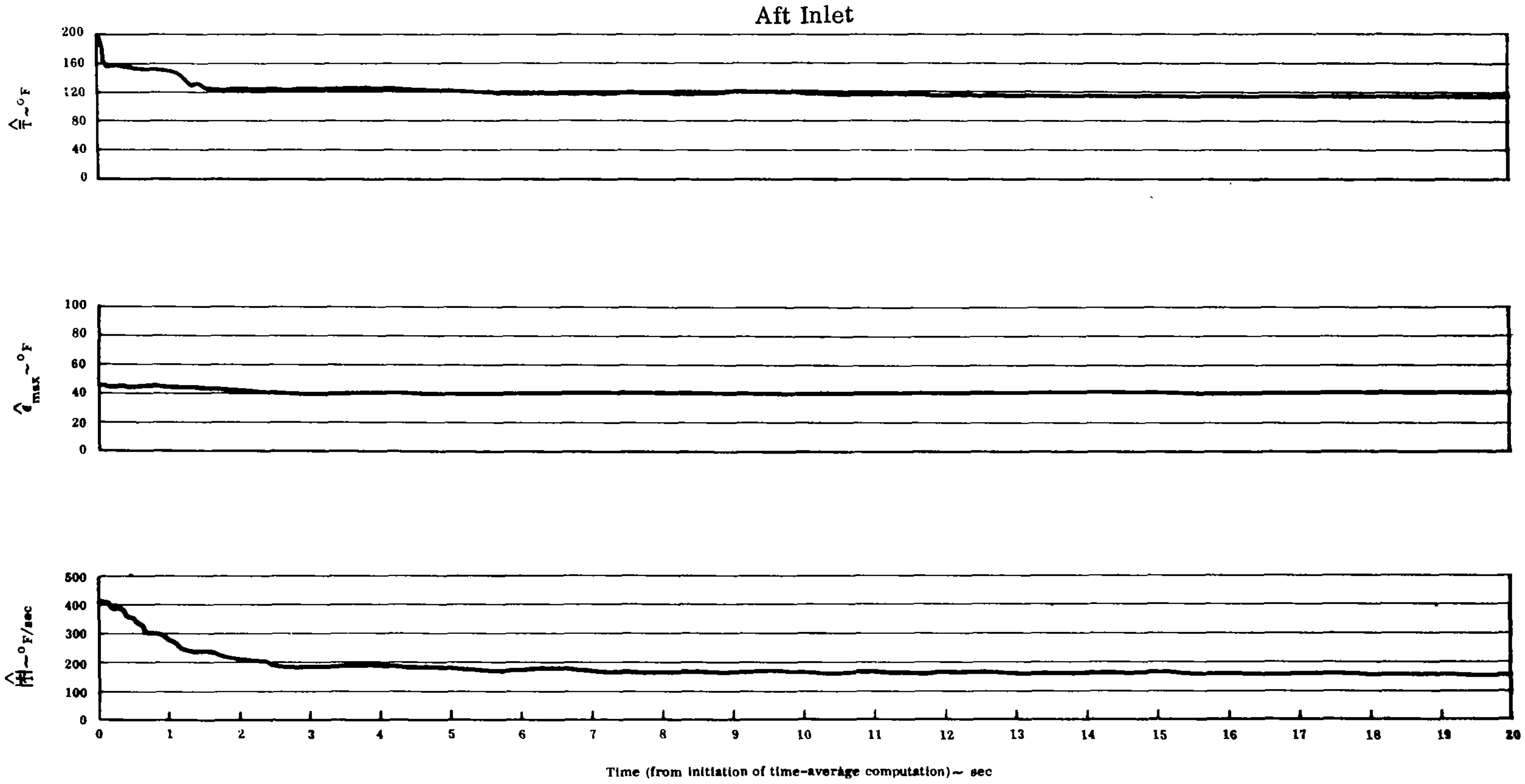

FIGURE 22. SMALL-SCALE INGESTION CHARACTERISTICS CUMULATIVE TIME-AVERAGE

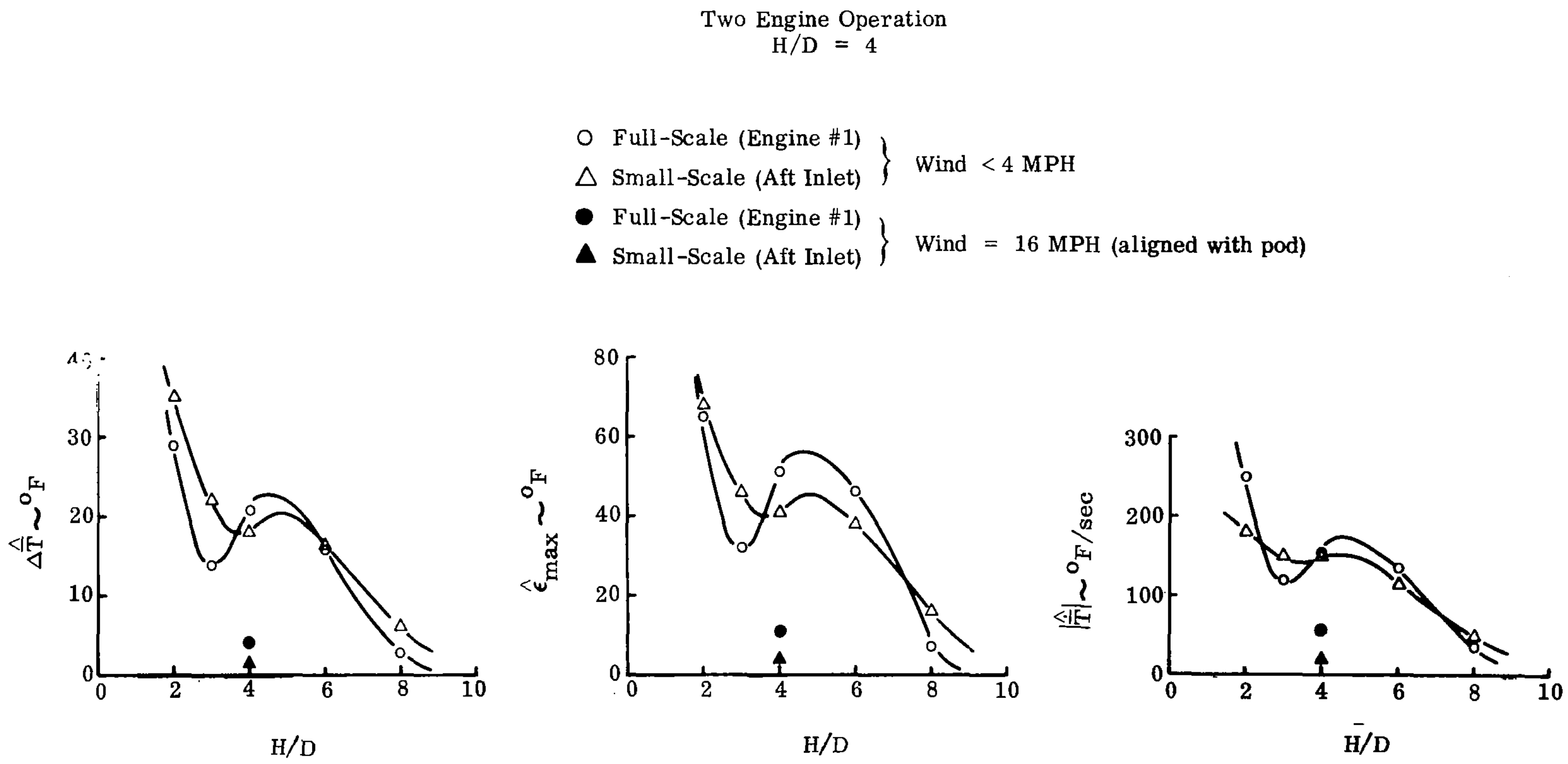

FIGURE 23. VARIATION IN TIME-AVERAGE INGESTION CHARACTERISTICS WITH H/D

Two Engine Operation
H/D = 4
Wind <4 MPH

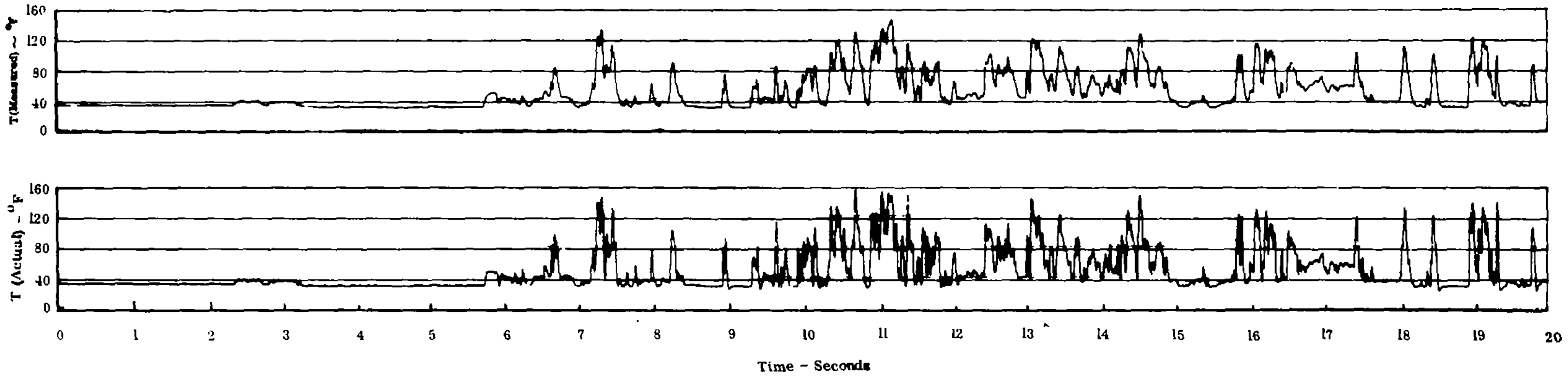

(a) Full-Scale

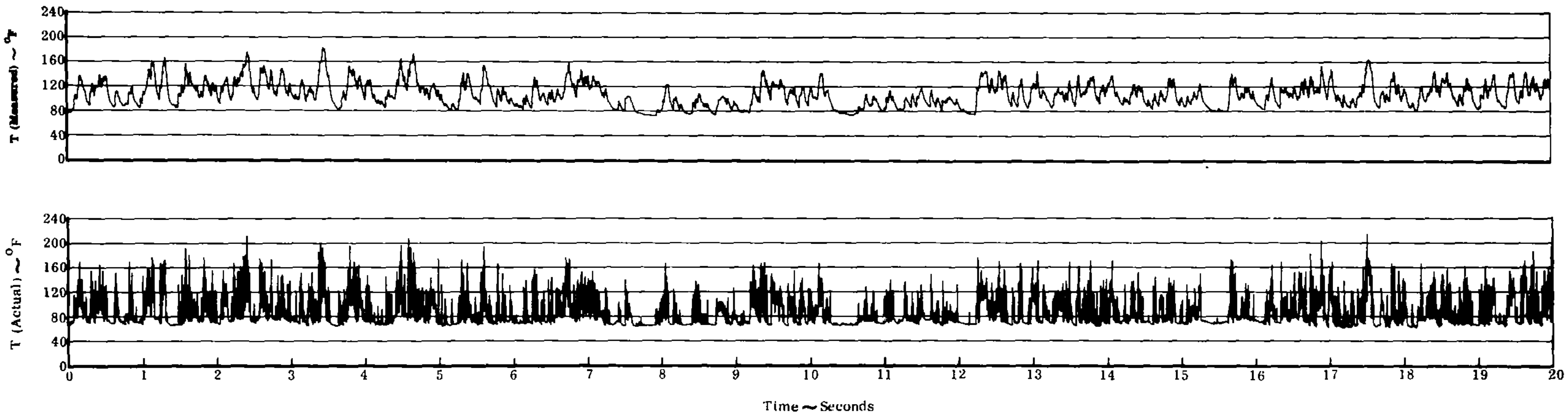

(b) Small-Scale

FIGURE 24. COMPARISON OF MEASURED AND CORRECTED INLET TEMPERATURE HISTORIES

Two Engine Operation
H/D = 4
Wind <4 MPH

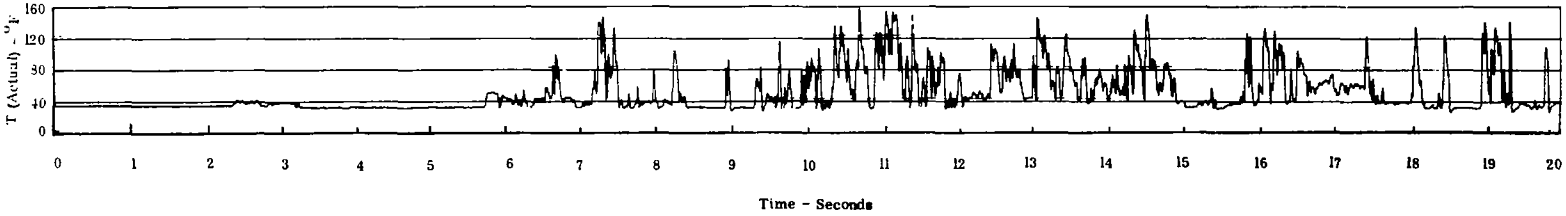

(a) Full-Scale

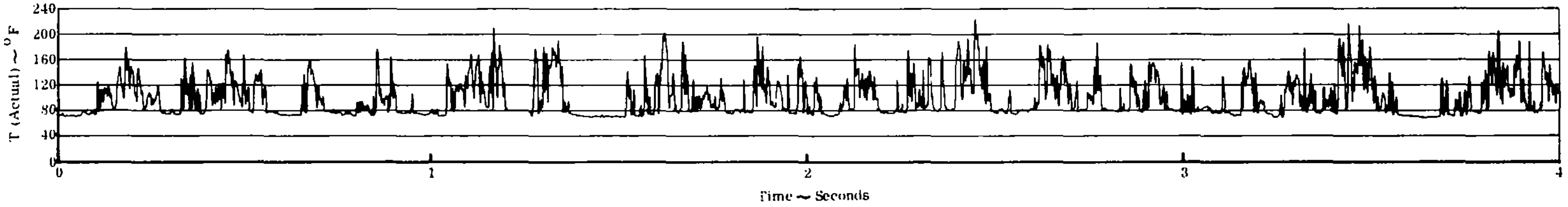

(b) Small-Scale

FIGURE 25. TIME-SCALED CORRECTED INLET TEMPERATURE HISTORIES

Two Engine Operation
H/D = 4
Wind <4 MPH

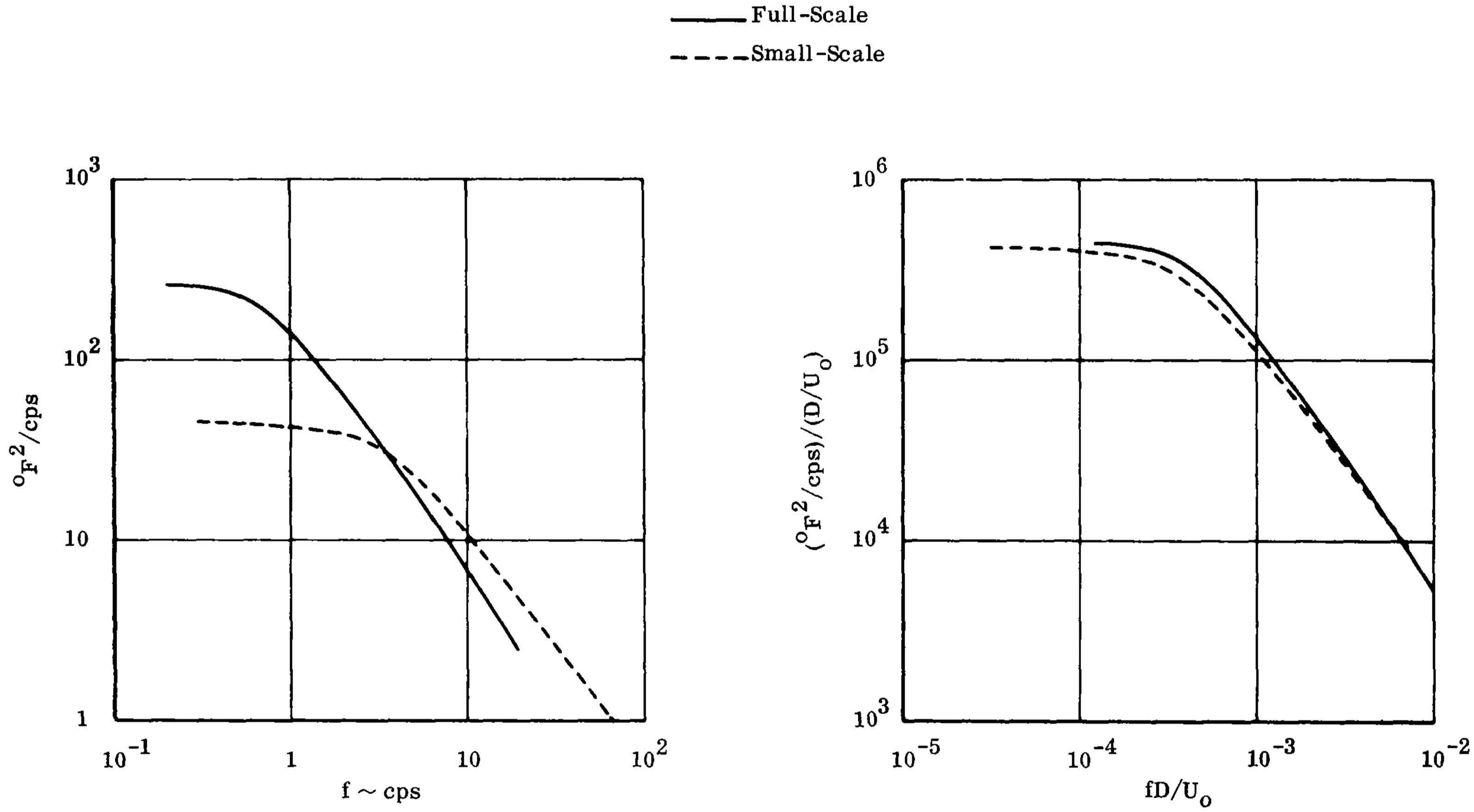

(a) Absolute Power Spectra

(b) Non-Dimensional Power Spectra

FIGURE 26. POWER SPECTRAL DENSITY OF CORRECTED INLET TEMPERATURE HISTORIES

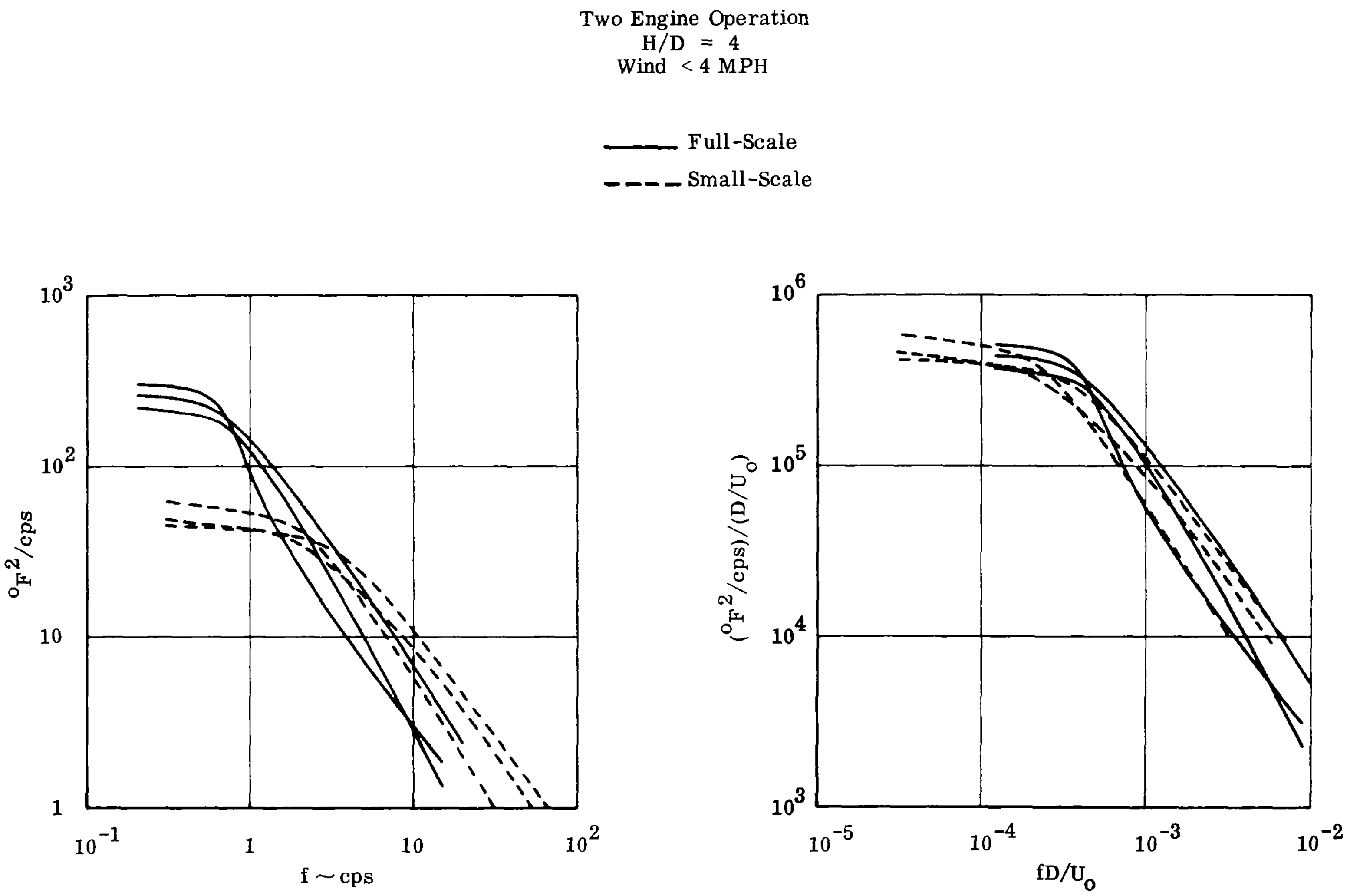

(a) Absolute Power Spectra

(b) Non-Dimensional Power Spectra

FIGURE 27. POWER SPECTRAL DENSITY OF CORRECTED INLET TEMPERATURE HISTORIES

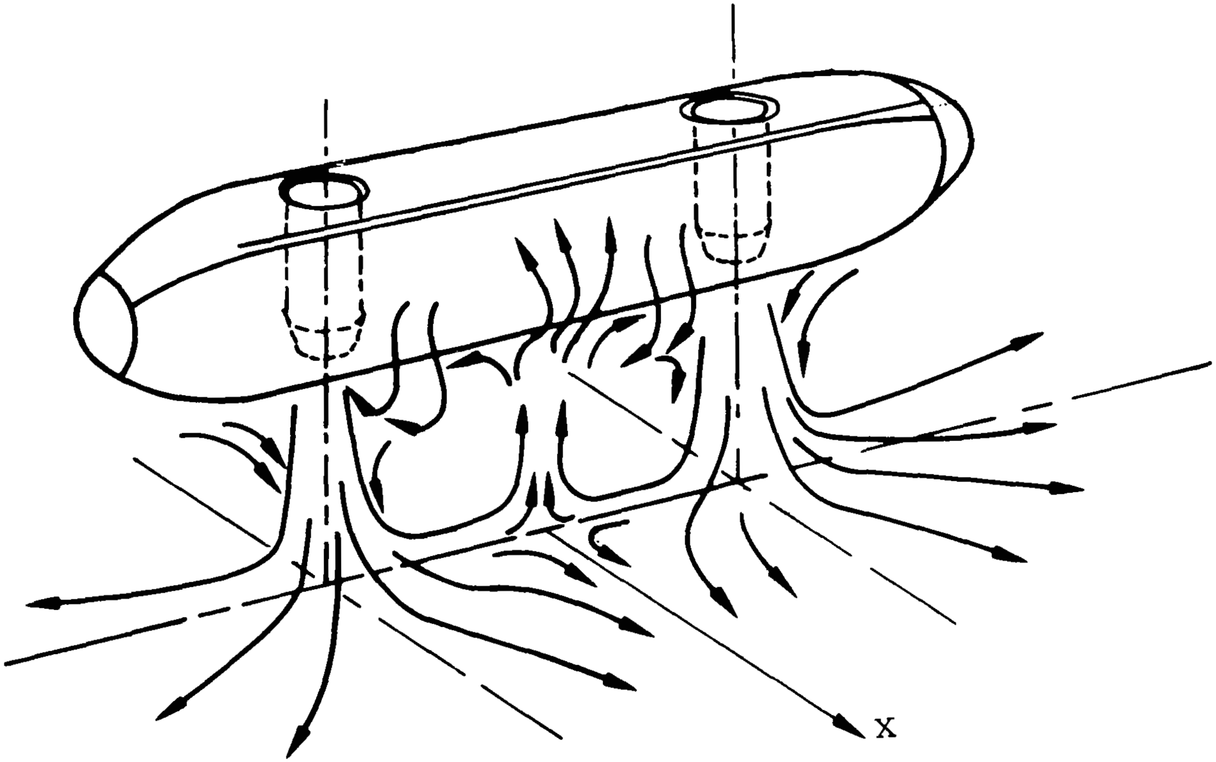

FIGURE 28. FLOW STRUCTURE BETWEEN GROUND PLANE AND POD FOR TWO ENGINE OPERATION

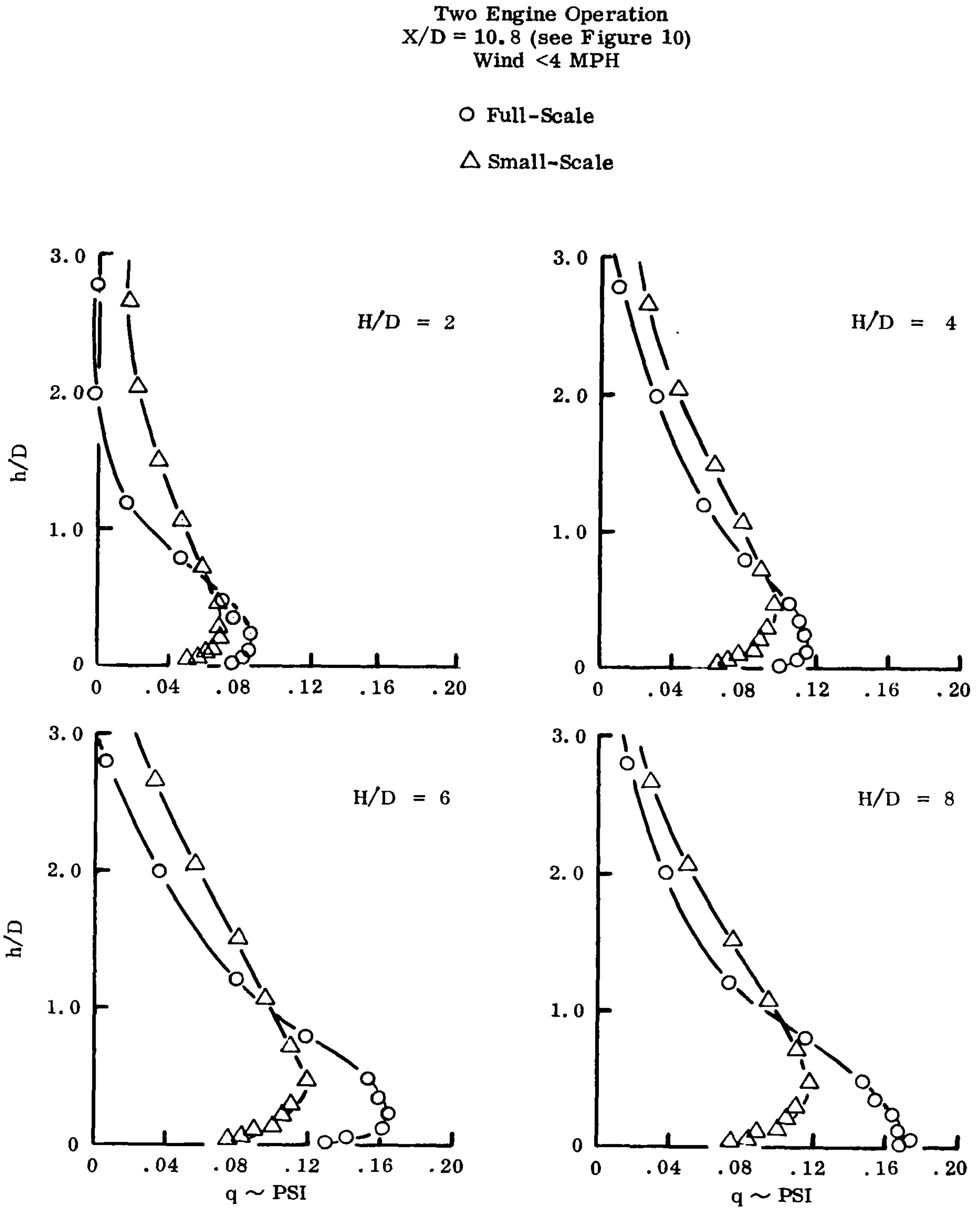

FIGURE 29. GROUND JET DYNAMIC PRESSURE PROFILES

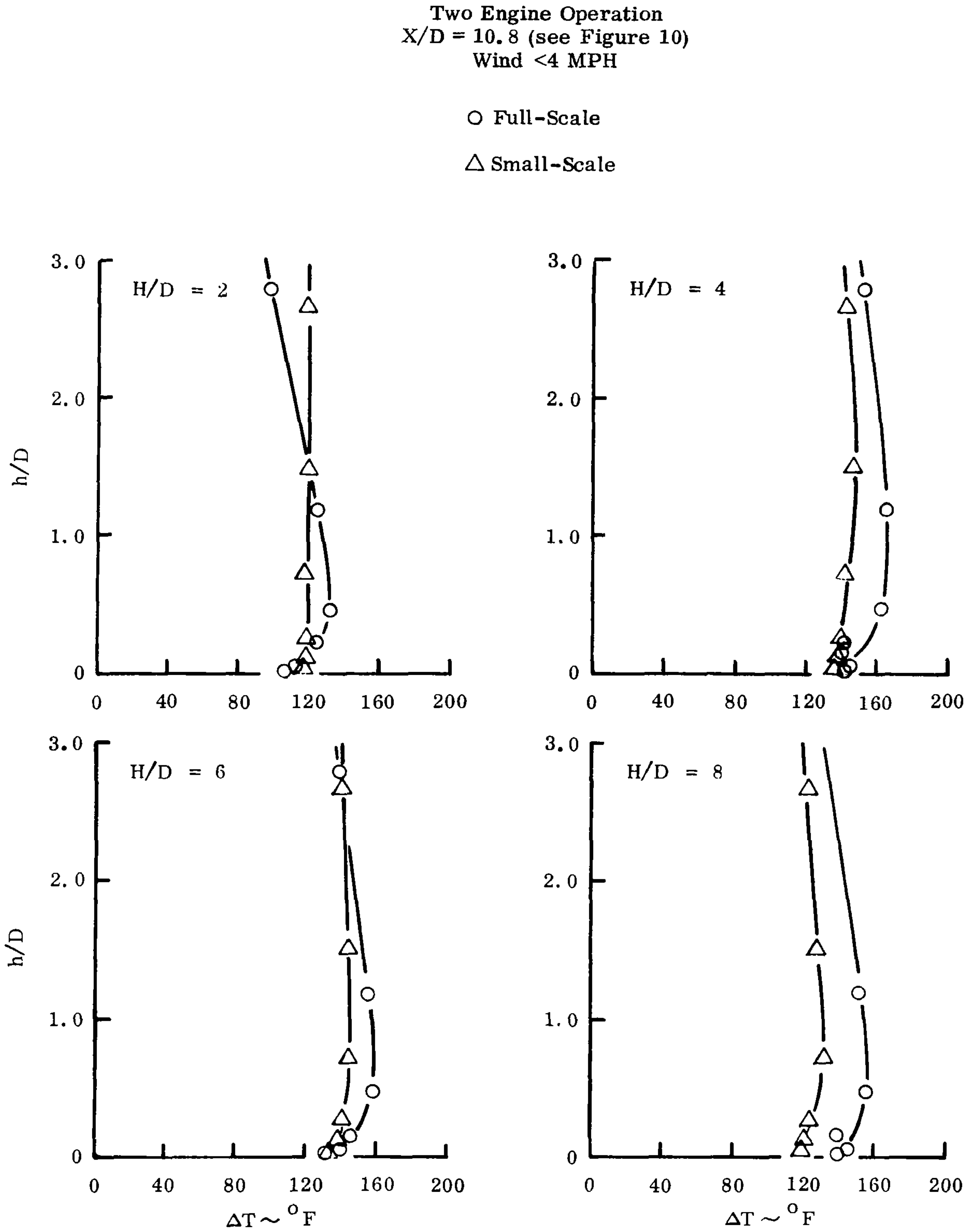

FIGURE 30. GROUND JET TEMPERATURE PROFILES

Single Engine Operation
X/D = 10.8 (see Figure 10)
Wind < 4 MPH

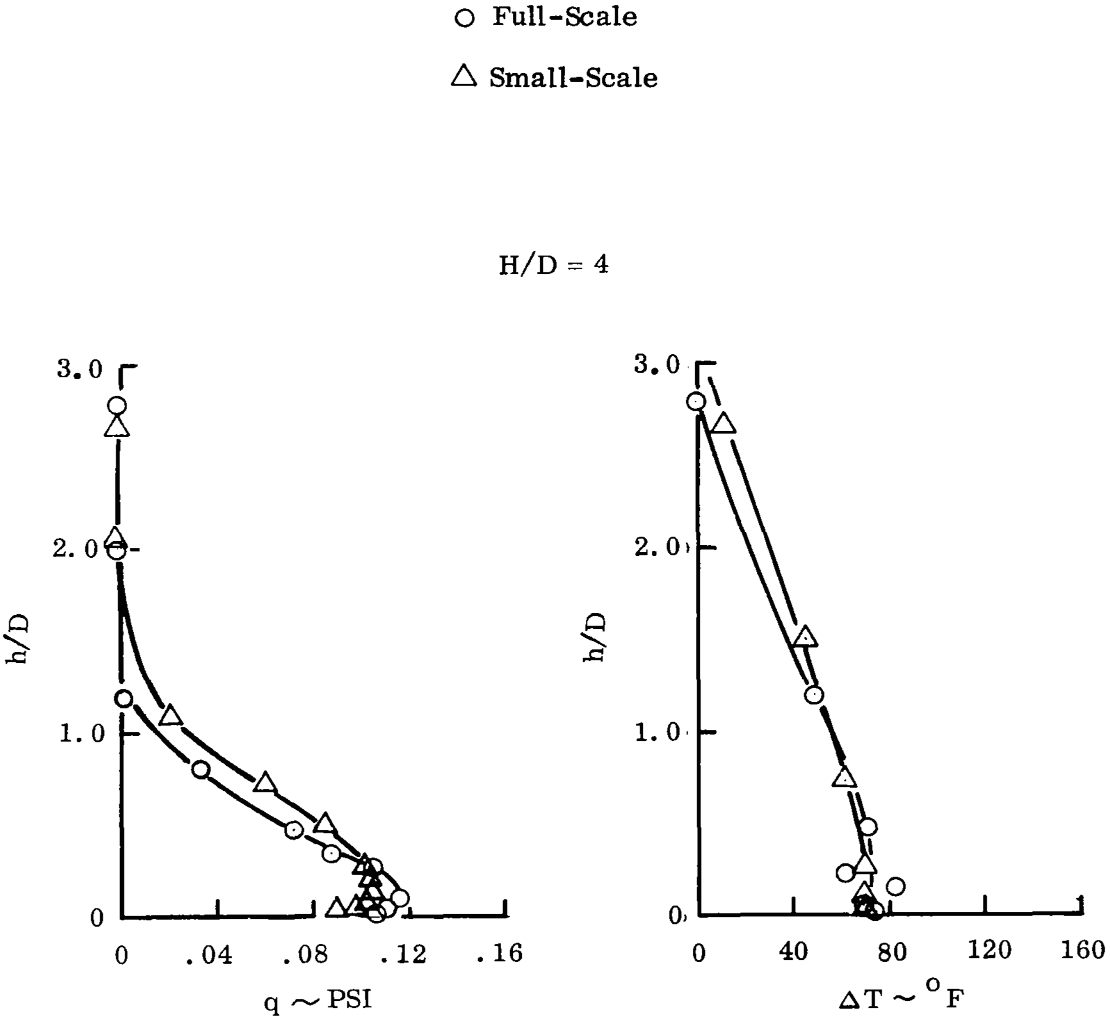

FIGURE 31. GROUND JET DYNAMIC PRESSURE AND TEMPERATURE PROFILES

Two Engine Operation
X/D = 10.8 (see Figure 10)
Wind = 16 MPH

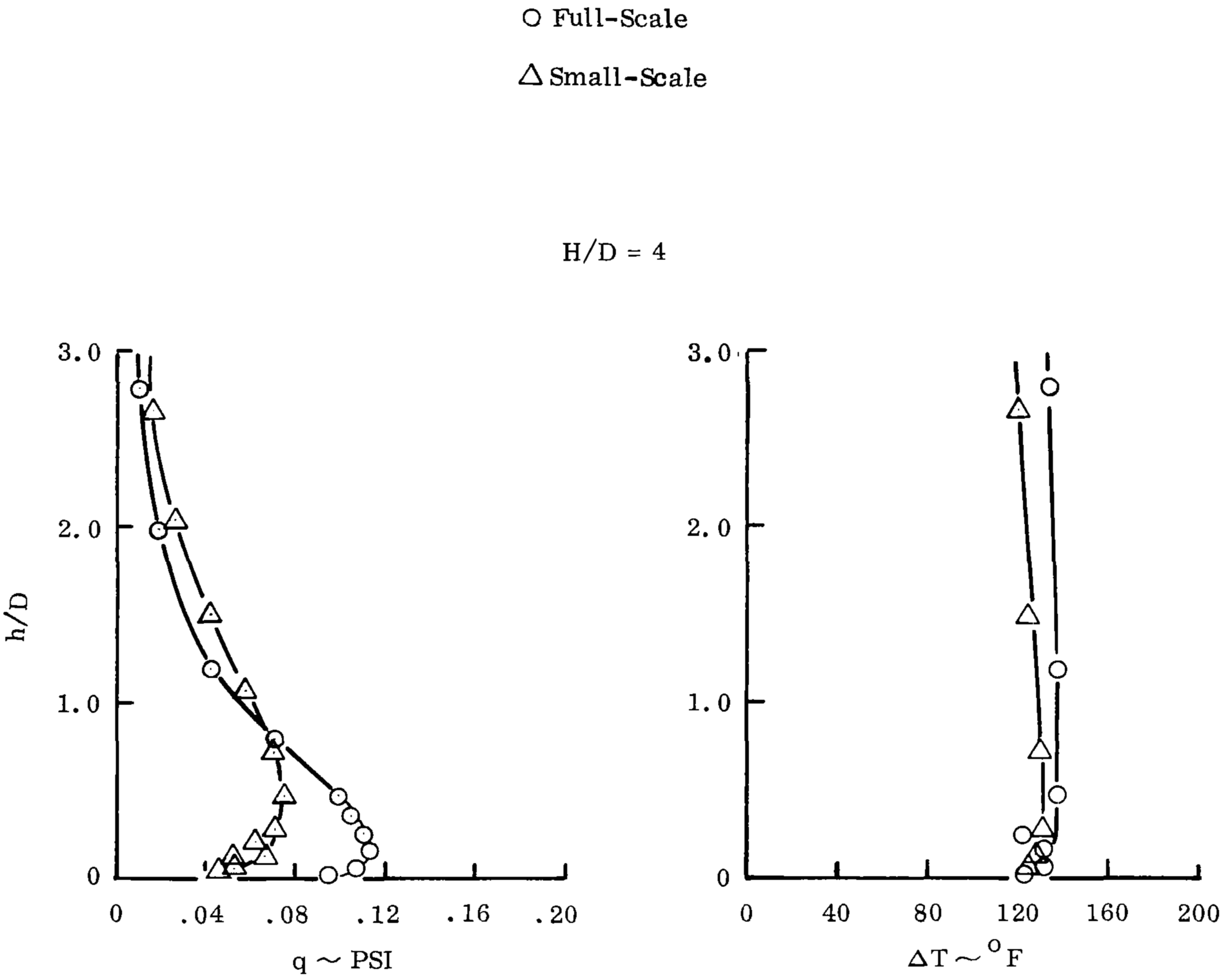

FIGURE 32. GROUND JET DYNAMIC PRESSURE AND TEMPERATURE PROFILES

Two Engine Operation
H/D = 4
Wind <4 MPH

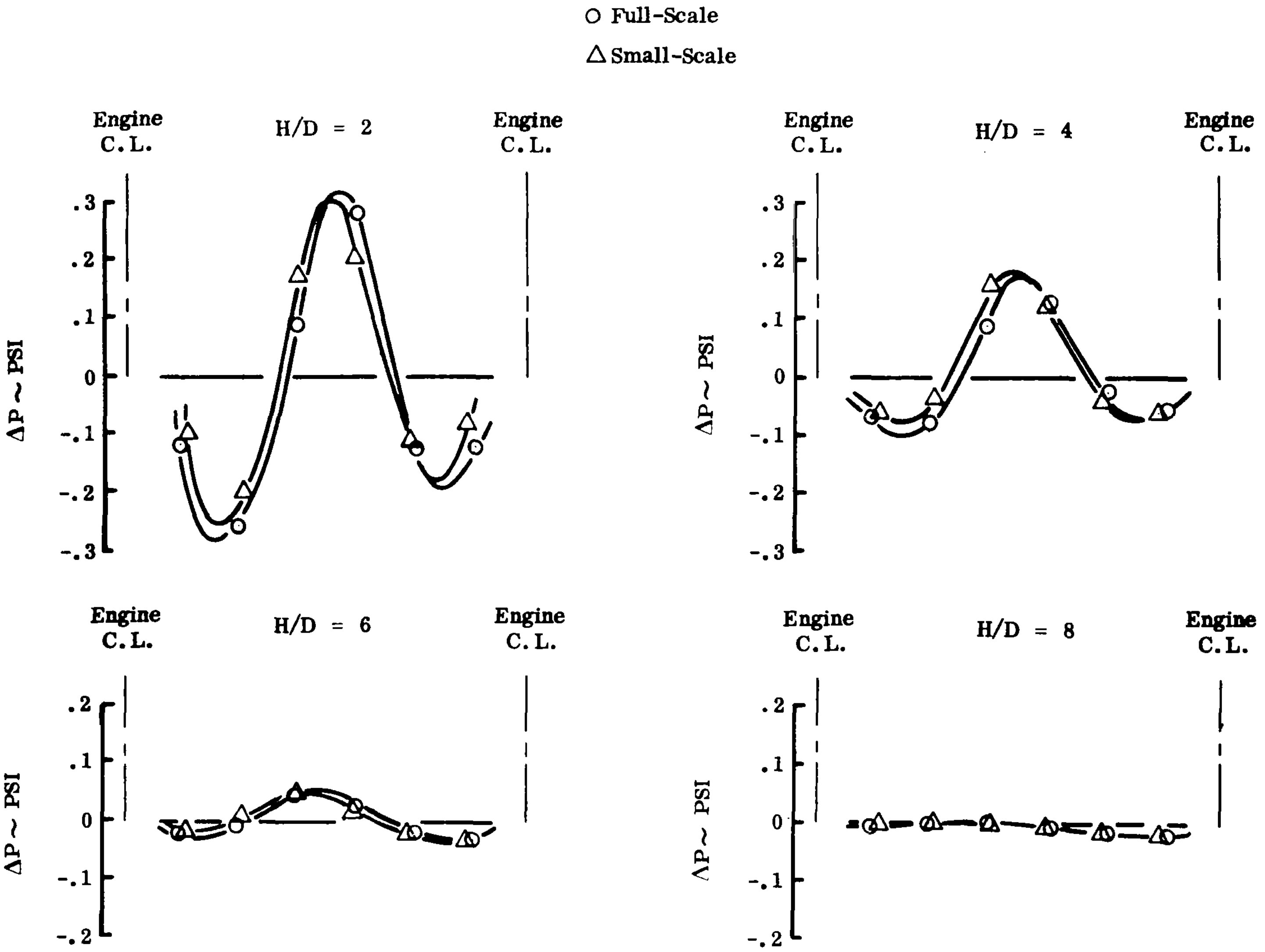

FIGURE 33. POD PRESSURE DISTRIBUTION

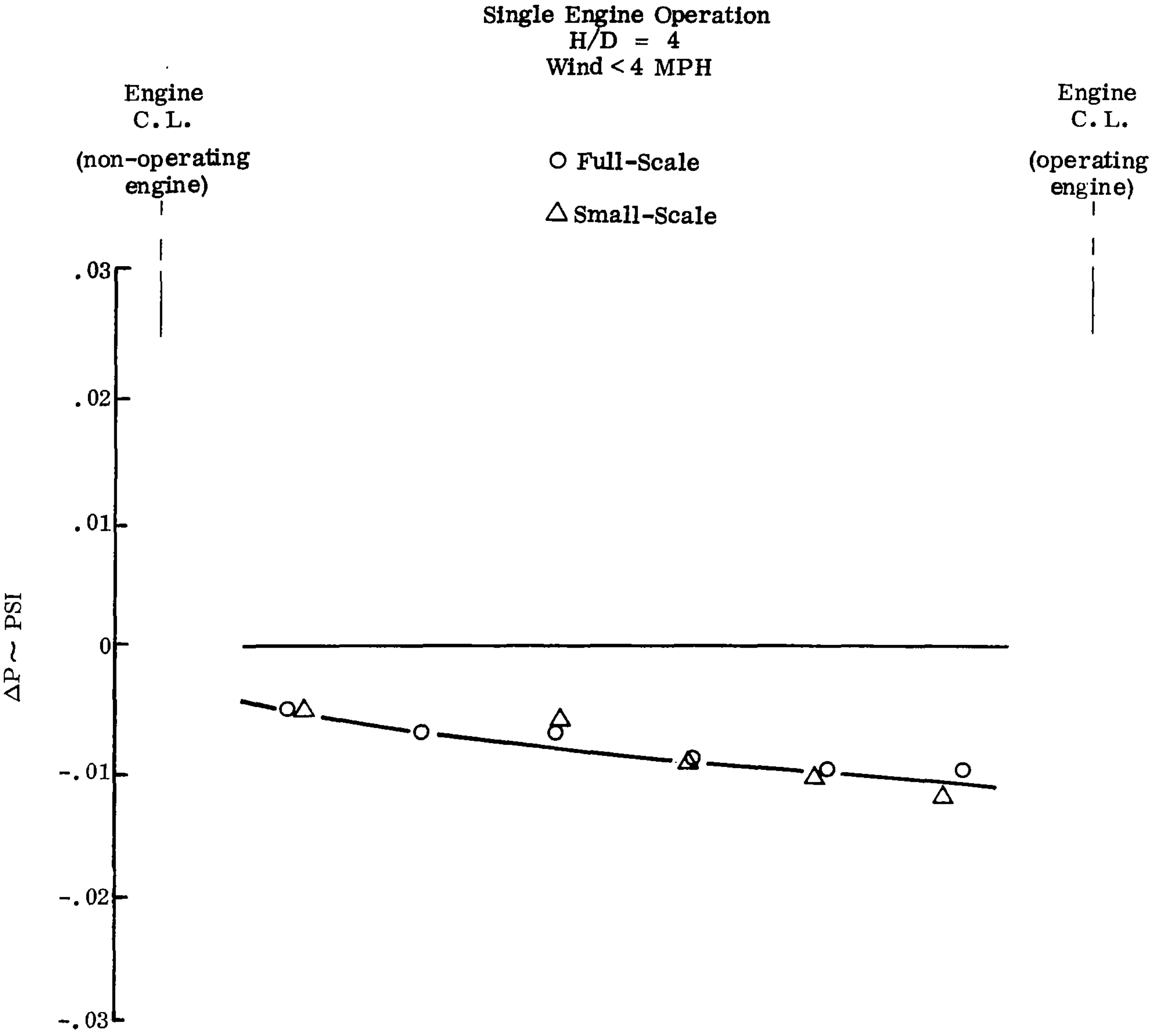

FIGURE 34. POD PRESSURE DISTRIBUTION

Two Engine Operation
H/D = 4
Wind = 16 MPH

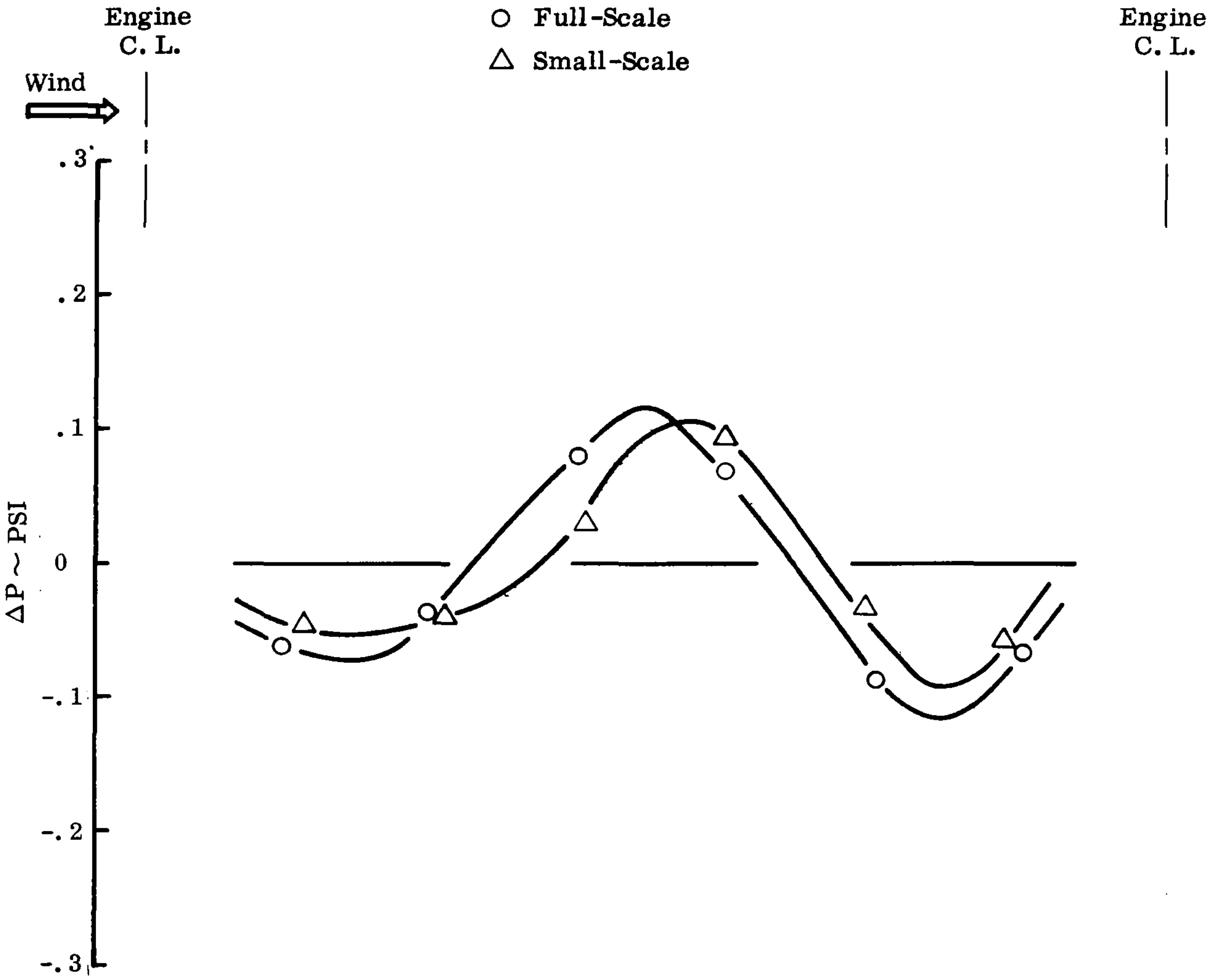

FIGURE 35. POD PRESSURE DISTRIBUTION

APPENDIX

Presented herein are full-scale/small-scale ingestion indices for each of the tests of Table A-1. In addition, time histories of the raw inlet temperatures (uncorrected for thermocouple lag) are presented as indicated.

The nominal period of computation of the time-average ingestion indices was 30 seconds, computation being initiated upon reaching full thrust in the full-scale tests and following trap door closure in the small-scale tests. The accuracy of the time varying and time-average ingestion indices is considered to be about ±2°F.

TABLE A-1

Test No.	Engines Operating	Pod Height H/D	Wind Velocity	Ambient Temp ~ °F		Appendix Data	
				Full Scale	Small Scale	Ingestion Indices	Raw Inlet Temp.
1	2	2	<4 MPH	40	72	X	
2	↓	3	↓	38	72	X	
3		4		40	90	X	X
4		6		40	64	X	
5		8		38	80	X	
6	2	4	16 MPH (aligned with pod)	42	68	X	X
7	1	4	<4 MPH	38	62	X	X
8	1	4	16 MPH (aligned with pod)	44	64	X	X

Test 1

Two Engine Operation

$H/D = 2$

Wind < 4 MPH

TIME-AVERAGE INGESTION CHARACTERISTICS

	Full-Scale		Small-Scale	
	Engine #1	Engine #4	Fwd Inlet	Aft Inlet
$\Delta\hat{\bar{T}}$	29°F	6°F	6°F	35°F
$\hat{\epsilon}_{max}$	62°F	10°F	11°F	68°F
$\lvert\hat{\dot{T}}\rvert$	250°F/sec	—	40°F/sec	180°F/sec

Test 1

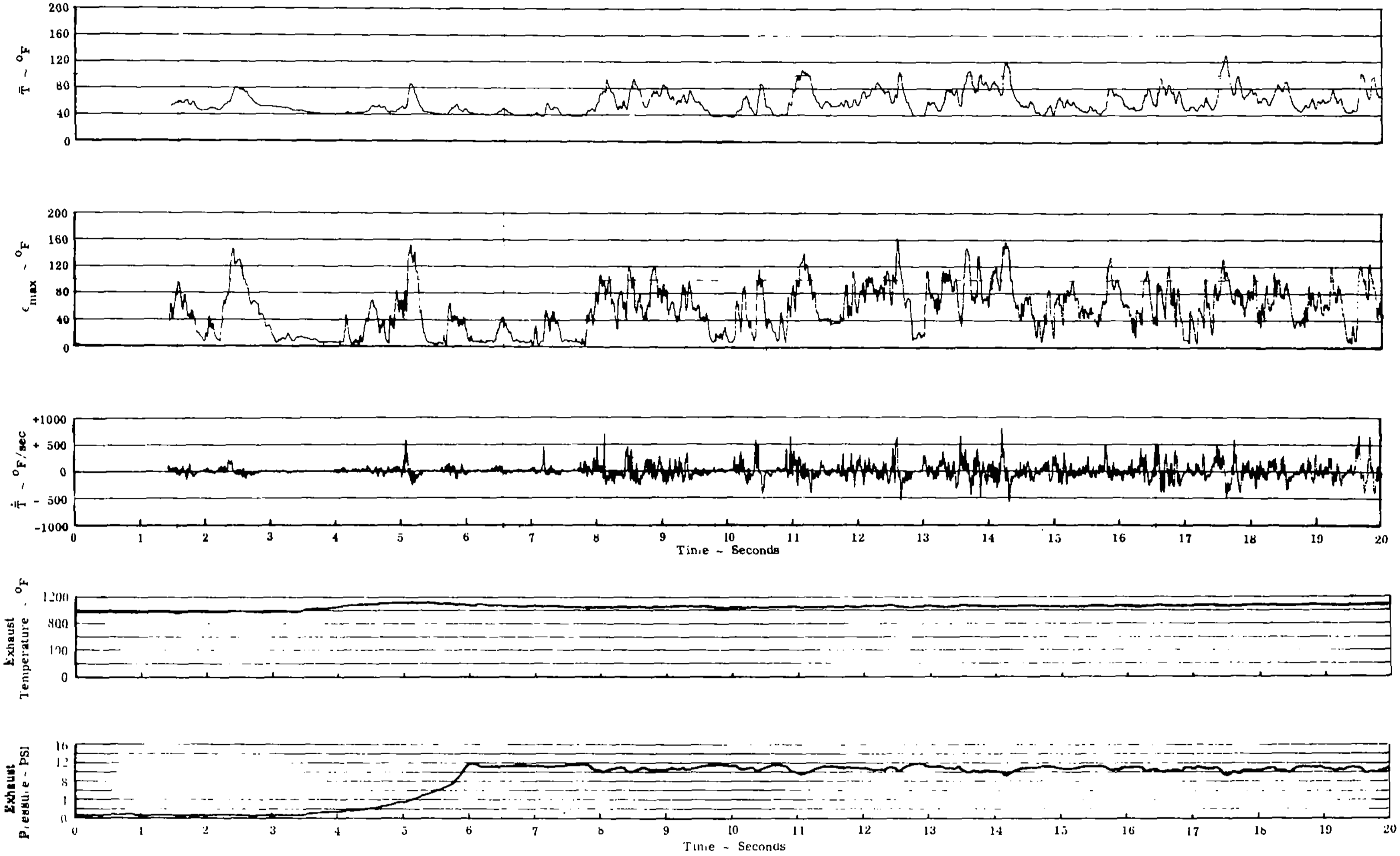

(a) ENGINE #1

FIGURE A1-1. FULL-SCALE INGESTION CHARACTERISTICS HISTORY

Test 1

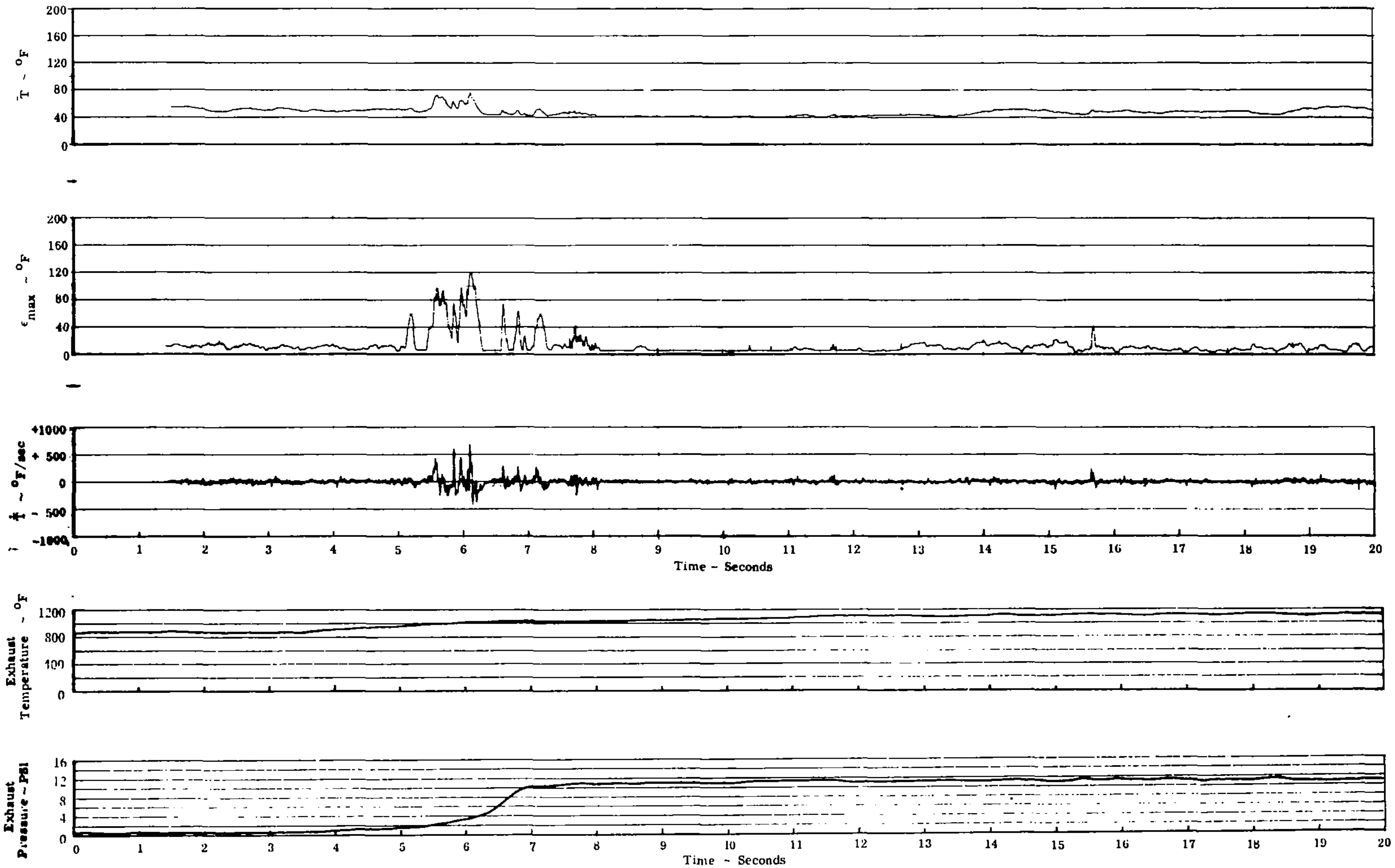

(b) ENGINE #4

FIGURE A1-1 (cont'd) FULL-SCALE INGESTION CHARACTERISTICS HISTORY

Test 1

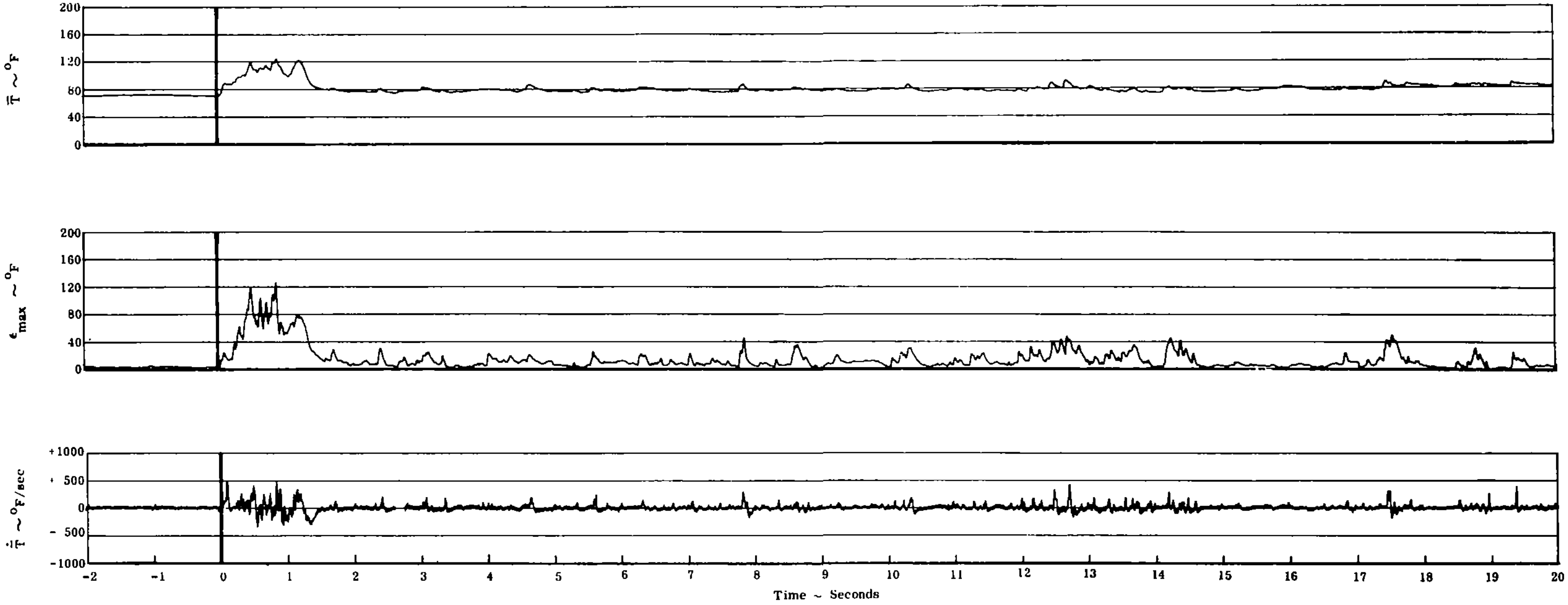

(a) FORWARD INLET

FIGURE A1-2. SMALL-SCALE INGESTION CHARACTERISTICS HISTORY

Test 1

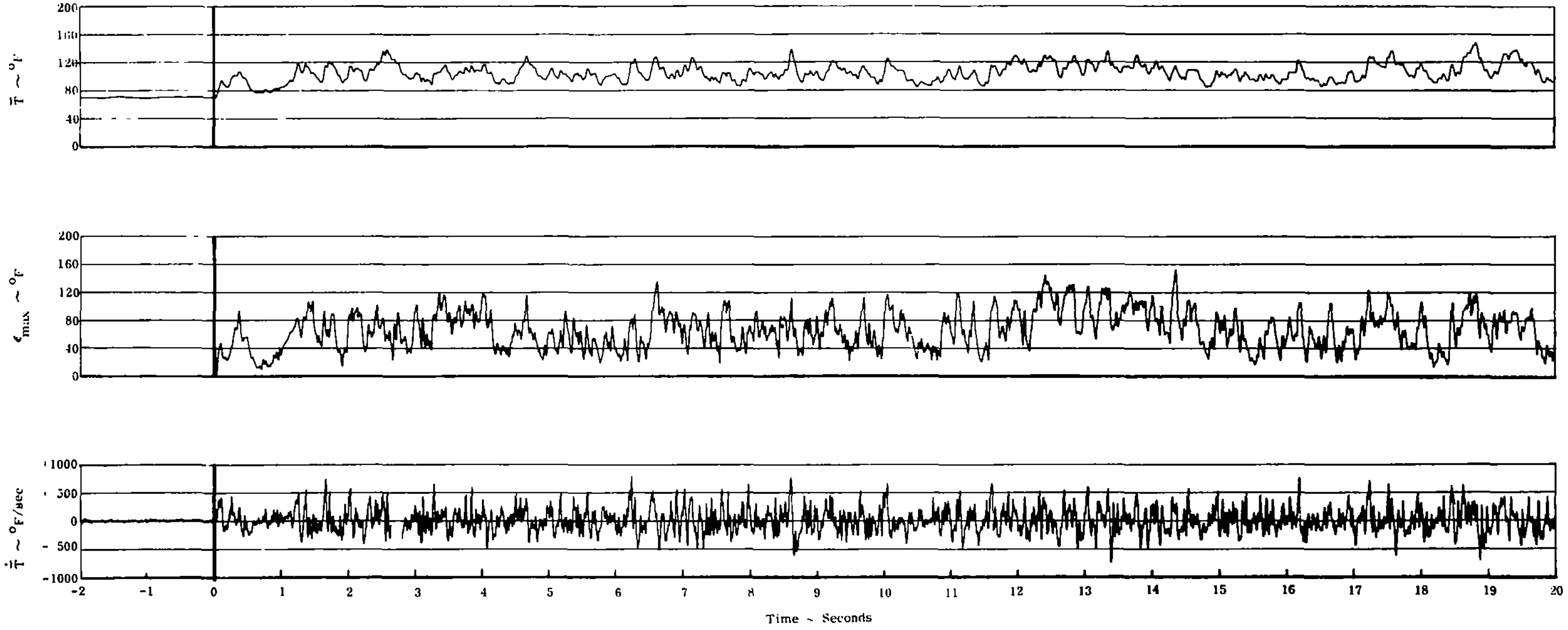

(b) AFT INLET

FIGURE A1-2 (cont'd) SMALL-SCALE INGESTION CHARACTERISTICS HISTORY

Test 2

Two Engine Operation

H/D = 3

Wind < 4 MPH

TIME-AVERAGE INGESTION CHARACTERISTICS

	Full-Scale		Small-Scale	
	Engine #1	Engine #4	Fwd Inlet	Aft Inlet
$\Delta\hat{T}$	14°F	1°F	6°F	22°F
$\hat{\epsilon}_{max}$	32°F	4°F	8°F	46°F
$\lvert\hat{\dot{T}}\rvert$	120°F/sec	——	30°F/sec	150°F/sec

Test 2

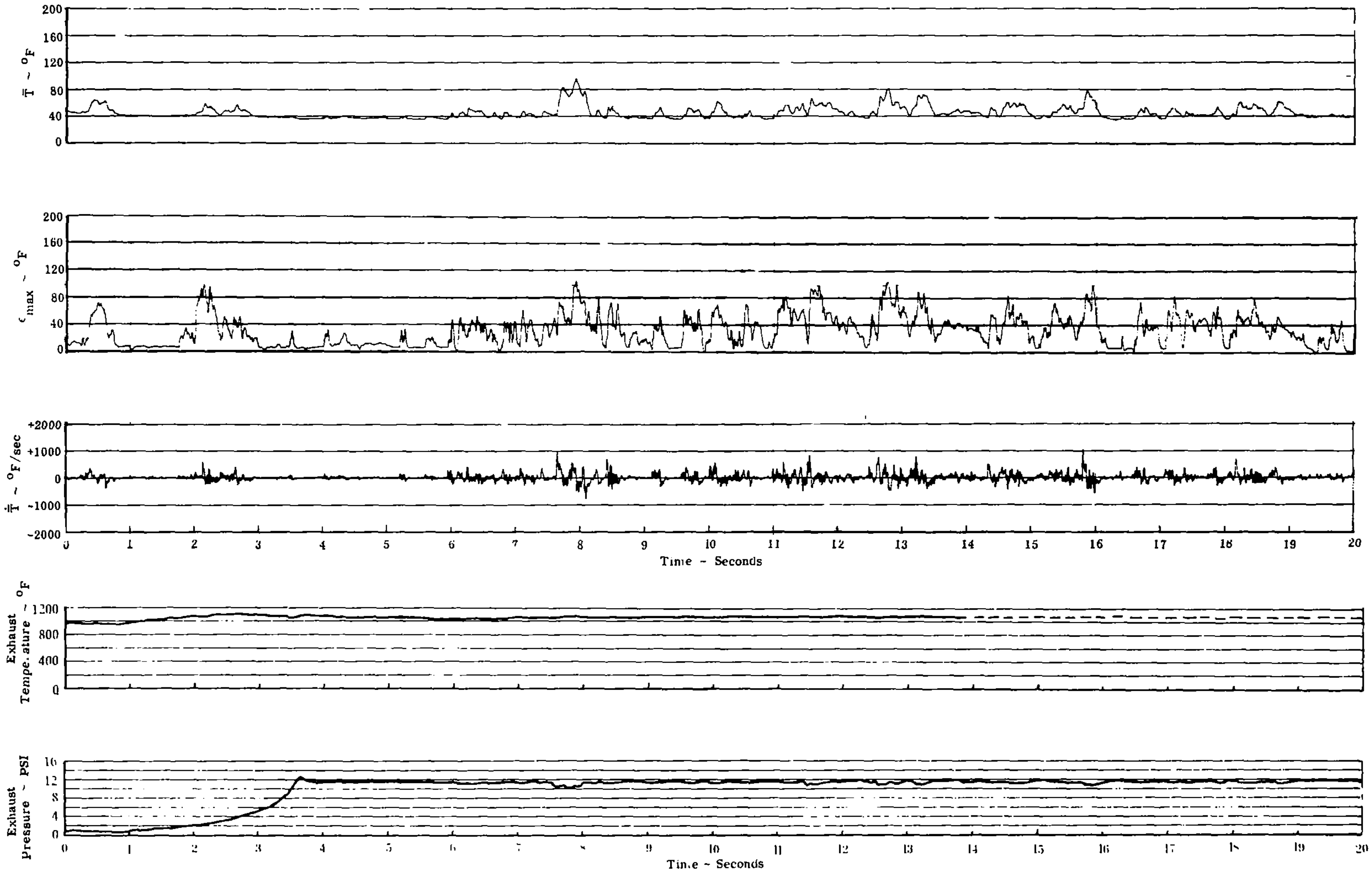

(a) ENGINE #1

FIGURE A2-1. FULL-SCALE INGESTION CHARACTERISTICS HISTORY

Test 2

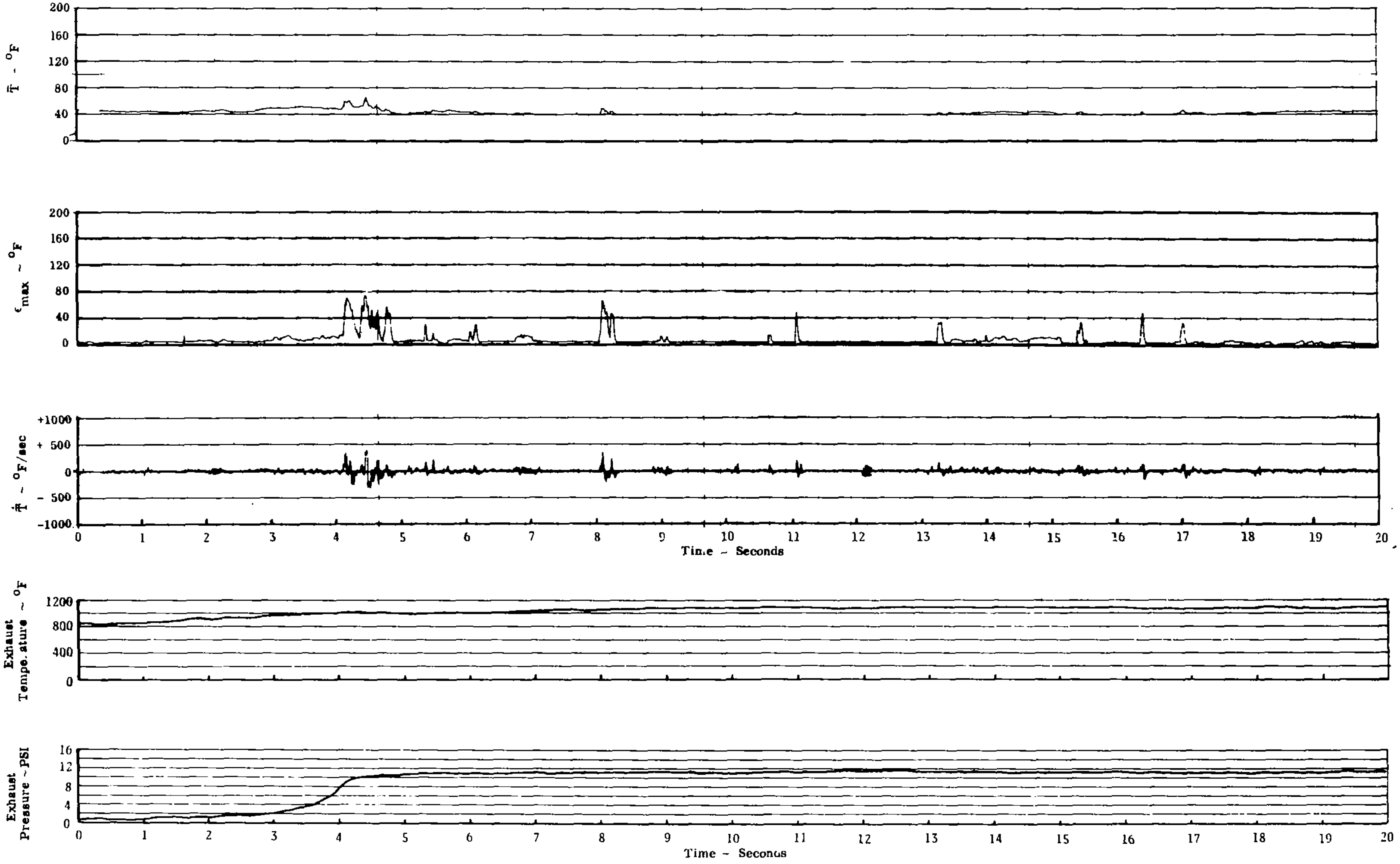

(b) ENGINE #4

FIGURE A2-1 (cont'd). FULL-SCALE INGESTION CHARACTERISTICS HISTORY

Test 2

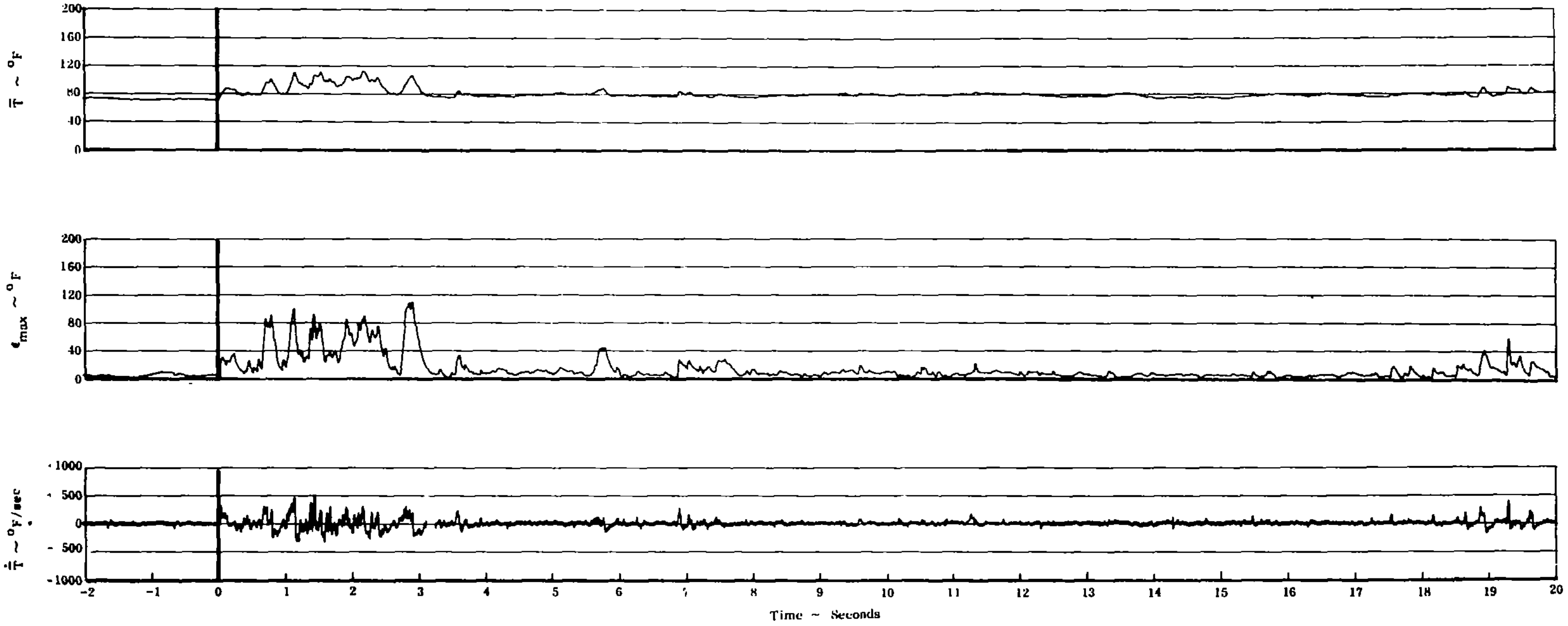

(a) FORWARD INLET

FIGURE A2-2. SMALL-SCALE INGESTION CHARACTERISTICS HISTORY

Test 2

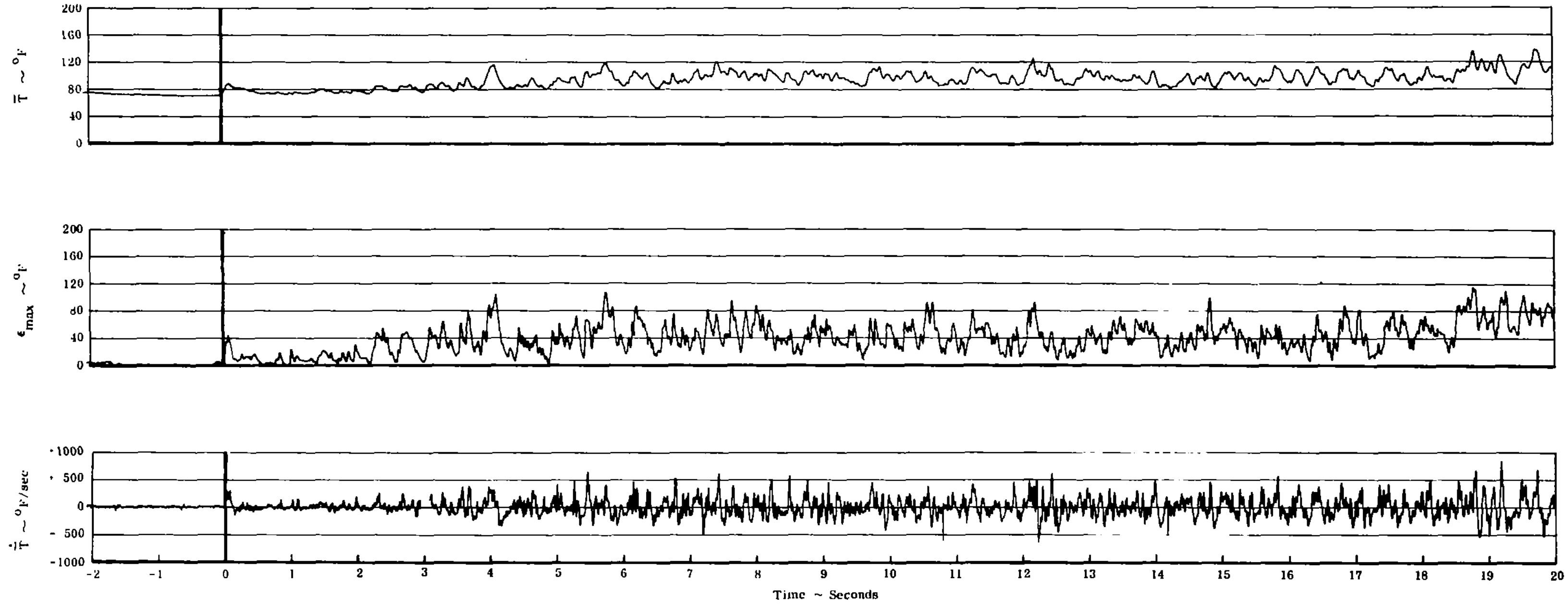

(b) AFT INLET

FIGURE A2-2 (cont'd). SMALL-SCALE INGESTION CHARACTERISTICS HISTORY

Test 3

Two Engine Operation

H/D = 4

Wind < 4 MPH

TIME-AVERAGE INGESTION CHARACTERISTICS

	Full-Scale		Small-Scale	
	Engine #1	Engine #4	Fwd Inlet	Aft Inlet
$\Delta\hat{T}$	21°F	4°F	4°F	18°F
$\hat{\epsilon}_{max}$	56°F	8°F	13°F	41°F
$\lvert\hat{\dot{T}}\rvert$	140°F/sec	——	40°F/sec	150°F/sec

Test 3

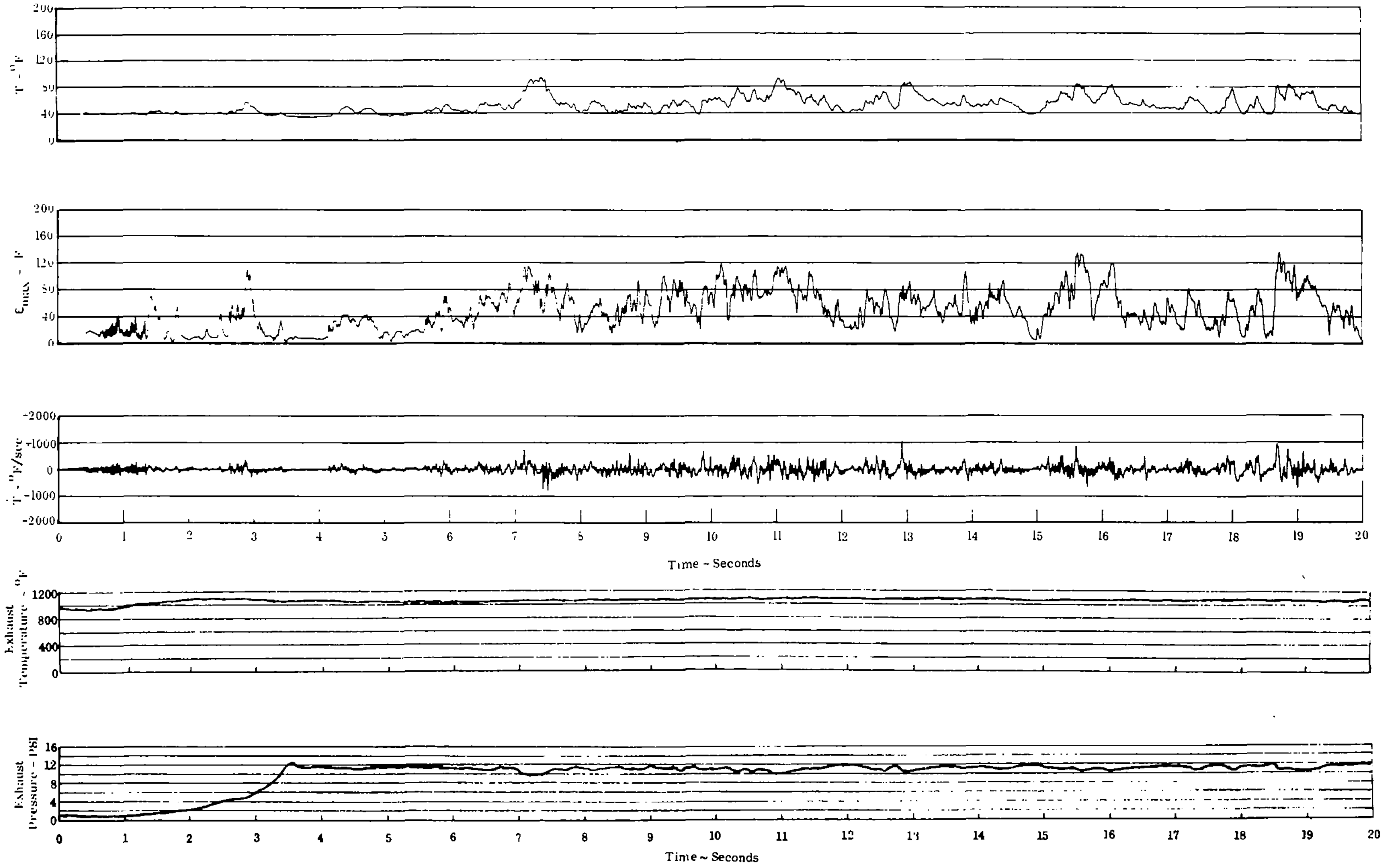

(a) ENGINE #1

FIGURE A3-1. FULL-SCALE INGESTION CHARACTERISTICS HISTORY

Test 3

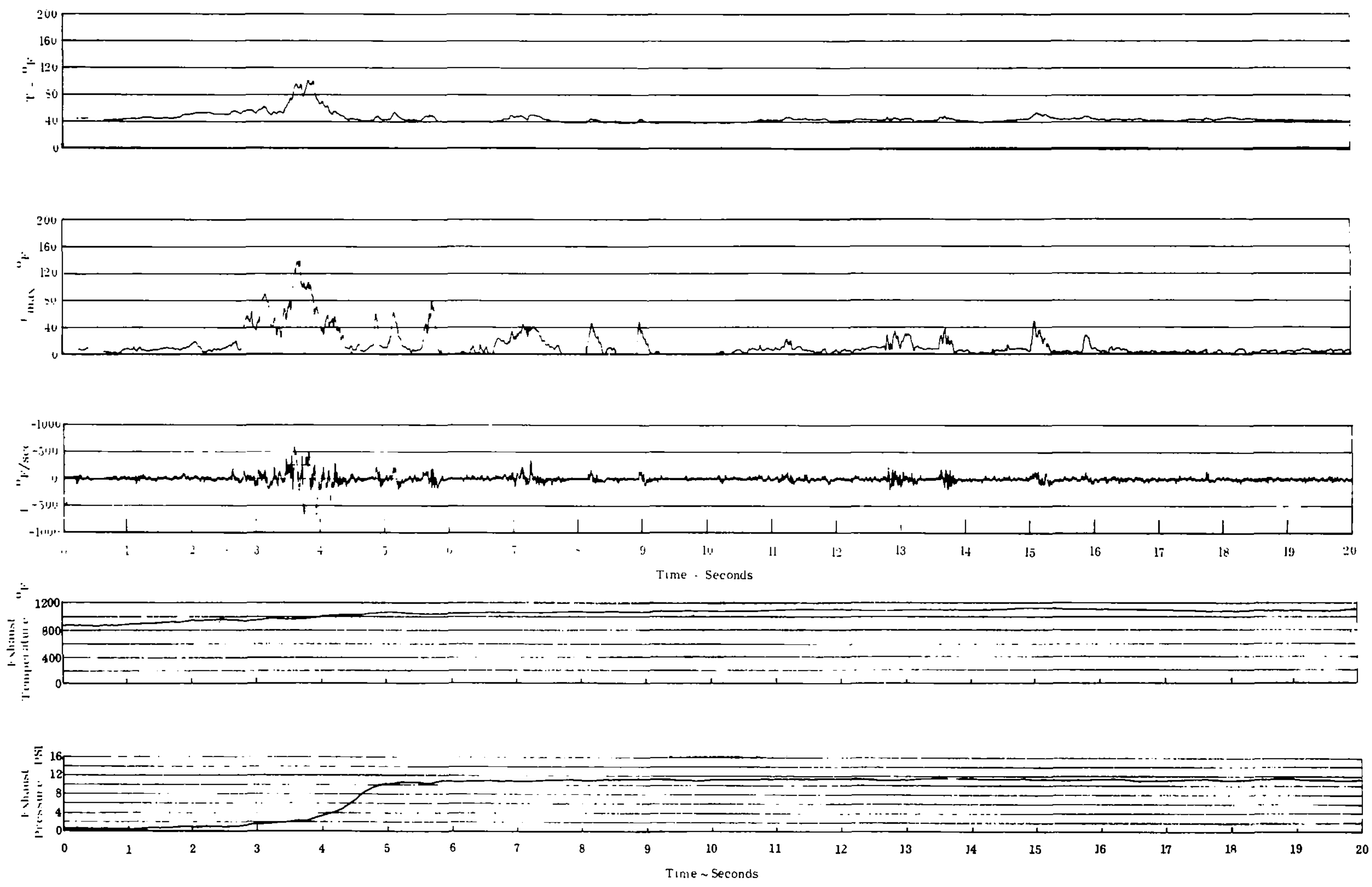

(b) ENGINE #4

FIGURE A3-1 (cont'd) FULL-SCALE INGESTION CHARACTERISTICS HISTORY

Test 3

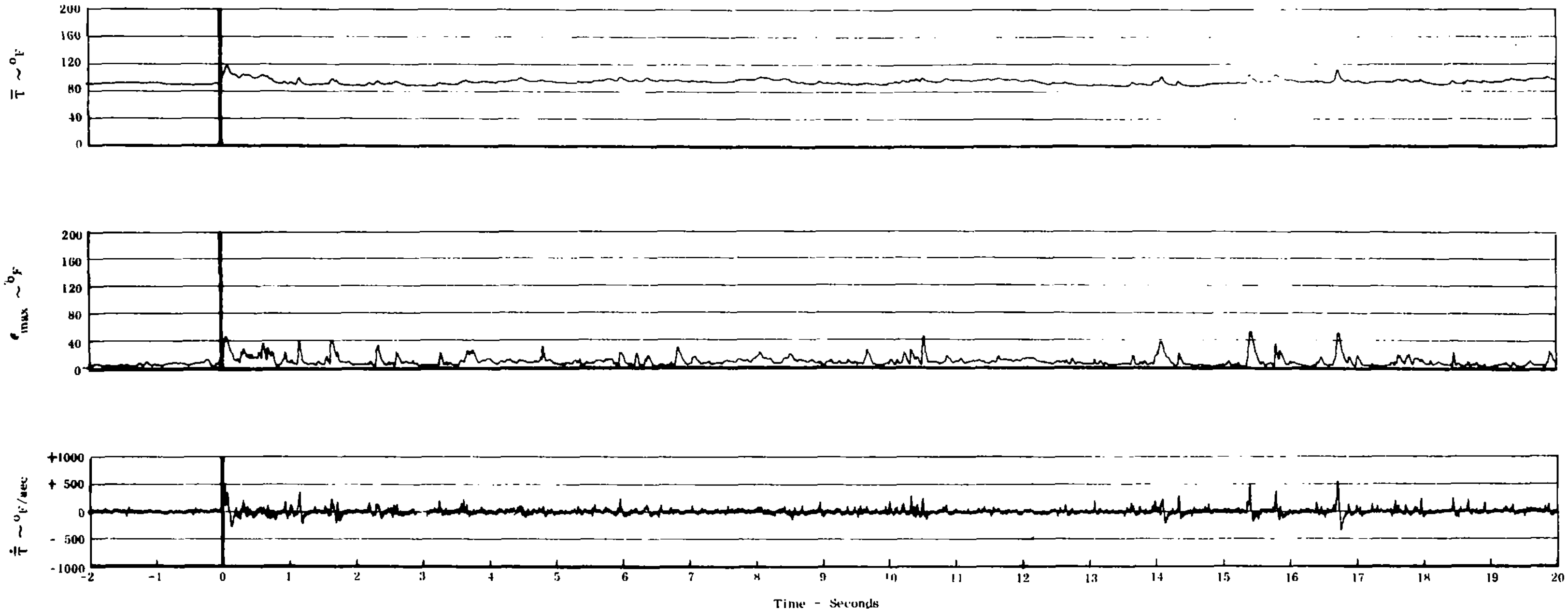

(a) FORWARD INLET

FIGURE A3-2. SMALL-SCALE INGESTION CHARACTERISTICS HISTORY

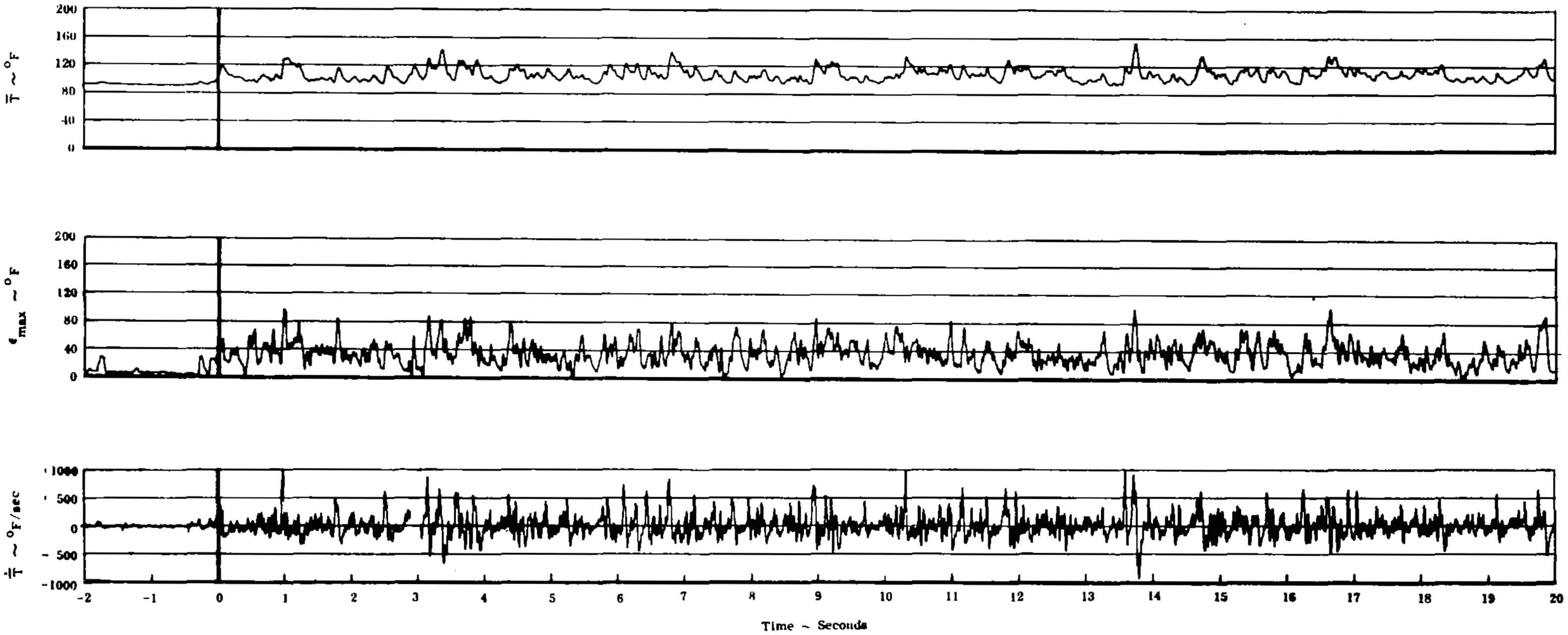

Test 3

(b) AFT INLET

FIGURE A3-2 (cont'd). SMALL-SCALE INGESTION CHARACTERISTICS HISTORY

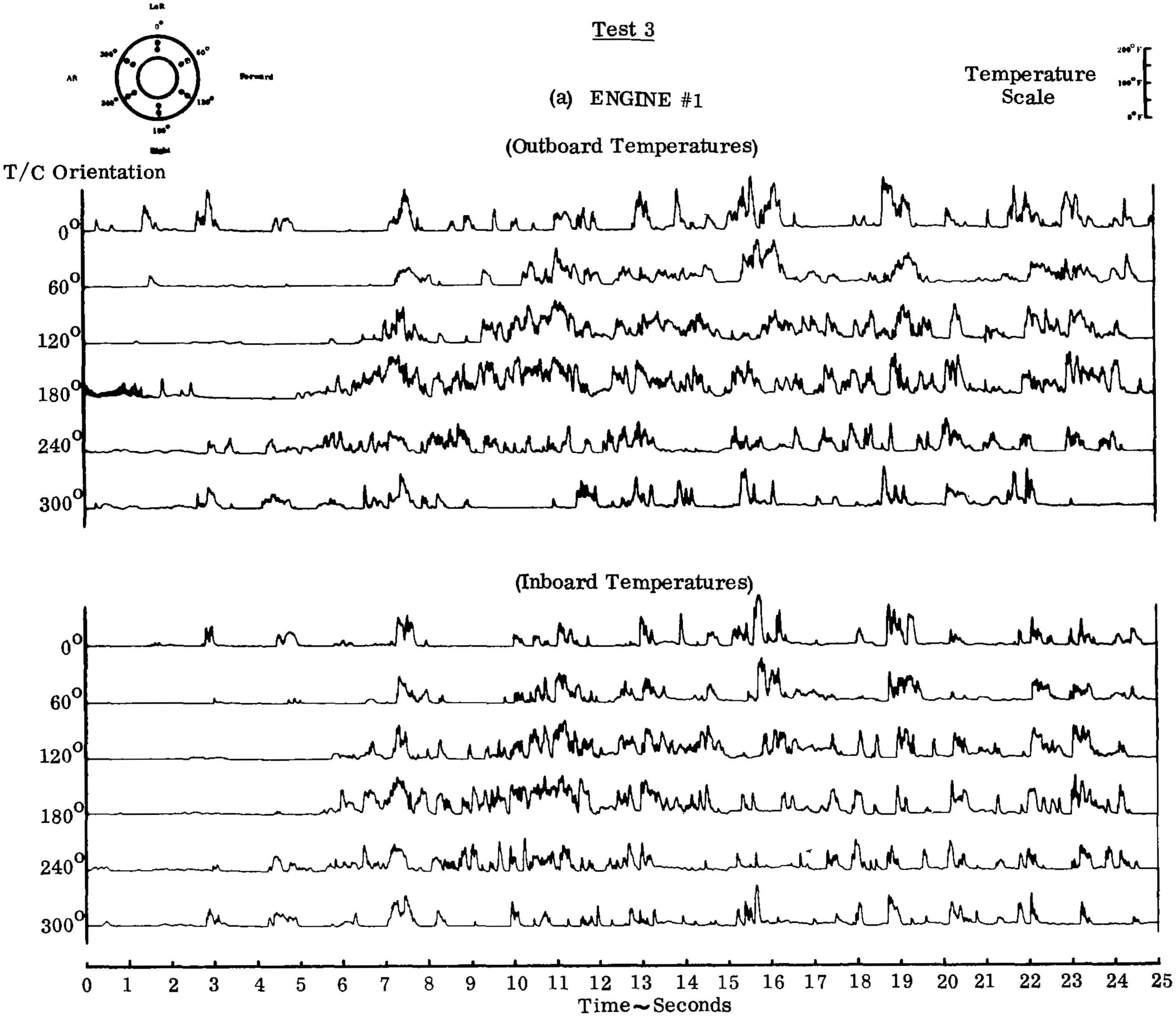

FIGURE A3-3. FULL-SCALE INLET TEMPERATURE HISTORY

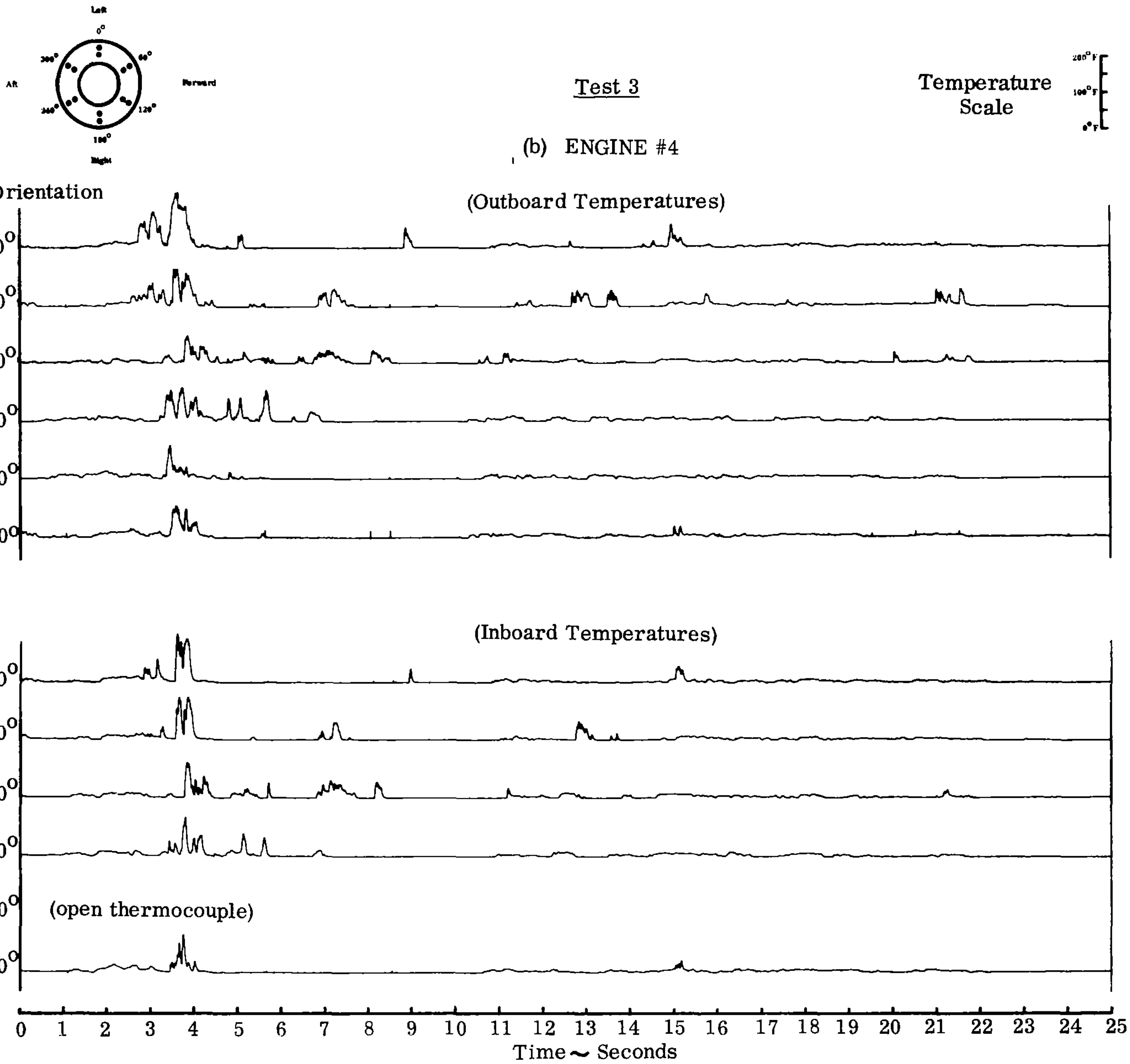

FIGURE A3-3 (cont'd). FULL-SCALE INLET TEMPERATURE HISTORY

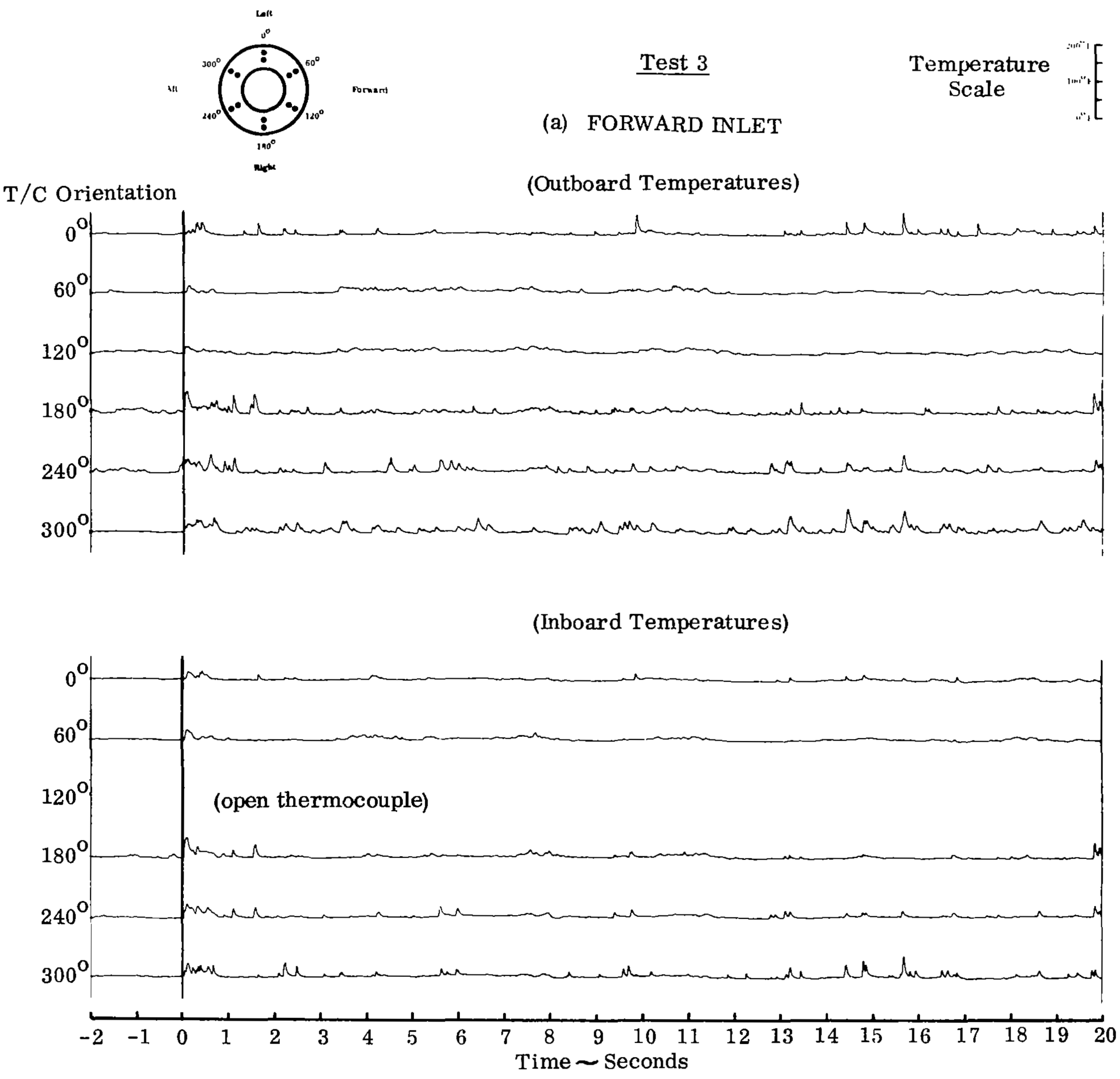

FIGURE A3-4. SMALL-SCALE INLET TEMPERATURE HISTORY

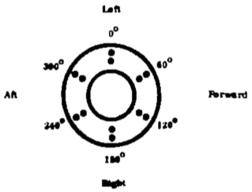

Test 3

(b) AFT INLET

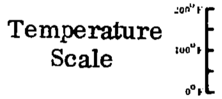

(Outboard Temperatures)

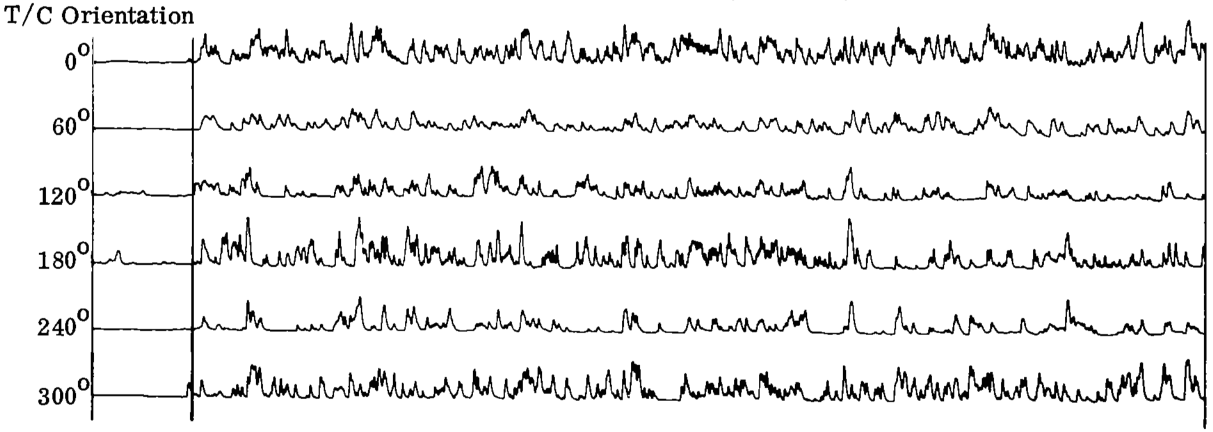

(Inboard Temperatures)

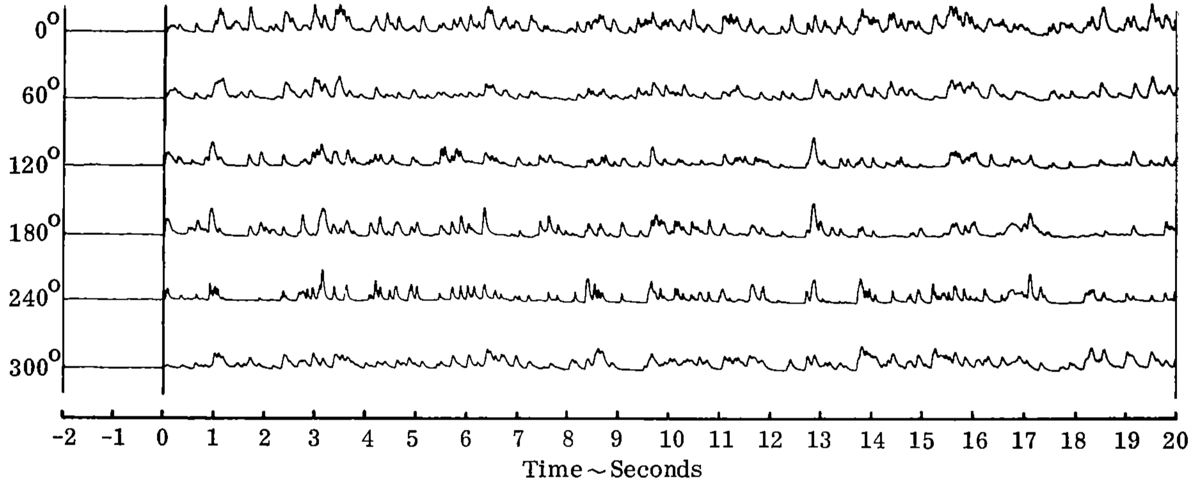

FIGURE A3-4 (cont'd). SMALL-SCALE INLET TEMPERATURE HISTORY

Test 4

Two Engine Operation

H/D = 6

Wind < 4 MPH

TIME-AVERAGE INGESTION CHARACTERISTICS

	Full-Scale		Small-Scale	
	Engine #1	Engine #4	Fwd Inlet	Aft Inlet
$\Delta\hat{\bar{T}}$	16°F	4°F	3°F	16°F
$\hat{\epsilon}_{max}$	46°F	16°F	10°F	38°F
$\lvert\hat{\dot{\bar{T}}}\rvert$	135°F/sec	55°F/sec	40°F/sec	115°F/sec

Test 4

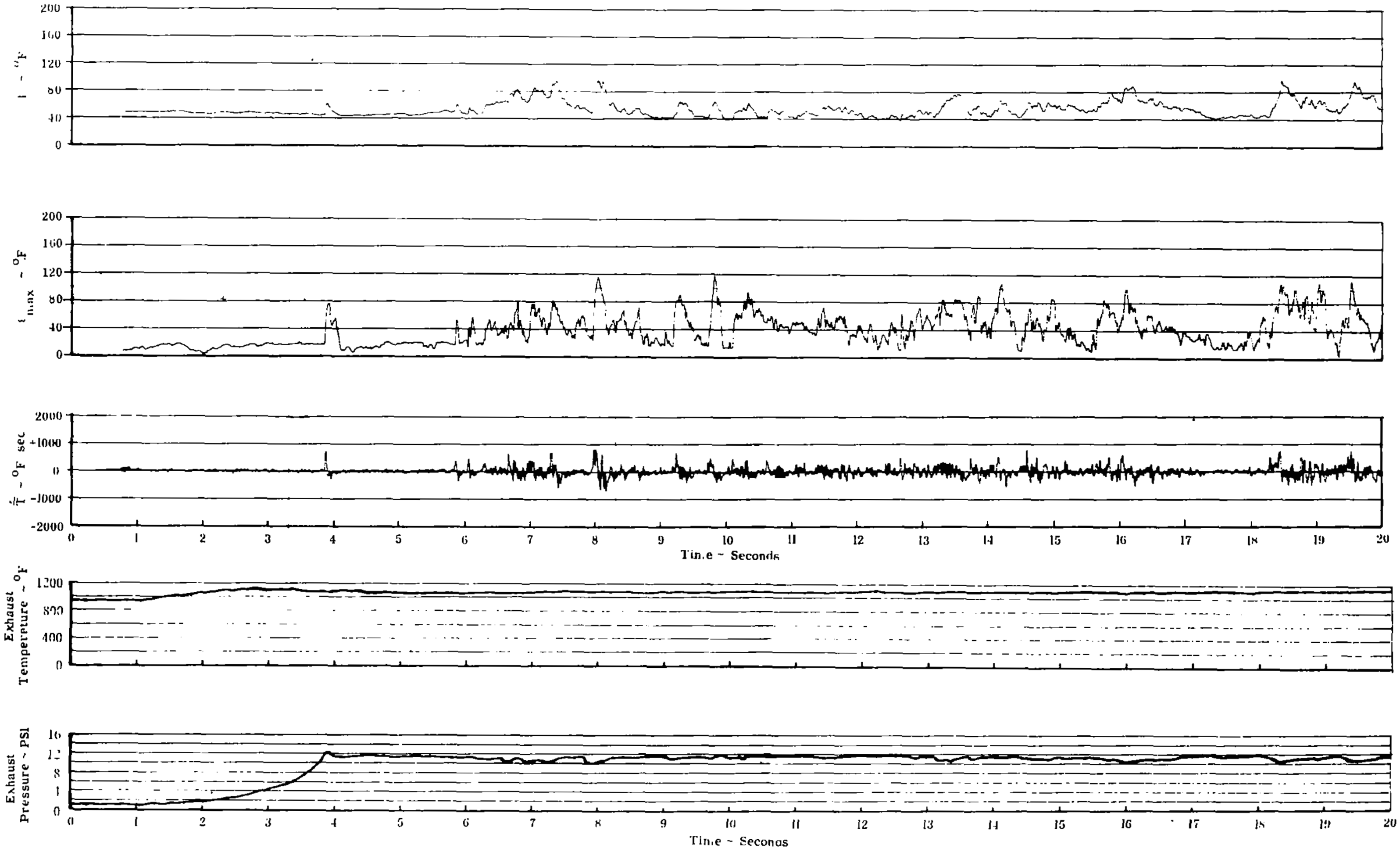

(a) ENGINE #1

FIGURE A4-1. FULL-SCALE INGESTION CHARACTERISTICS HISTORY

Test 4

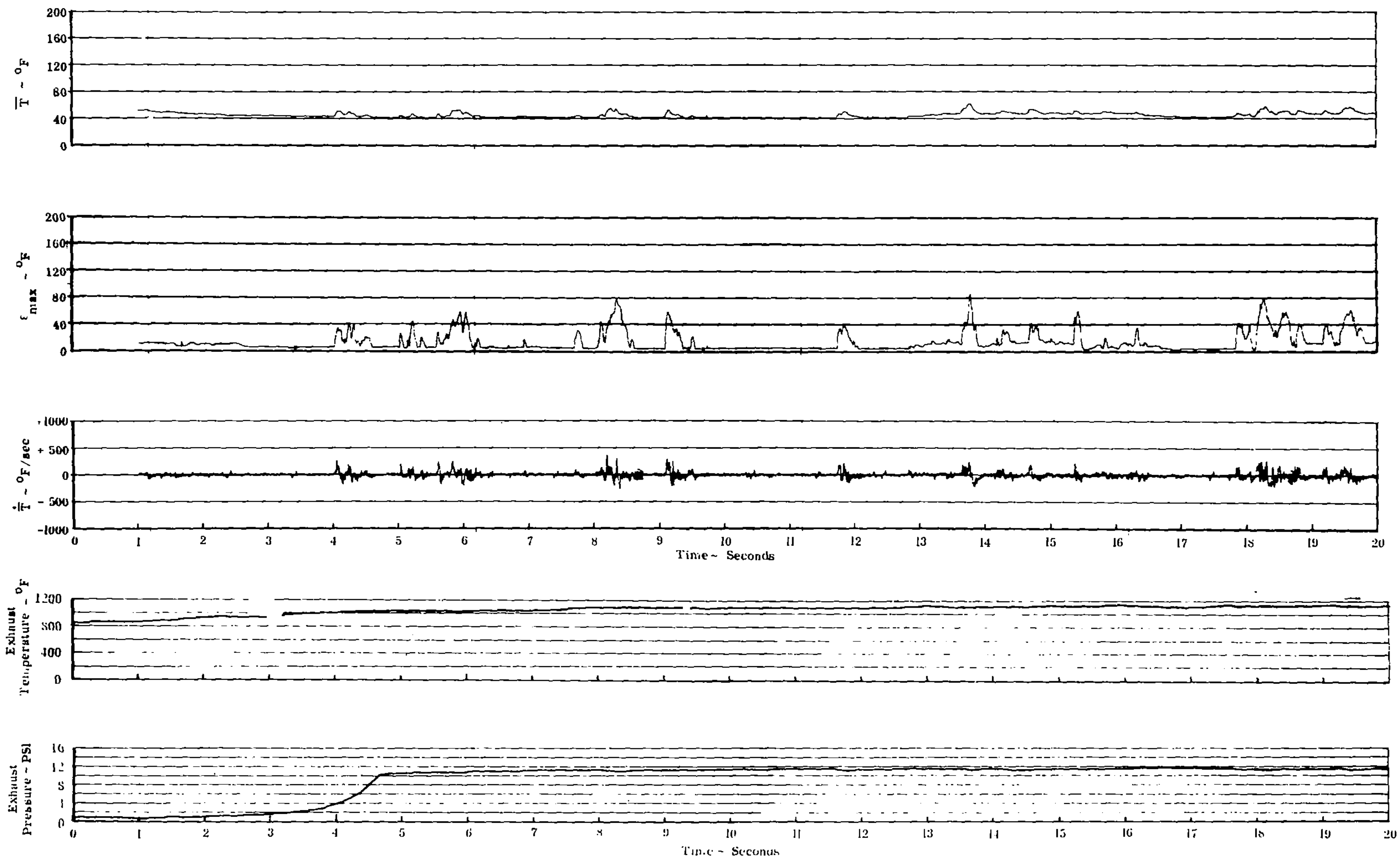

(b) ENGINE #4

FIGURE A4-1 (cont'd). FULL-SCALE INGESTION CHARACTERISTICS HISTORY

Test 4

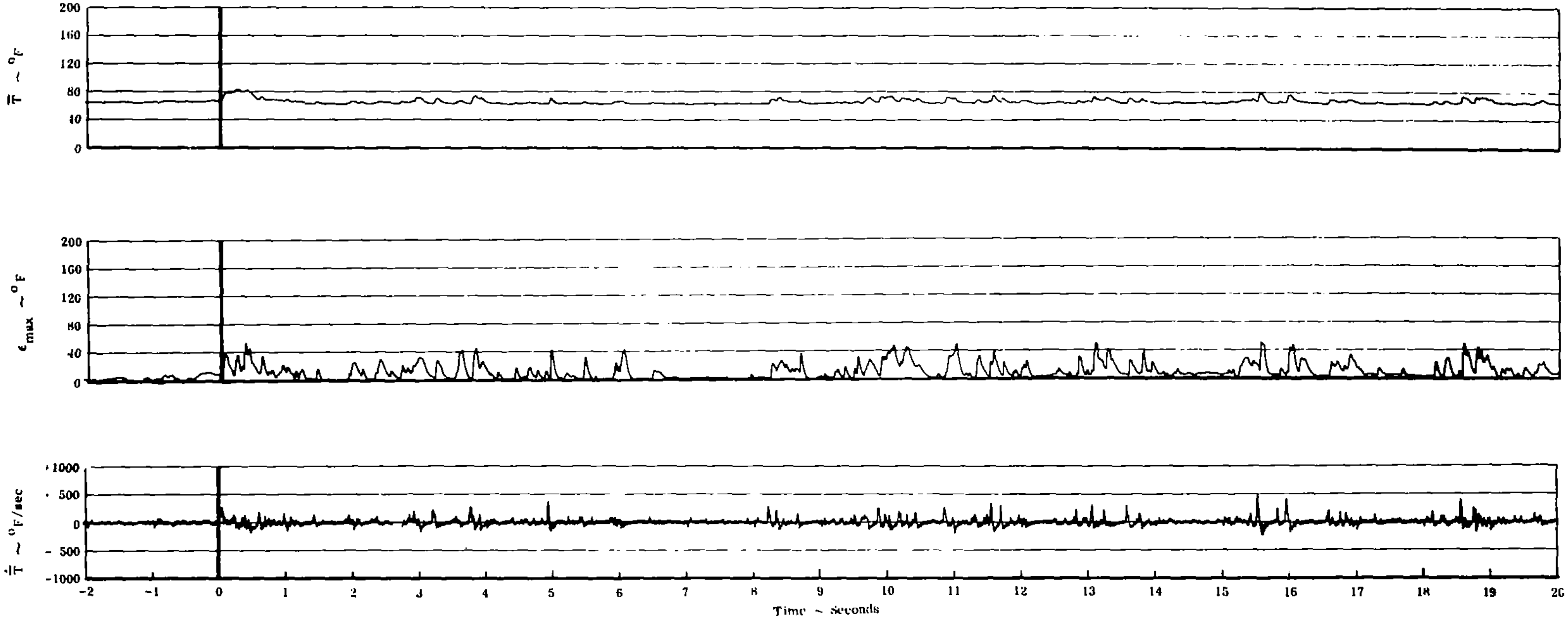

(a) FORWARD INLET

FIGURE A4-2. SMALL-SCALE INGESTION CHARACTERISTICS HISTORY

Test 4

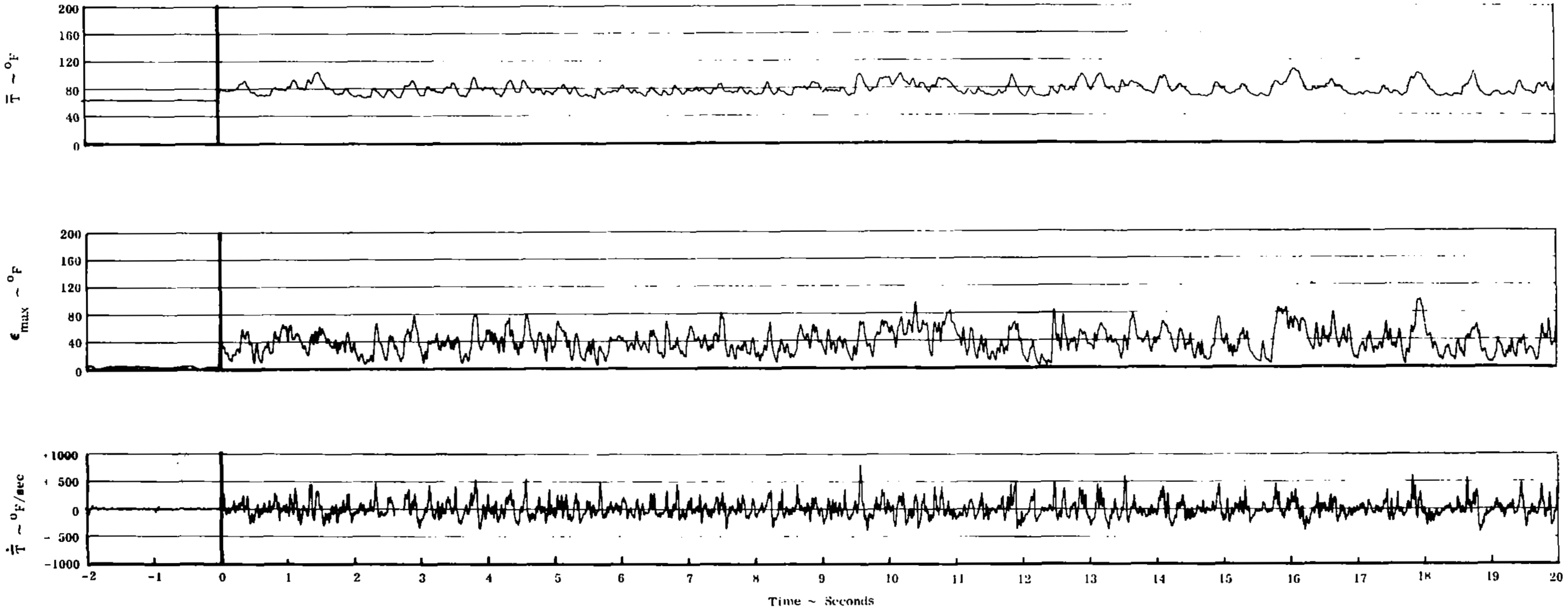

(b) AFT INLET

FIGURE A4-2 (cont'd). SMALL-SCALE INGESTION CHARACTERISTICS HISTORY

Test 5

Two Engine Operation

H/D = 8

Wind < 4 MPH

TIME-AVERAGE INGESTION CHARACTERISTICS

	Full-Scale		Small-Scale	
	Engine #1	Engine #4	Fwd Inlet	Aft Inlet
$\Delta\hat{T}$	$3^{o}F$	$3^{o}F$	$3^{o}F$	$6^{o}F$
$\hat{\epsilon}_{max}$	$7^{o}F$	$4^{o}F$	$6^{o}F$	$16^{o}F$
$\lvert\hat{\dot{T}}\rvert$	$35^{o}F/sec$	———	$25^{o}F/sec$	$50^{o}F/sec$

Test 5

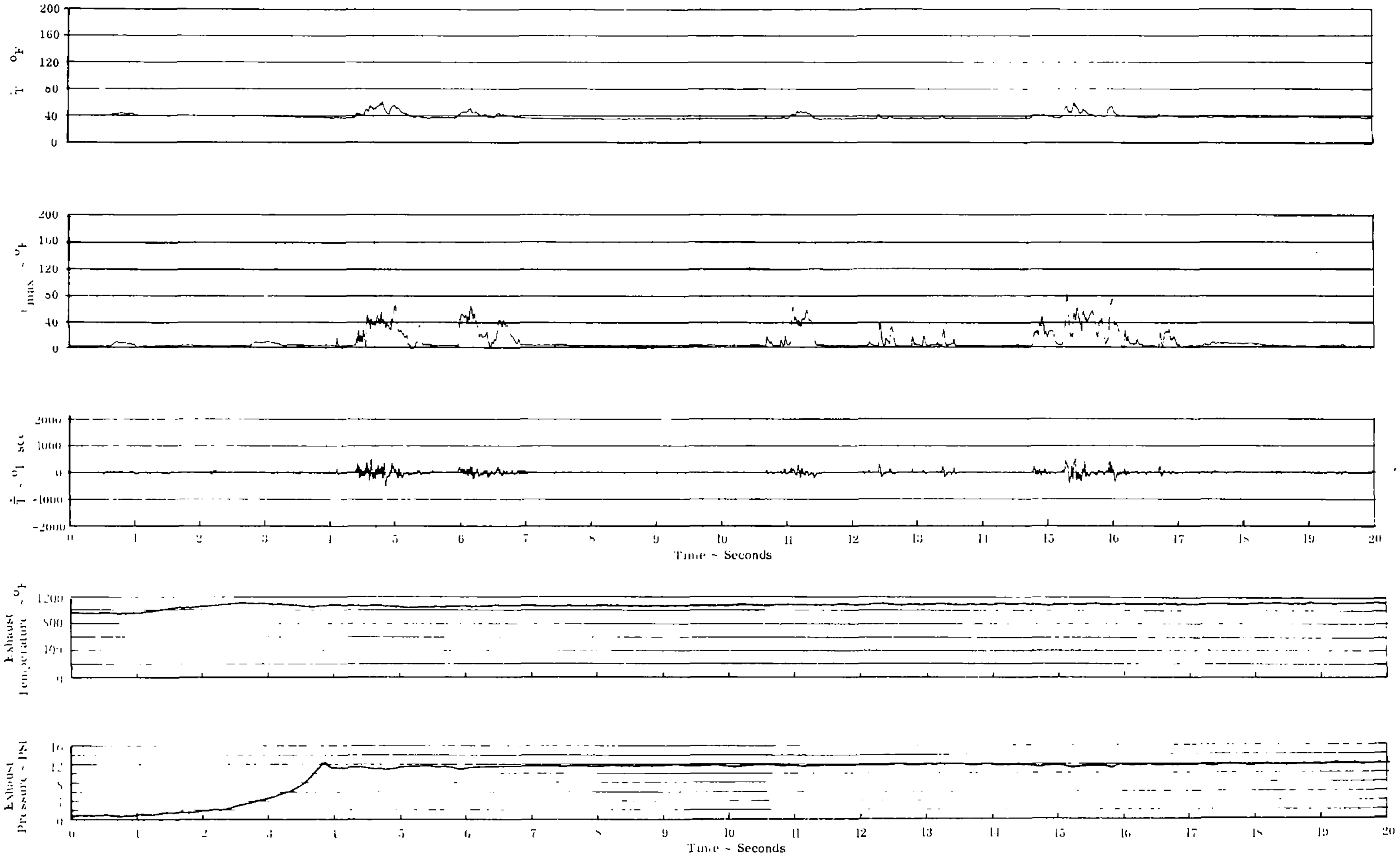

(a) ENGINE #1

FIGURE A5-1. FULL-SCALE INGESTION CHARACTERISTICS HISTORY

Test 5

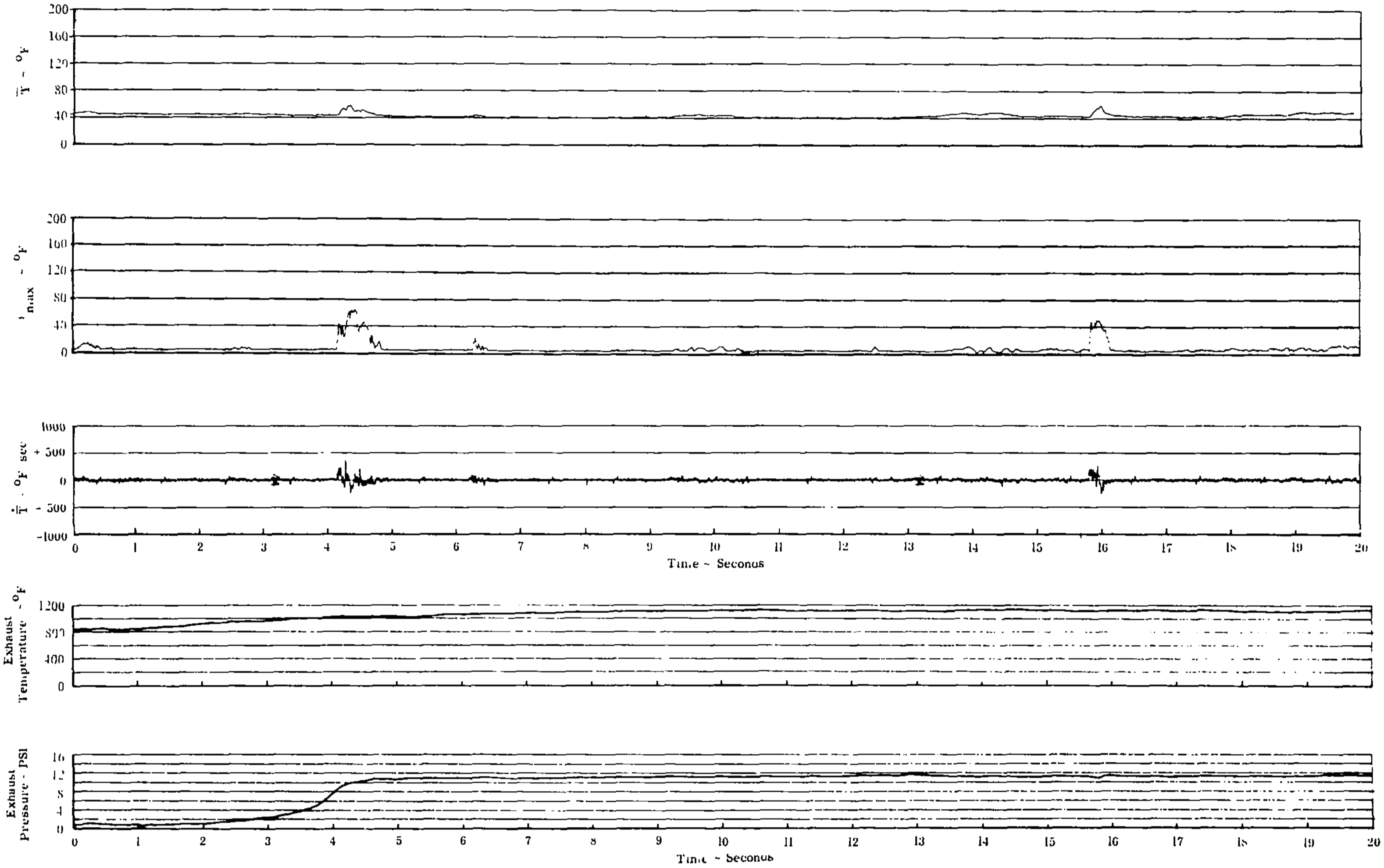

(b) ENGINE #4

FIGURE A5-1 (cont'd). FULL-SCALE INGESTION CHARACTERISTICS HISTORY

Test 5

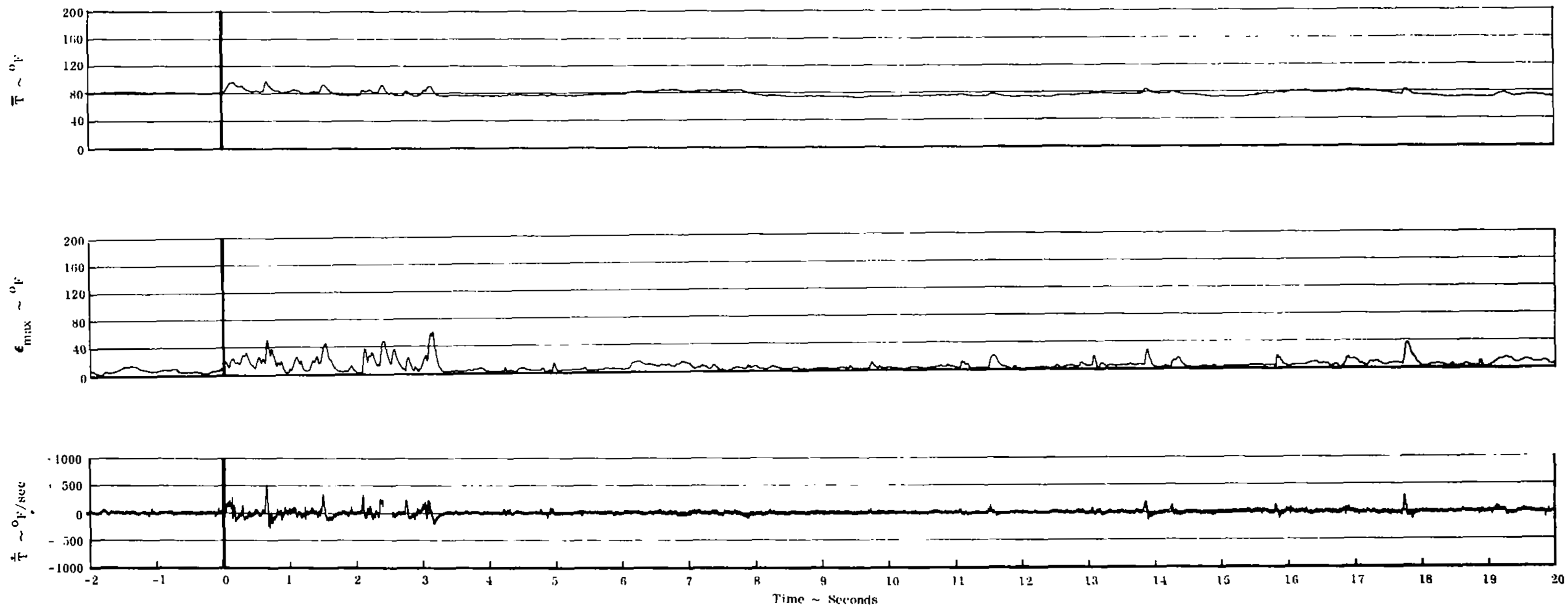

(a) FORWARD INLET

FIGURE A5-2. SMALL-SCALE INGESTION CHARACTERISTICS HISTORY

Test 5

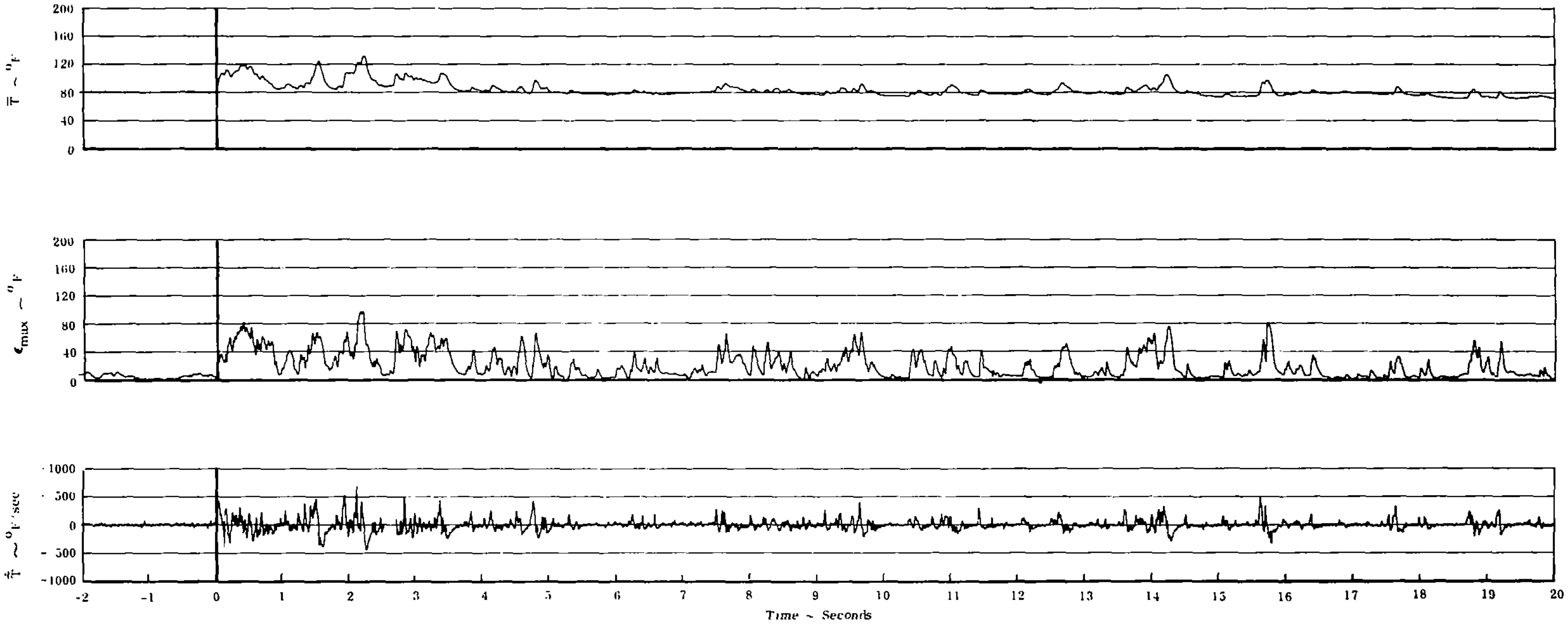

(b) AFT INLET

FIGURE A5-2 (cont'd). SMALL-SCALE INGESTION CHARACTERISTICS HISTORY

Test 6

Two Engine Operation

$H/D = 4$

Wind = 16 MPH

TIME-AVERAGE INGESTION CHARACTERISTICS

	Full-Scale		Small-Scale	
	Engine #1	Engine #4	Fwd Inlet	Aft Inlet
$\Delta\hat{T}$	$4^{o}F$	$3^{o}F$	$3^{o}F$	$2^{o}F$
$\hat{\epsilon}_{max}$	$11^{o}F$	$6^{o}F$	$5^{o}F$	$3^{o}F$
$\lvert\hat{\dot{T}}\rvert$	$60^{o}F/sec$	$50^{o}F/sec$	$40^{o}F/sec$	$30^{o}F/sec$

Test 6

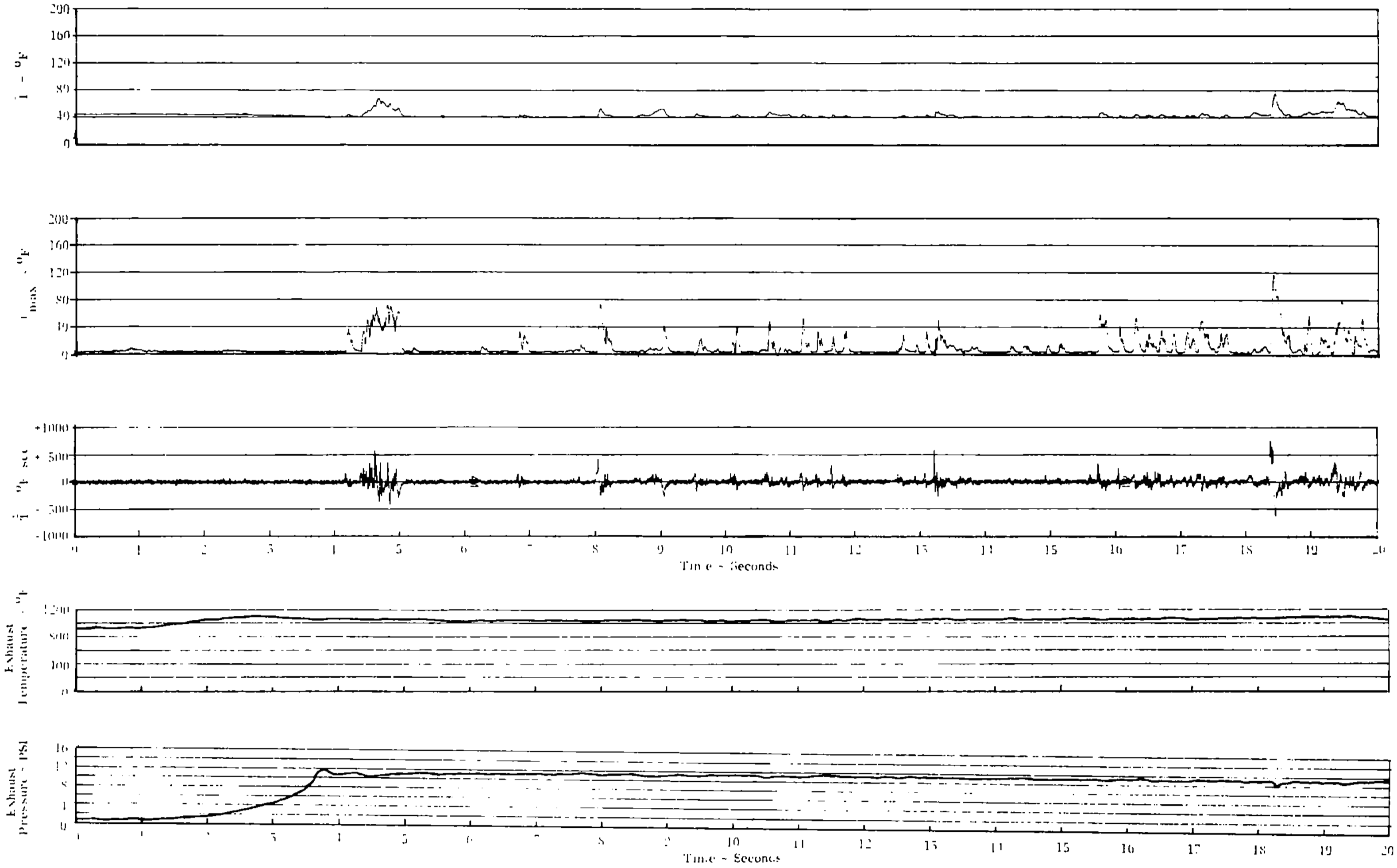

(a) ENGINE #1

FIGURE A6-1. FULL-SCALE INGESTION CHARACTERISTICS HISTORY

Test 6

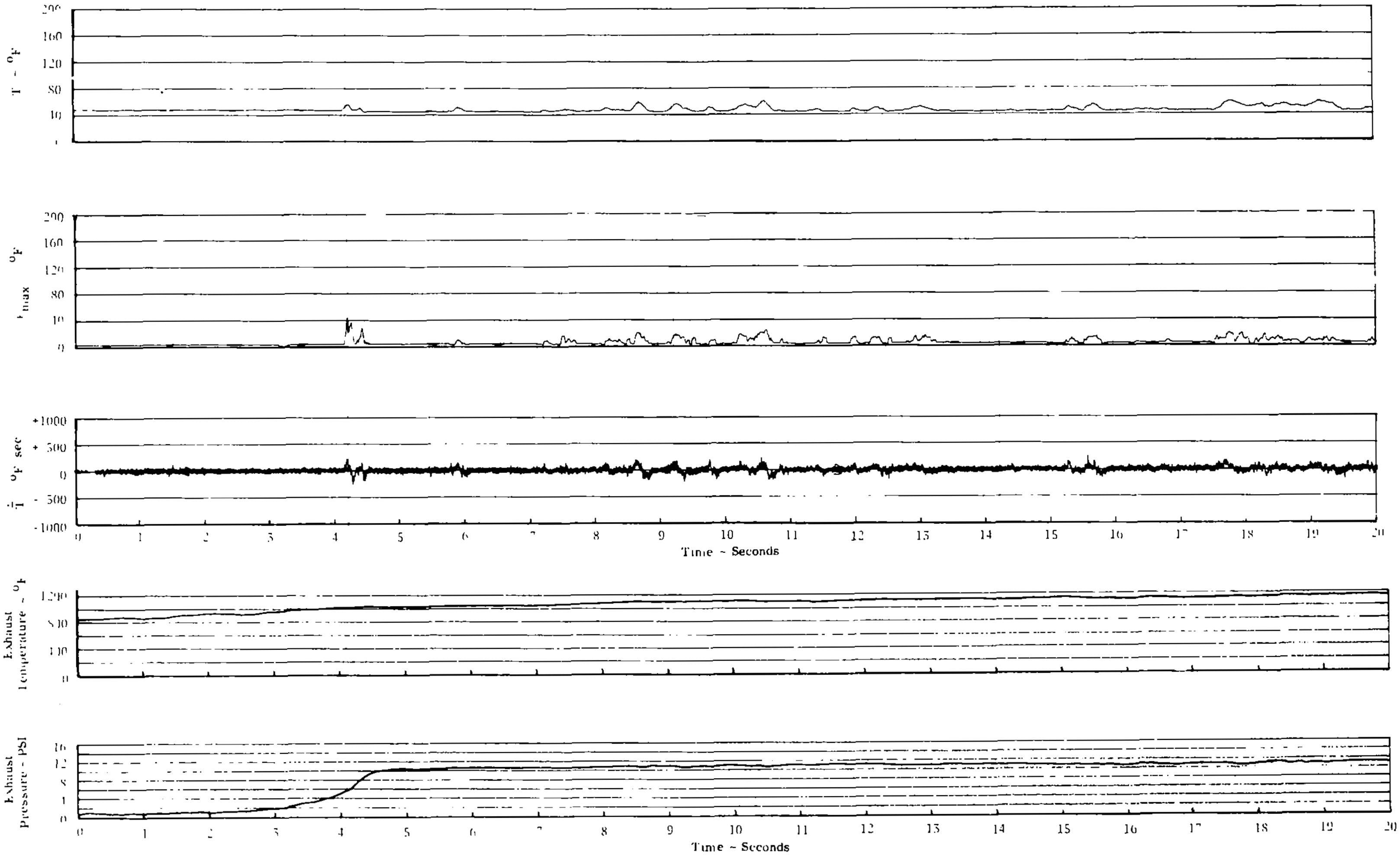

(b) ENGINE #4

FIGURE A6-1 (cont'd). FULL-SCALE INGESTION CHARACTERISTICS HISTORY

Test 6

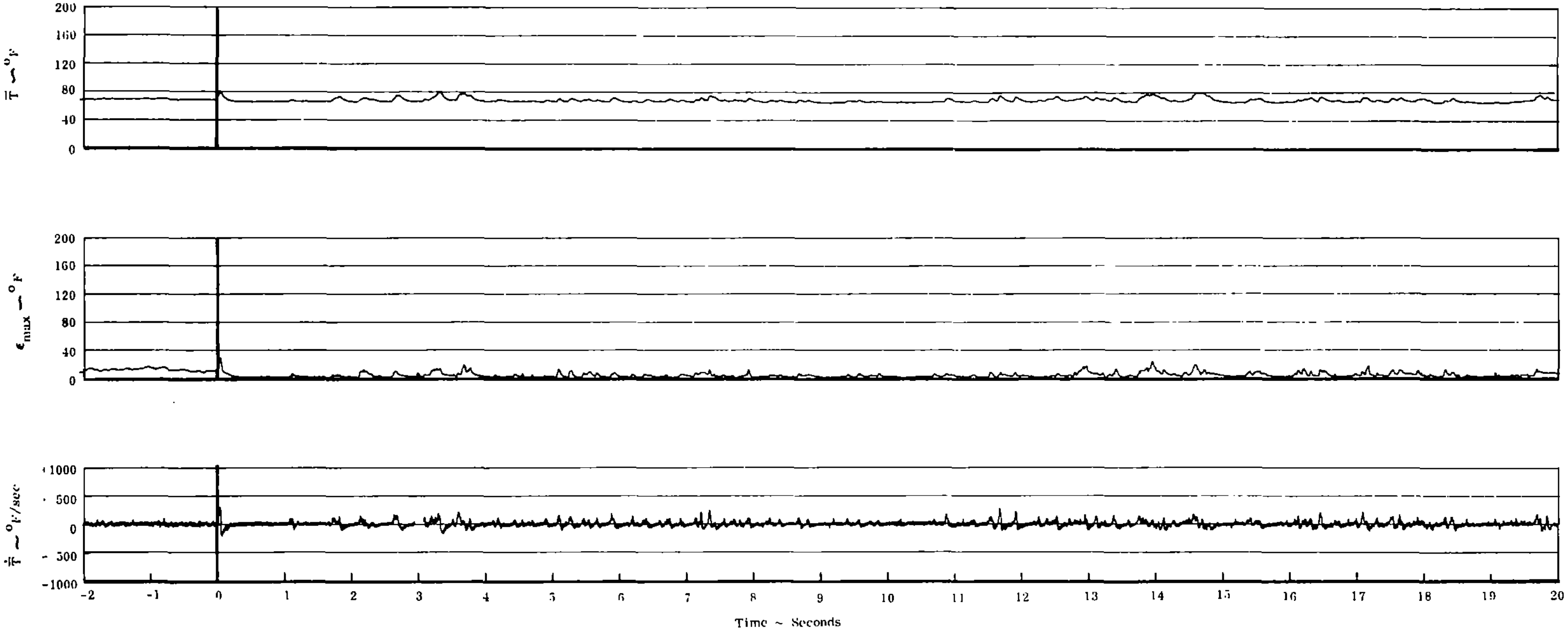

(a) FORWARD INLET

FIGURE A6-2. SMALL-SCALE INGESTION CHARACTERISTICS HISTORY

Test 6

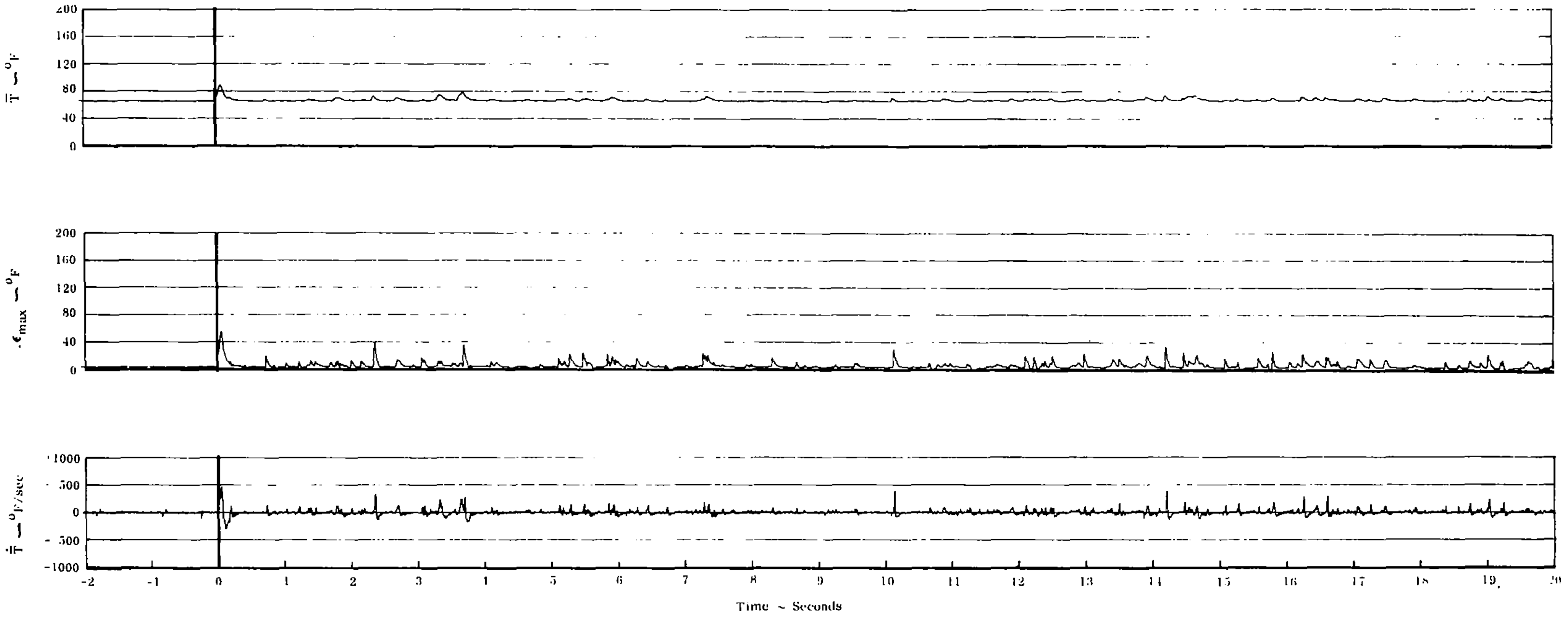

(b) AFT INLET

FIGURE A6-2 (cont'd). SMALL-SCALE INGESTION CHARACTERISTICS HISTORY

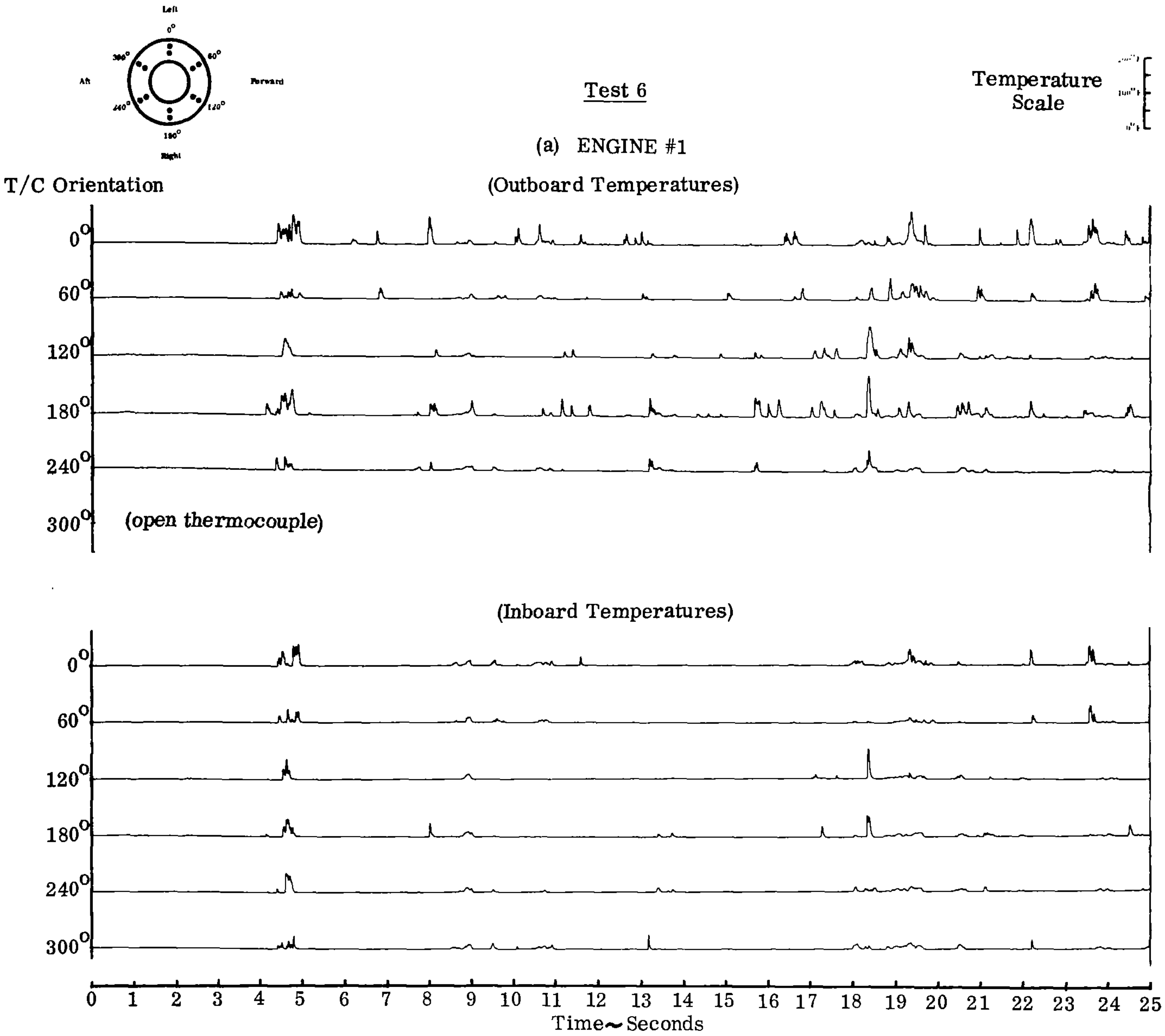

FIGURE A6-3. FULL-SCALE INLET TEMPERATURE HISTORY

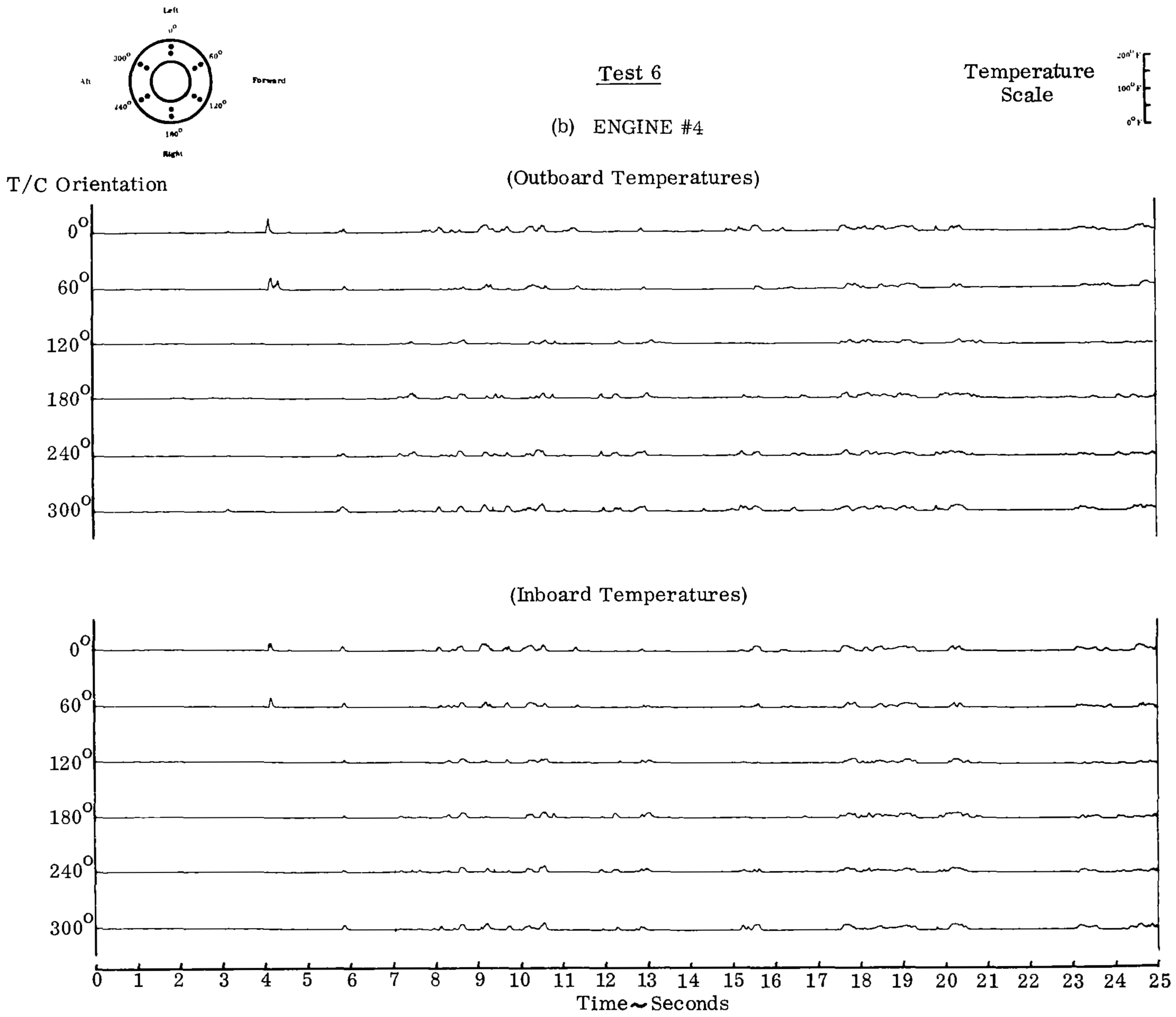

Test 6

(b) ENGINE #4

FIGURE A6-3 (cont'd). FULL-SCALE INLET TEMPERATURE HISTORY

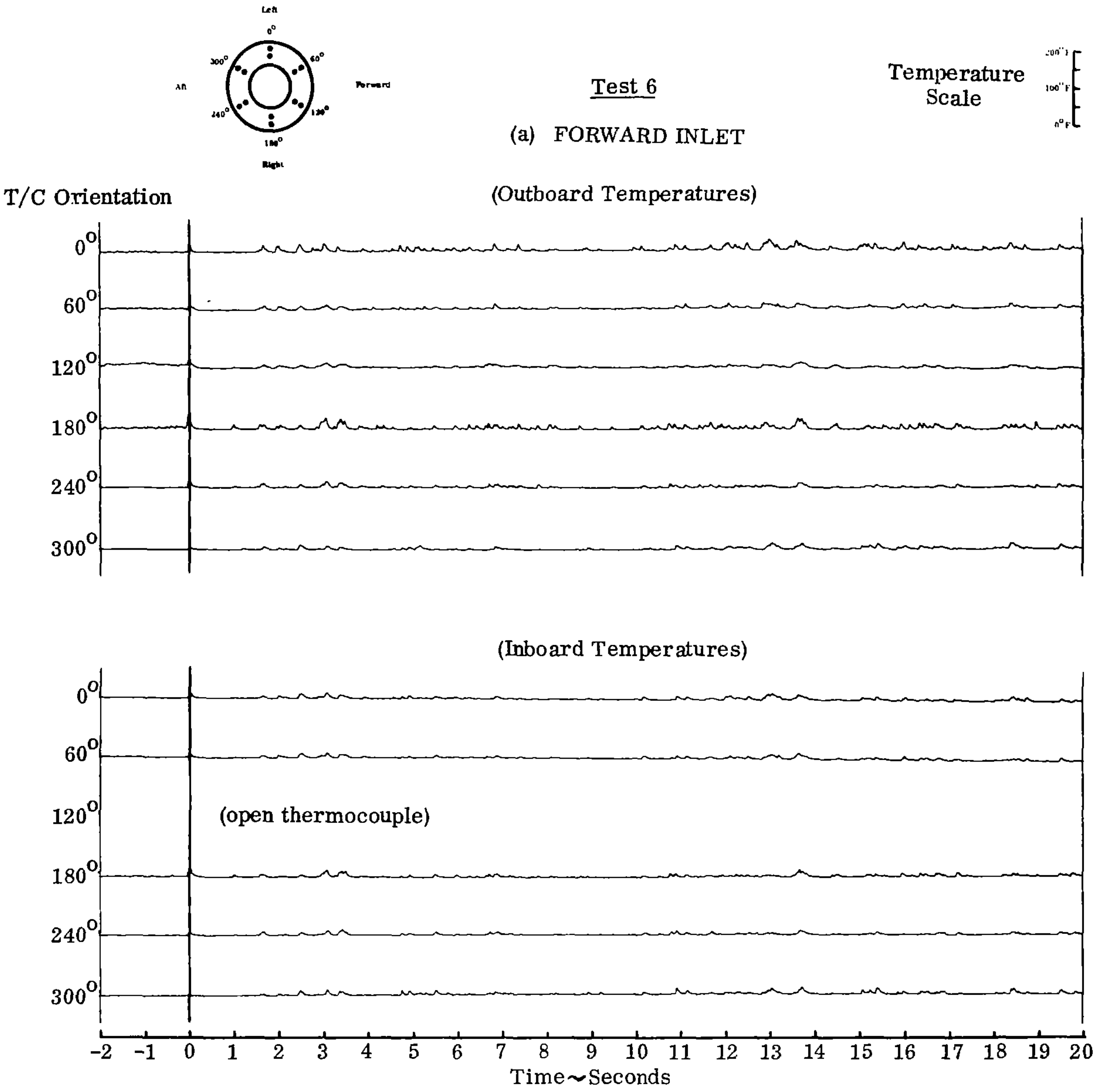

Test 6

(a) FORWARD INLET

(Outboard Temperatures)

(Inboard Temperatures)

(open thermocouple)

FIGURE A6-4. SMALL-SCALE INLET TEMPERATURE HISTORY

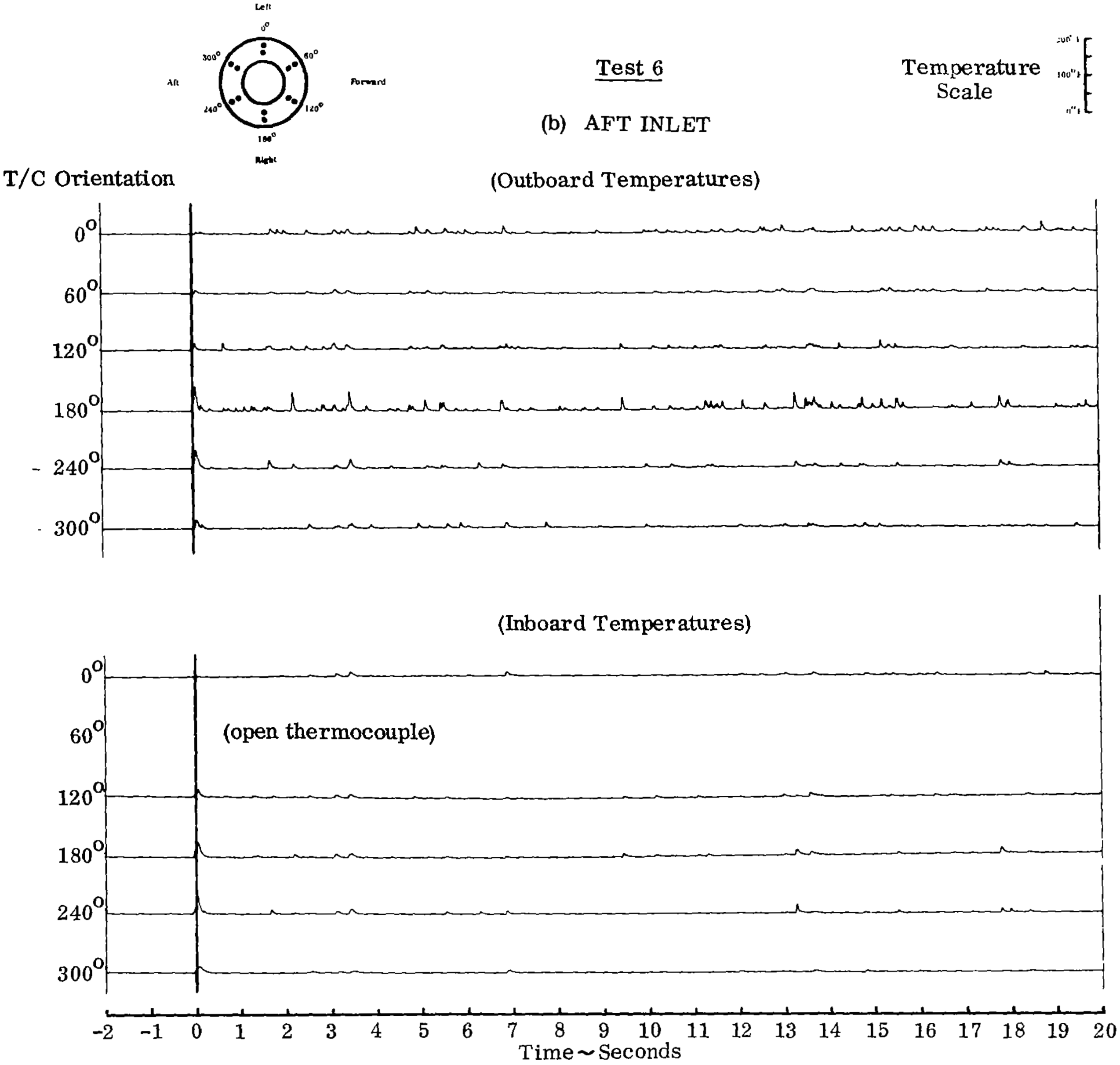

Test 6

(b) AFT INLET

FIGURE A6-4 (cont'd). SMALL-SCALE INLET TEMPERATURE HISTORY

Test 7

Single Engine Operation

$H/D = 4$

Wind < 4 MPH

TIME-AVERAGE INGESTION CHARACTERISTICS

	Full-Scale		Small-Scale	
	Engine #1	Engine #4	Fwd Inlet	Aft Inlet
$\Delta\hat{T}$		$0^{\circ}F$	$2^{\circ}F$	
$\hat{\epsilon}_{max}$		$4^{\circ}F$	$4^{\circ}F$	
$\lvert\hat{\dot{T}}\rvert$		—	$20^{\circ}F/sec$	

Test 7

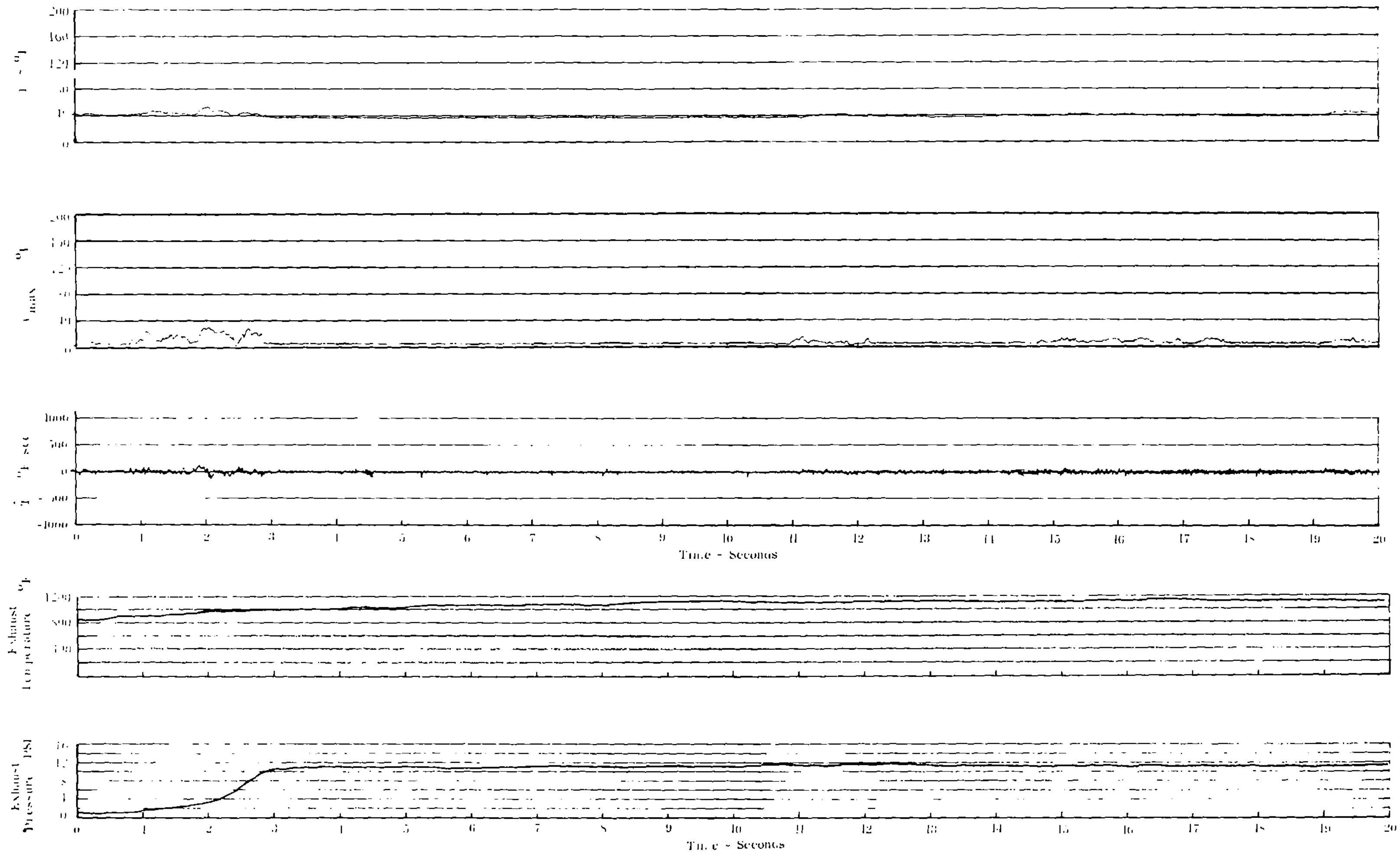

ENGINE #4

FIGURE A7-1. FULL-SCALE INGESTION CHARACTERISTICS HISTORY

Test 7

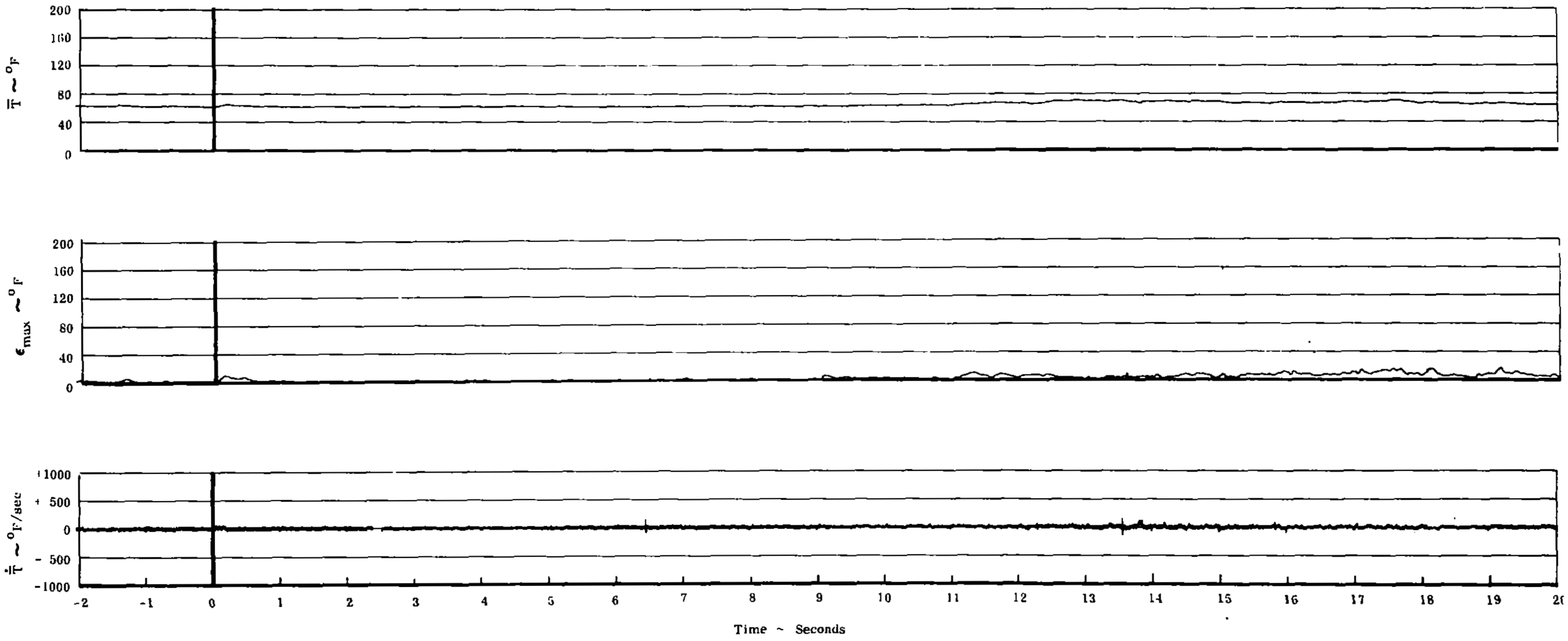

FORWARD INLET

FIGURE A7-2. SMALL-SCALE INGESTION CHARACTERISTICS HISTORY

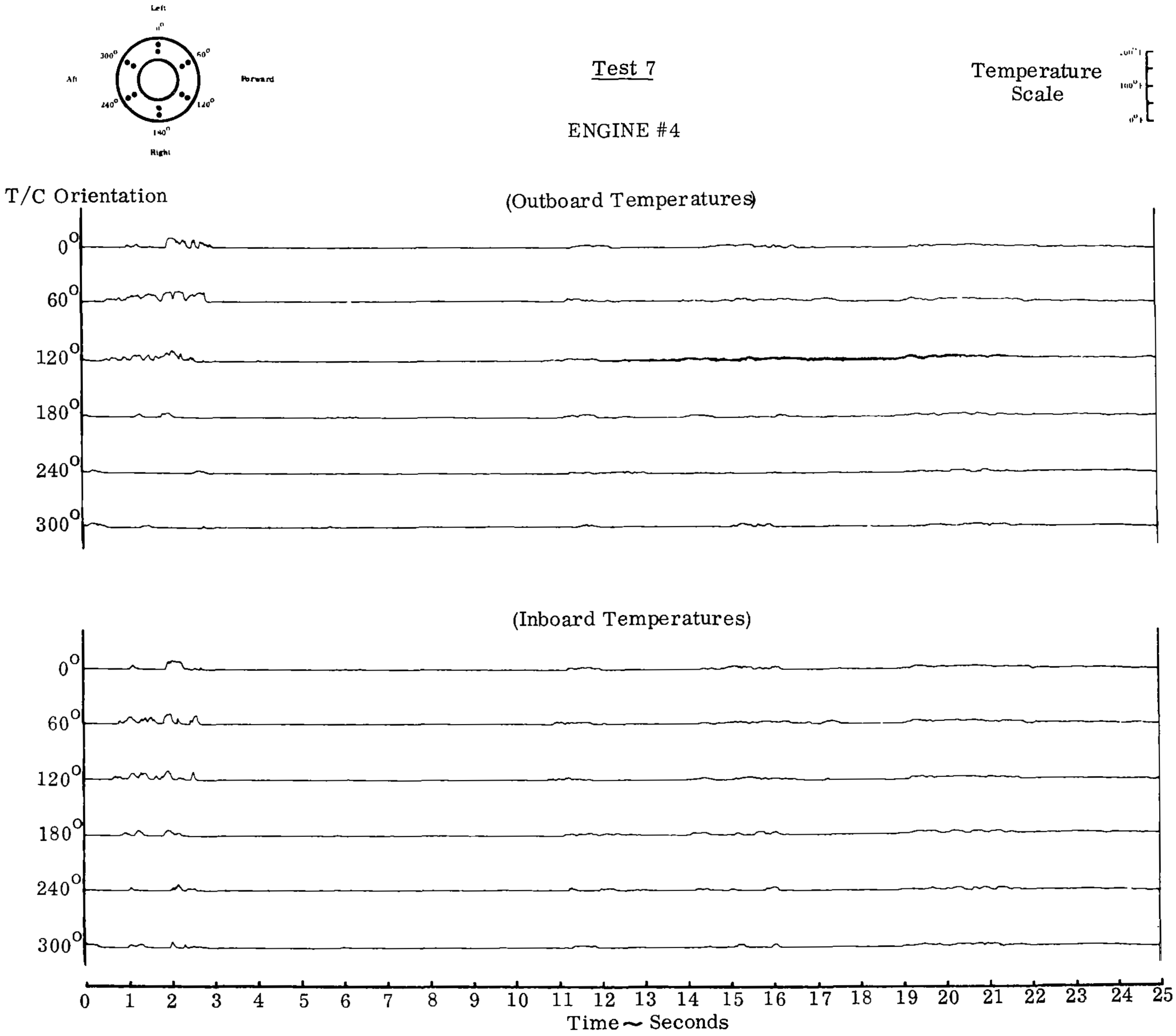

FIGURE A7-3. FULL-SCALE INLET TEMPERATURE HISTORY

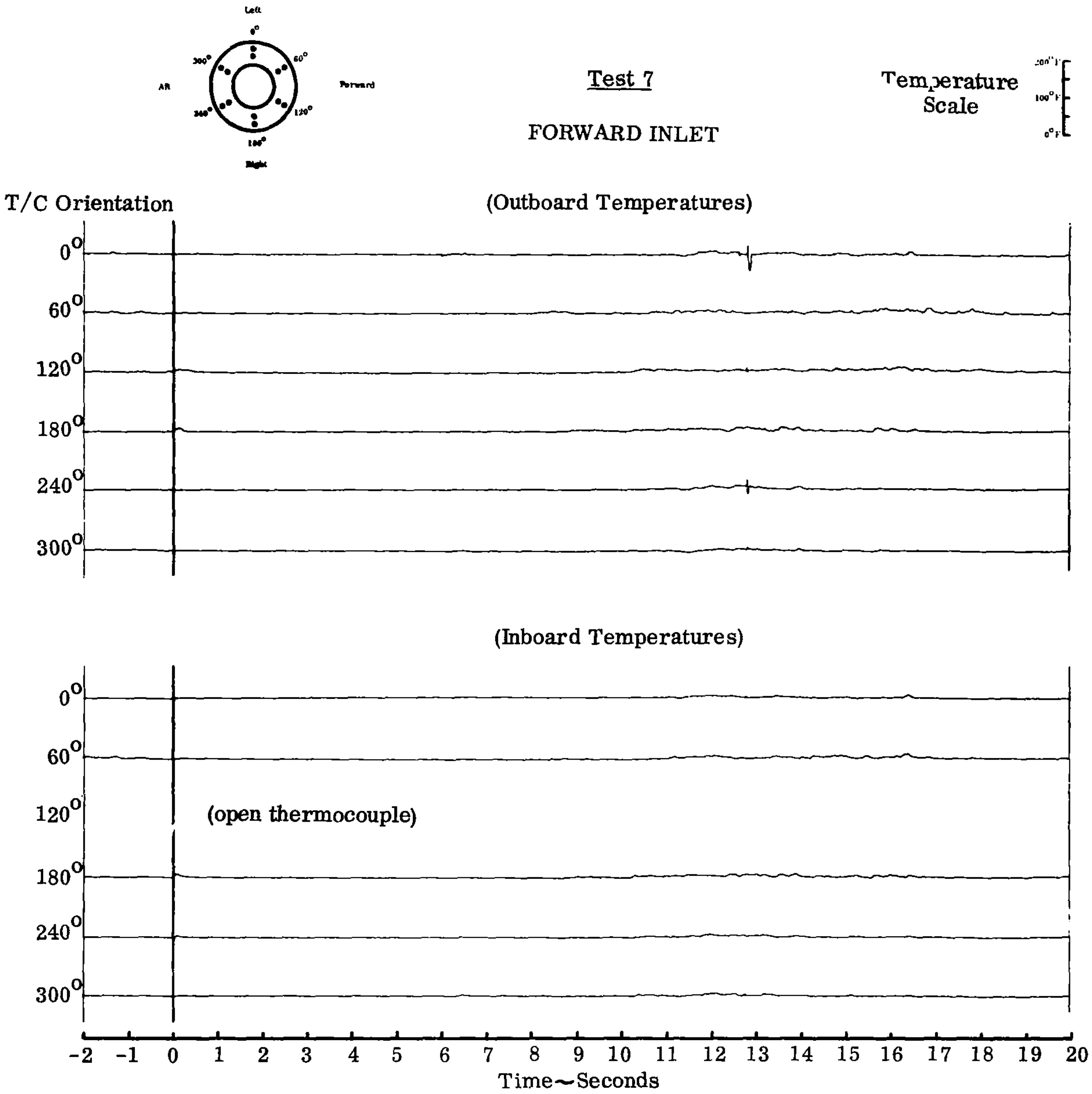

FIGURE A7-4. SMALL-SCALE INLET TEMPERATURE HISTORY

Test 8

Single Engine Operation

H/D = 4

Wind = 16 MPH

TIME-AVERAGE INGESTION CHARACTERISTICS

	Full-Scale		Small-Scale	
	Engine #1	Engine #4	Fwd Inlet	Aft Inlet
$\Delta\hat{\bar{T}}$		$4^{o}F$	$4^{o}F$	
$\hat{\epsilon}_{max}$		$6^{o}F$	$7^{o}F$	
$\lvert\hat{\dot{T}}\rvert$		——	$50^{o}F/sec$	

Test 8

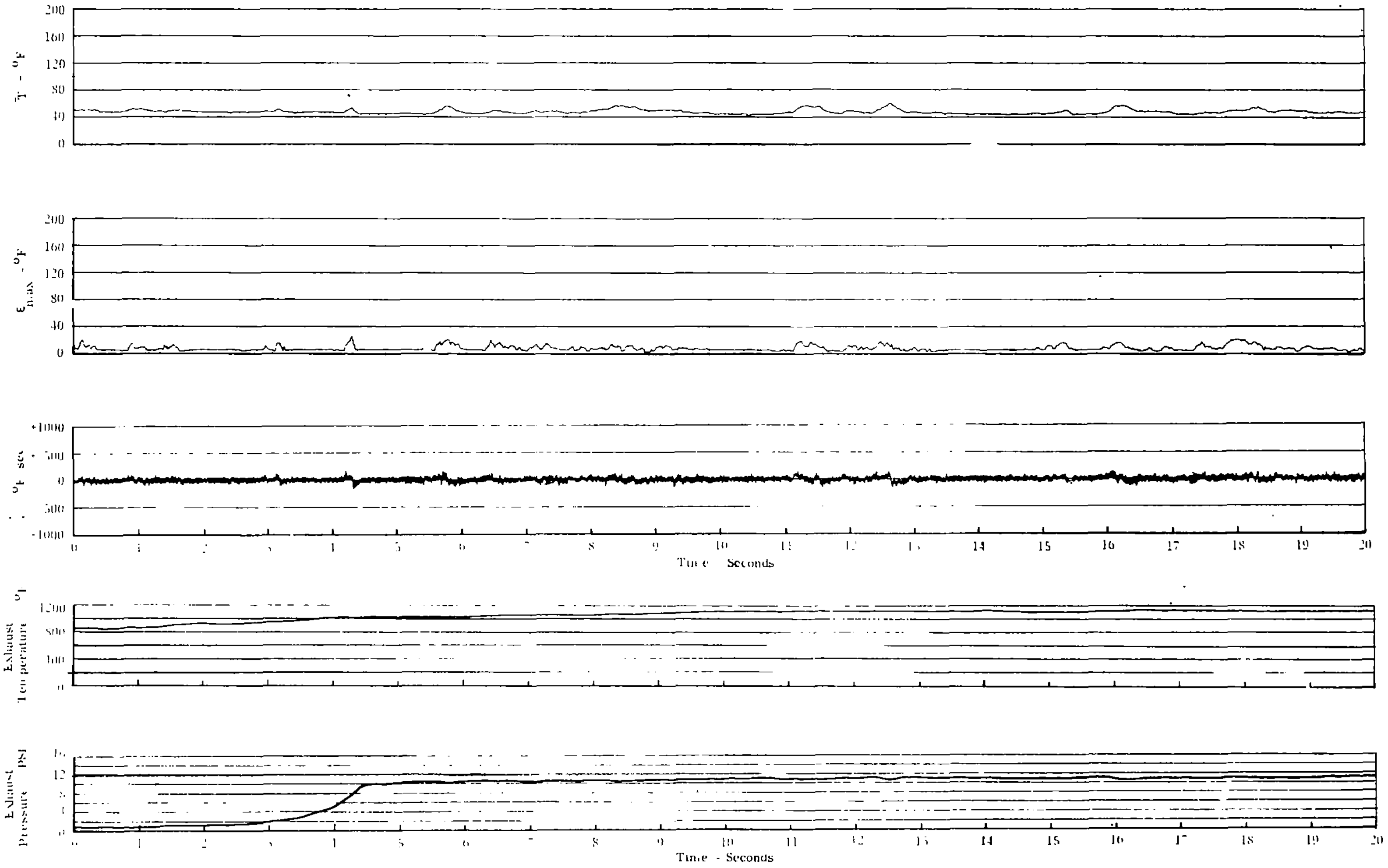

ENGINE #4

FIGURE A8-1. FULL-SCALE INGESTION CHARACTERISTICS HISTORY

Test 8

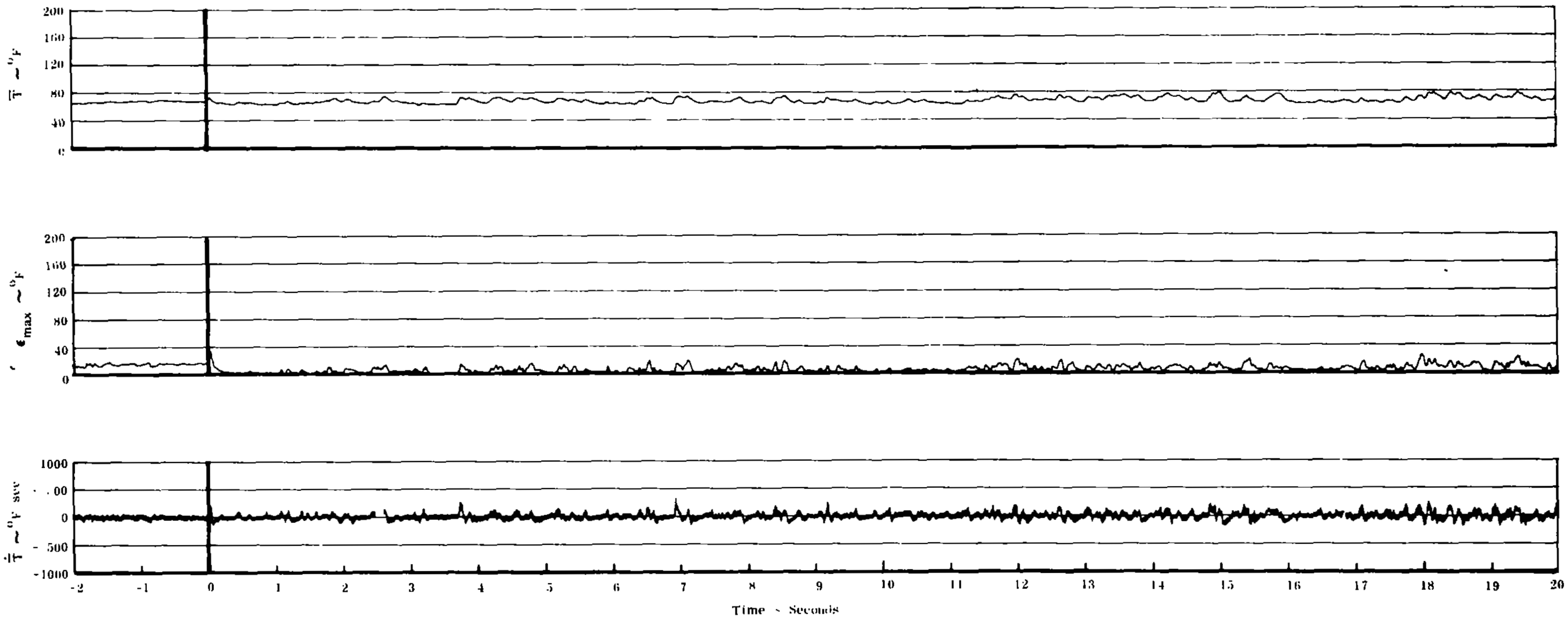

FORWARD INLET

FIGURE A8-2. SMALL-SCALE INGESTION CHARACTERISTICS HISTORY

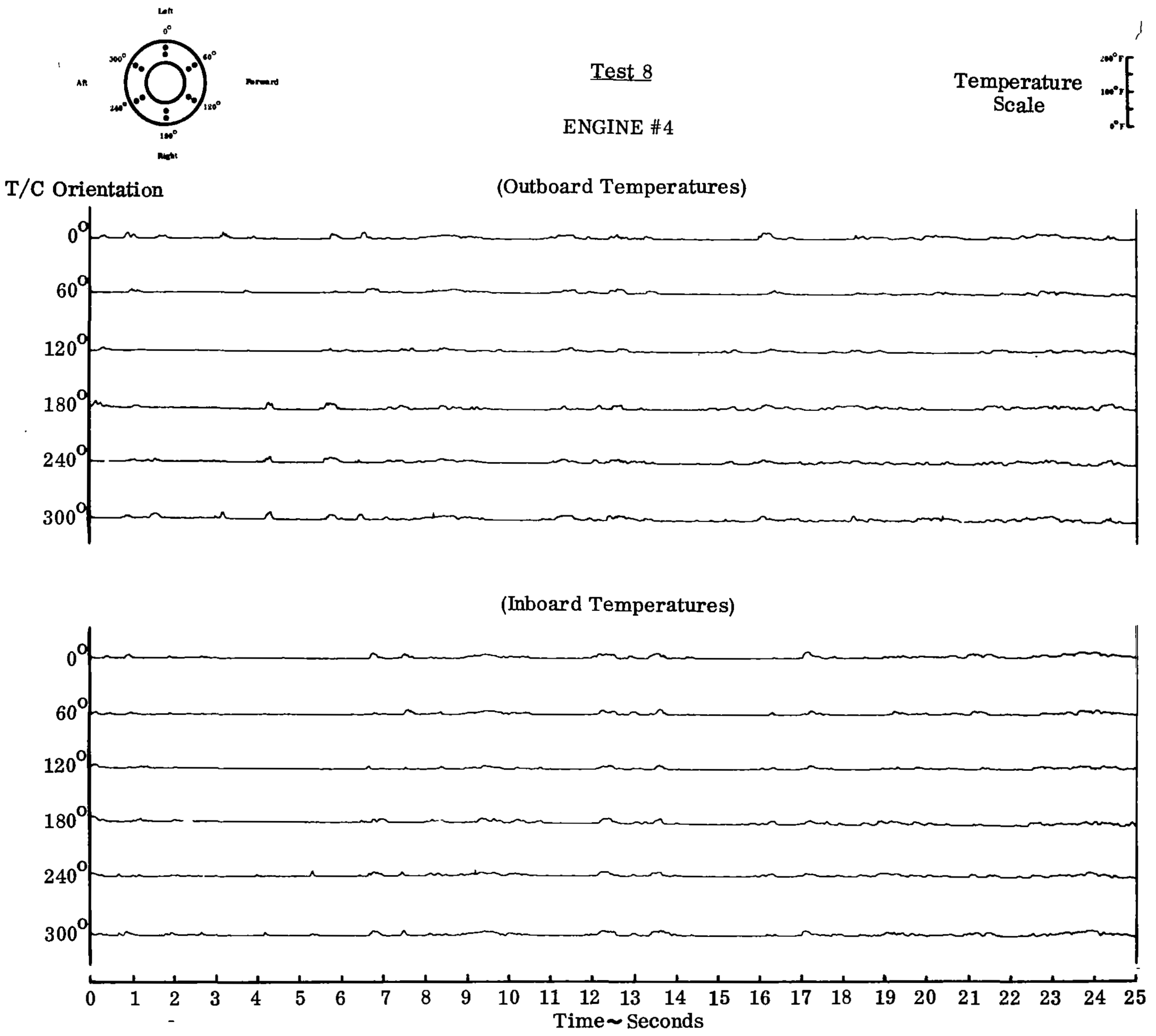

FIGURE A8-3. FULL-SCALE INLET TEMPERATURE HISTORY

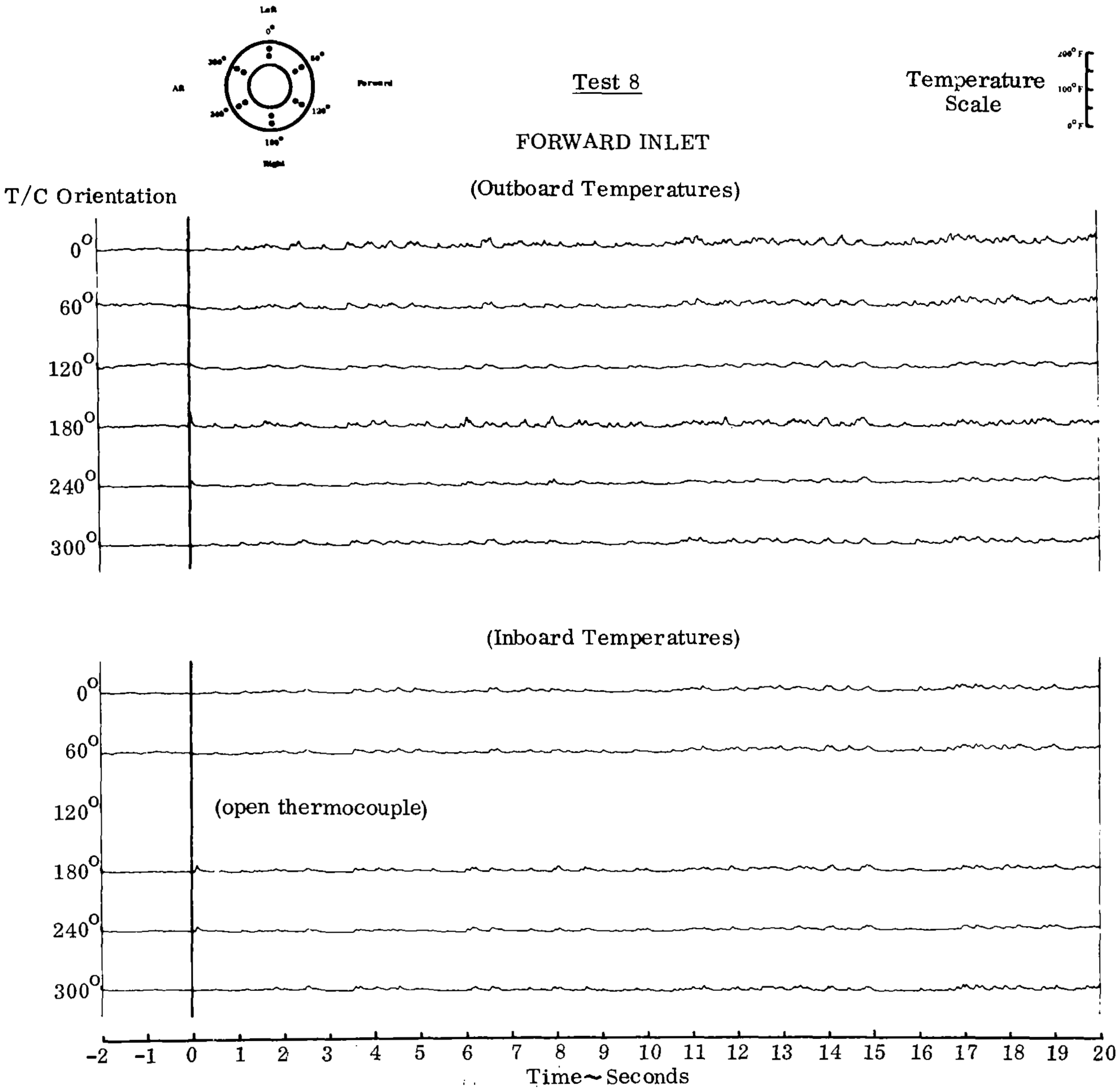

FIGURE A8-4. SMALL-SCALE INLET TEMPERATURE HISTORY